

## ABSTRACT

Title of dissertation: INVESTIGATING ENERGETIC POROUS SILICON  
AS A SOLID PROPELLANT MICRO-THRUSTER

Wayne Churaman

Dissertation directed by: Professor Sarah Bergbreiter  
Department of Mechanical Engineering

Energetic porous silicon has emerged as a novel on-chip energetic material capable of generating energy that can be harnessed for positioning of millimeter and micron-scale mobile platforms such as microrobots and nano-satellites. Formed by an electrochemical etching process, porous silicon is inert and only becomes reactive when nano-scale pores are infused with a liquid oxidizer such as sodium perchlorate. In this work, energetic porous silicon was investigated as an actuator for micro-propulsion by quantifying thrust and impulse produced during the exothermic reaction. Performance was measured as a function of porous silicon morphology, where morphology was characterized according to the porosity of the material. The baseline devices used in the study were individual two millimeter diameter porous silicon devices etched to a lateral target depth of 25  $\mu\text{m}$ . The pores were etched in a p-type, boron doped silicon wafer, and porosity was varied by changing the concentration of hydrofluoric acid (HF) and ethanol (EtOH) in the etchant solution, varying the porous silicon etch depth, and wafer resistivity. Thrust results were collected while varying the porosity

from 30 % to 75 %. The highest thrust and impulse values measured with a calibrated Kistler 9215 force sensor were 680 mN and 266  $\mu\text{N} \cdot \text{s}$ , respectively from a 2 mm diameter porous silicon device etched in a 3:1 etch solution to an etch depth of 30  $\mu\text{m}$  (72 % porosity). As a result of changing porosity, a 7x change in thrust performance and a 16x change in impulse performance was demonstrated. Impulse values were also validated using a pendulum experiment in which the microthruster was unconstrained.

Further studies evaluated the potential of porous silicon for multi-propulsion events. Limitations and trade-offs associated with propulsion event density were presented by studying the effects of scaling area on thrust performance, and characterizing simultaneous thrust when arrays of porous silicon micro-thruster devices were ignited simultaneously. In addition, the effects of sympathetic ignition were evaluated to better understand how closely propulsion events could be physically spaced on a 1  $\text{cm}^2$  chip. Finally, to further increase thrust, a process was demonstrated to fabricate a 3D printed nozzle and integrate it with porous silicon. The effects of confinement were evaluated by performing a parametric study, varying nozzle throat diameter, and divergent angle. It was shown that integration of a nozzle (throat diameter of 0.75 mm and a divergent angle of  $\theta$  measuring  $10^\circ$ ) resulted in approximately 4X increase in thrust, and 4X increase in impulse. This study highlighted enhancements to thrust and impulse based on an in-depth understanding of the material characteristics of porous silicon as a solid propellant, and identified trade-offs associated with achieving multiple propulsion events on a 1  $\text{cm}^2$  chip given the ability to do simultaneous ignition

and porous silicon device scaling.

INVESTIGATING ENERGETIC POROUS SILICON  
AS A SOLID PROPELLANT MICRO-THRUSTER

by

Wayne A Churaman

Dissertation submitted to the Faculty of the Graduate School of the  
University of Maryland, College Park in partial fulfillment  
of the requirements for the degree of  
Doctor of Philosophy  
2019

Advisory Committee:

Professor Sarah Bergbreiter, Advisor

Professor Don L. DeVoe

Professor Miao Yu

Assistant Professor Ryan Sochol

Professor Christopher Cadou - Dean's Representative

Christopher Morris Ph.D. (U.S. Army Research Laboratory)

© Copyright by  
Wayne Churaman  
2019

# Preface

## Foreword

## Dedication

I am so thankful for the blessings that Jesus Christ has bestowed upon me, and for the strength and wisdom that He has given me throughout my life. Even in the most difficult situations, I am reminded of a Bible verse in Philippians 4:13 that says, "I can do all things through Christ who strengthens me." I know that He has opened doors, and paved the way for me to achieve this major accomplishment in my life.

I would like to dedicate this Ph.D. to my beautiful wife, Helen Churaman, who deserves every bit of this Ph.D. because she has motivated and encouraged me every step along the way. She has been the voice of hope and reason many times when I felt like giving up and settling for less than what I was capable of accomplishing. Her constant motivation and much needed pushing has allowed me to cross this finish line in my academic career. Helen, I thank you for the sacrifices you made for me and for our family. We would not be here if I didn't have such an incredible wife and best friend. You have always been and will continue to be the loudest voice cheering me on. I love you.

To our son, Wesley Leonel Churaman... may you always know that you can achieve anything in life that you set your mind to. Always put God first in everything you do.

I would also like to dedicate this Ph.D. to my parents, Mr. Walter Churaman and Mrs. Sandra Churaman, how took an incredible leap of faith to leave the life they built together in our small homeland of Guyana, to venture to the United

States with myself (only 6 years old) and my younger sister, in hopes of giving us opportunities that were never afforded to them. My parents taught me the importance of hard work and dedication, and always striving for the best when it comes to living out the talents that God has blessed you with. I am so thankful for the countless sacrifices that they made for me, and for their continued love and support. My parents invested their time and love into my life, and encouraged me to keep striving even when things seemed impossible. This Ph.D. is for my father, the greatest man and engineer that I know, and for my mother, an incredible woman who has prayed me through lots of challenging situations in my life.

To my sister, Dr. Maria Churaman Diwanji, who motivated me to run faster and jump higher. Thanks for your encouragement and support.

To many others... my Grandmother (Yvonne Small), my Grandfather (Frank Allan Small), my Aunty Desiree Swamy, and my Aunt Agnes Dalgetty... and so many others who prayed for me every day and believed in me.

## Acknowledgments

I would like to acknowledge my colleagues at the U.S. Army Research Laboratory including members of the On-Chip Energetics and MEMS Team for their support and encouragement throughout the years. I would especially like to acknowledge Mr. Brian Isaacson for his fabrication expertise and for providing what seemed to be an endless number of silicon wafers to test. I would also like to acknowledge my mentors and countless individuals in leadership at the U.S. Army Research Laboratory for giving me the opportunity to pursue my PhD and for encouraging me to strive for the best.

I would also like to thank my advisor, Dr. Sarah Bergbreiter, for her guidance, support, and encouragement throughout this academic endeavor.

# Table of Contents

List of Tables	ix
List of Figures	xi
1 Introduction	1
1.1 Motivation	1
1.2 Generating Thrust	3
1.2.1 Microrobots Generating Thrust	4
1.2.2 Nano-satellites Generating Thrust	12
1.2.3 Summary of Thrust Generation	17
1.3 Porous Silicon	19
1.4 Research Goals	23
2 Repeatability of Fabrication and Characterization Methods	25
2.1 Introduction	25
2.2 Fabrication	25
2.3 Etch Repeatability	30
2.4 Force Measurement Repeatability	36
2.5 Oxidizer Loading	42
2.6 Conclusion	45
3 Effect of Morphology on Propulsion Performance	46
3.1 Introduction	46
3.2 Experimental Methods	46
3.2.1 Gravimetric Determination of Porous Silicon Porosity	47
3.2.2 Varying Concentration and Etch Depth of Porous Silicon Etch	50
3.2.3 Varying Resistivity of Silicon Wafer	51
3.2.4 Calculating Impulse and Specific Impulse	52
3.2.5 Measuring Impulse with Pendulum	52
3.3 Results	55
3.3.1 Concentration of Etch Solution	55
3.3.2 Porosity versus Etch Depth	57
3.3.3 Porosity versus Wafer Resistivity	61
3.3.4 Pendulum Validation of Impulse Measurements	63
3.4 Discussion	65
3.4.1 Use of Porosity instead of Surface Area and Pore Size in Porous Silicon	65
3.4.2 Thrust and Impulse based on Porosity	66
3.5 Conclusion	68

4	Scaling Effects for Multiple Thrust Events	70
4.1	Introduction	70
4.2	Scaling Microthrusters	71
4.3	Fabrication	74
4.4	Experimental Methods	76
4.4.1	Area Scaling Study	76
4.4.2	Simultaneous Ignition Study	76
4.4.3	Sympathetic Ignition Study	77
4.5	Results	79
4.5.1	Area Scaling Study	79
4.5.2	Simultaneous Ignition Study	82
4.5.3	Sympathetic Ignition Study	86
4.6	Discussion	91
4.7	Summary	95
5	Confining Thrust	96
5.1	Introduction	96
5.2	Silicon Nozzle	100
5.2.1	Fabrication Methods	100
5.2.2	Results	104
5.3	3-Dimensional Printed Nozzles	106
5.3.1	Fabrication and Parametric Design	106
5.3.2	Design Verification	108
5.3.3	Assembly and Testing	110
5.3.4	Results	112
5.3.4.1	Micro-CT Post-Ignition	112
5.3.4.2	Video Analysis	114
5.3.4.3	Force Measurements	116
5.4	Summary	119
6	Conclusions	121
6.1	Future Work	123
B	MATLAB	125
B.1	Experimental and Computational Background	125
	Bibliography	126

## List of Tables

1.1	Summary of Centimeter Scale Robotics . . . . .	12
1.2	Summary of performance metrics for micro-thrusters . . . . .	13
1.3	Summary of Jump Performance of Small-Scale Robots . . . . .	19
2.1	Volumetric analysis measurements performed on three separate silicon coupons, each consisting of 25 individual 2 mm porous silicon devices. Each coupon was placed at a different location in the etch beaker during the etch. . . . .	31
2.2	Volumetric analysis measurements performed on three separate silicon coupons, each consisting of 25 individual 2 mm porous silicon devices. Each coupon was placed at the same relative location in the beaker. . . . .	33
2.3	Summary of force and impulse measurements taken from three partially burned porous silicon devices. . . . .	34
2.4	Summary of peak force, and impulse based on different oxidizer loading amounts. . . . .	44
3.1	Results for varied electrolyte concentrations. The error is the standard deviation over 4 trials (3 trials for porosity). The equivalence ratio is based on the average porosity. . . . .	56
3.2	Results for varied etch depth. The error is the standard deviation over 4 trials (3 trials for porosity). The equivalence ratio is based on the average porosity. . . . .	58
3.3	Results as a function of wafer resistivity. The error is the standard deviation over 4 trials (3 trials for porosity). . . . .	62
4.1	Summary of nominal separation distance (in microns) between adjacent devices . . . . .	78
4.2	Summary of average impulse, and minimum and maximum impulse as a function of porous silicon area . . . . .	80
4.3	Summary of average force, and minimum and maximum force as a function of porous silicon area . . . . .	80
4.4	Summary of peak force and impulse for a single 4.8 mm <sup>2</sup> device in comparison to three 1.6 mm <sup>2</sup> devices connected in parallel and ignited simultaneously. Results from the first of two experiments shown. . . . .	84
4.5	Summary of average force, and minimum and maximum force as a function of porous silicon area . . . . .	88
4.6	Summary of propulsion event density, along with thrust and impulse measurements based on the number of micro-thrusters per cm <sup>2</sup> . . . . .	94

5.1	Table provides a comparison of intended nozzle design parameters with actual dimensions measured after fabrication using Micro-CT scans. . . . .	110
5.2	Table provides a comparison of intended nozzle design parameters with actual dimensions measured after subjecting the nozzle to the exothermic porous silicon reaction. . . . .	114
5.3	Summary of thrust performance for the different nozzle configurations. . . . .	119
5.4	Summary of impulse performance for the different nozzle configurations. . . . .	119

## List of Figures

1.1	SEM image of a flea with outstretched hind legs. (B) Drawing of the right hind leg and part of the thorax [1]. . . . .	4
1.2	Bio-inspired robot uses SMA springs to catapult itself 64 cm into the air [2]. . . . .	5
1.3	Side view illustration of the Mini-Whegs 9J showing both the retracted (top) and released (bottom) spring positions [3]. . . . .	6
1.4	Jumping robot uses a gearbox, including motor, gear wheels, cam, and pager motor to jump [4]. . . . .	7
1.5	Locust inspired jumping robot uses a motor and torsional spring to jump. . . . .	8
1.6	(A) Distortion of the water surface created by the legs. (B) As the robot is actuated, the legs do not penetrate the surface of the water [5]. . . . .	9
1.7	Schematic showing the three phases of jumping (1) equilibrium position (2) applied external force (3) immediately after take-off [6]. . . . .	10
1.8	SEM of jumping mechanism using elastomer springs [6]. . . . .	10
1.9	Micro-robot with legs held in place by electrostatic clamps and an elastomer used to store energy for motion [7]. . . . .	11
1.10	Schematic of a micro-thruster showing the chip with the embedded propellant and a separate chip with the igniter (B) SEM of a propellant chip [8]. . . . .	14
1.11	Thruster designed using explosive porous silicon [9]. . . . .	16
2.1	Illustration of the galvanic porous silicon etch process [10] . . . . .	26
2.2	Cross-sectional process flow illustrating the fabrication of porous silicon and oxidizer activation. . . . .	27
2.3	(A) Illustration of an array of 2 mm diameter porous silicon devices with bridgewires. (B) A scanning electron micrograph (SEM) of the cross section of a porous silicon device showing the metal bridgewire initiator and porous silicon undercutting the bridgewire as a result of the etch. . . . .	28
2.4	(Left) Single diced coupon consisting of four individual 2 mm diameter porous silicon devices (dark circular regions). (Right) A scanning electron micrograph (SEM) of an individual device showing a close-up of the center of the bridgewire. . . . .	29
2.5	Three separate etches performed in HF resistant beakers, where the silicon coupon was suspended at approximately the same location in the beaker using a blue clip, held in place with a notched plastic fixture . . . . .	32
2.6	Region of un-reacted porous silicon. White crystalline structures scattered across the chip are residual oxidizer crystals. . . . .	34
2.7	Force vs time generated for five un-annealed porous silicon devices. . . . .	35

2.8	Force vs time generated for four annealed porous silicon devices. . .	36
2.9	Experimental set-up used to evaluate force generated by energetic porous silicon. The Kistler 5010 converts charge signal from the piezo in the Kistler 9215A force sensor into voltage waveform. . . .	38
2.10	Image of the Kistler 9215A sensor and the M2 tap used to interface with the sensor. The porous silicon device was mounted on the M2 tap. . . . .	38
2.11	Experimental set-up (top: schematic, bottom: photo of actual test setup) used to measure force produced by porous silicon device. Devices are not drawn to scale. . . . .	39
2.12	Aluminum block was attached to the M2 tap to provide more surface area for mounting the porous silicon device. . . . .	40
2.13	Force output generated when porous silicon devices were attached using the modified M2 tap with aluminum block . . . . .	41
2.14	Force output generated when porous silicon devices were attached using the original M2 tap . . . . .	42
2.15	(top) High speed video frame capture showing flame generated by a single 2 mm diameter porous silicon device oxidized with 1 $\mu\text{L}$ of sodium perchlorate (bottom) Similar device oxidized with 6 $\mu\text{L}$ of sodium perchlorate. . . . .	43
2.16	Force versus time curves comparing oxidizer loading. . . . .	44
3.1	Figure showing the individual steps taken to evaluate porosity gravimetrically, including accounting for change in mass due to nitride and porous silicon etching. . . . .	48
3.2	Thrust profiles based on the varied electrolyte concentrations. . . .	57
3.3	Etch depth as a function of etch time. . . . .	58
3.4	Thrust profiles shown as a function of increasing etch depth. Etch depth varied from 10 $\mu\text{m}$ to 30 $\mu\text{m}$ by increments of 10 $\mu\text{m}$ . . . . .	59
3.5	Thrust profiles for six porous silicon devices etched 40 $\mu\text{m}$ deep. . .	60
3.6	(A) 30 $\mu\text{m}$ deep porous silicon sample without surface cracks (B) 40 $\mu\text{m}$ deep porous silicon sample showing surface cracks. . . . .	61
3.7	Thrust profiles based on the change in silicon wafer resistivity. . . .	62
3.8	Angular displacement of the pendulum captured on high-speed video. . . . .	64
3.9	Side by side images showing 9° of displacement upon actuation. . .	65
3.10	Comparison of impulse and peak thrust. . . . .	67
4.1	(Left) Silicon coupon consisting of three porous silicon devices with initiators connected in parallel (Right) Close-up of the initiator used to electrically ignite the porous silicon . . . . .	75
4.2	(Left) Illustration of a single 4.8 mm <sup>2</sup> porous silicon device. Illustration of three individual 1.6 mm <sup>2</sup> devices with individual bridgewires connected in parallel. (Right) Circuit schematic illustrating the resistor elements (bridgewire) for each porous silicon device. . . . .	77

4.3	Illustration of device spacing for sympathetic ignition study. . . . .	78
4.4	Plot of force versus time as a function of the porous silicon device area. Dashed lines represent average thrust, while solid lines represent upper and lower bounds of standard deviation. . . . .	80
4.5	Plot of force versus time as a function of the porous silicon device area for 7 $\mu\text{m}$ deep porous silicon etch. . . . .	81
4.6	Force versus time for single (4.8 $\text{mm}^2$ ) device versus three (1.6 $\text{mm}^2$ ) devices. Experiment repeated twice . . . . .	84
4.7	High speed frame capture of a single (4.8 $\text{mm}^2$ ) device reacting in comparison to three (1.6 $\text{mm}^2$ ) devices reacting simultaneously . . . . .	85
4.8	High speed video capture of series of 1.6 $\text{mm}^2$ devices etched for 30 seconds. . . . .	87
4.9	High speed video capture of series of 1.6 $\text{mm}^2$ devices etched for 30 seconds. . . . .	87
4.10	Still frames showing the sympathetic ignition of 3.2 $\text{mm}^2$ porous silicon devices etched for 3 minutes . . . . .	88
4.11	Summary of force and impulse as a function of porous silicon area plotted with error bars. . . . .	92
5.1	Illustration of micro-thruster fabricated with three wafers: chamber, igniter, and nozzle. Micro-thruster capable of producing up to 2.3 mN of force per device [11]. . . . .	97
5.2	Schematic of a micro-thruster showing the chip with a cavity for embedding propellant and a separate chip with the igniter. (B) SEM of the propellant chip [8]. . . . .	98
5.3	Assembled micro-thruster array consisting of (a) igniter layer, (b) chamber filled with BTATZ, and (c) the nozzle layer. Layers bonded together with silicone [12]. . . . .	99
5.4	Process flow illustrating fabrication of porous silicon device chip (a through e), cap chip (f through h), and the bonding of the two chips (i). . . . .	101
5.5	Fully assembled porous silicon device chip and cap chip. . . . .	102
5.6	Partial coverage of bond pad with solder after dipping process. . . . .	104
5.7	Comparison of confined versus unconfined thrust. . . . .	105
5.8	Summary of parameters varied in the design of the micro-thruster chamber and nozzle. . . . .	107
5.9	An array of printed micro-thruster chambers and nozzles with support structures. . . . .	108
5.10	Images of a micro-thruster printed with Form 2 taken with Keyence Microscope . . . . .	108
5.11	Images from micro-computerized tomography scan performed on 3D printed micro-thruster. . . . .	110

5.12	To make it easier to align the nozzle to the porous silicon chip, a ring of silicone was painted around the outer edge of the porous silicon device. Silicone was also painted on the bottom of the nozzle. . . . .	112
5.13	3D printed nozzle attached to oxidized porous silicon device and mounted to force sensor. . . . .	112
5.14	Images from micro-computerized tomography scan performed on 3D printed micro-thruster after nozzle were subjected to porous silicon burn. . . . .	114
5.15	(left) Porous silicon reaction without a nozzle (right) and one with a nozzle. . . . .	116
5.16	3D printed nozzle attached to oxidized porous silicon device and mounted to force sensor. . . . .	116
5.17	Force versus time curves for different micro-thruster nozzle configurations evaluated. . . . .	117
5.18	Force versus time curves for different micro-thruster nozzle configurations evaluated showing average force plus and minus the standard deviation. . . . .	118

# Chapter 1

## Introduction

### 1.1 Motivation

Achieving effective and efficient locomotion through propulsion provides a useful capability for many systems by enabling position and trajectory correction, and providing a mechanism for traversing rough terrain and overcoming obstacles. Systems such as nano-satellites and microrobots can propel themselves by generating thrust, which can generally be achieved by converting stored chemical energy to mechanical energy (as with an energetic material), or through energy produced by a motor-spring system [13, 14]. Both mechanisms for generating thrust rely on the rapid release of stored energy.

At smaller scales ( $< 1$  cm), integration of these thrusters can be complex given size, weight, and power constraints. Novel thrusters are required to meet these constraints while still producing useful thrust, ideally with the ability to generate multiple thrust events. For example, the 30 cm, 2 kg robot described in [15] can search for victims under the rubble of a collapsed building by propelling itself over rocks and boulders. The concept of a pneumatic cylinder is not easily scaled to sizes below 1 cm though. Therefore, the goal of this work is to study how propulsion can be achieved at smaller size scales while better understanding the trade-offs between thrust generated and propulsion event density.

This study builds on previous work that was demonstrated in the author's Master's Thesis entitled, "Novel Integrated System Architecture for an Autonomous Jumping Micro-Robot," [16] where the author demonstrated jumping locomotion of a fully autonomous hexapod microrobot that was equipped with on-board power, sensing, and actuation. Propulsion of the hexapod, designed on a 4 x 7 mm<sup>2</sup> polymer chassis, was achieved using energetic porous silicon as a micro-thruster, which produced 246  $\mu$ J of kinetic energy and propelled the microrobot to a vertical jump height of 8 cm using only the energy stored in a small surface mount 10  $\mu$ F capacitor to ignite the porous silicon. The porous silicon was infused with an oxidizer (sodium perchlorate) to produce an exothermic reaction that converted stored chemical to kinetic energy.

While this was a unique accomplishment because of the novel integration of the porous silicon propellant into the bulk silicon and the level of autonomy that was achieved [17], little was understood about scaling thrust and impulse as a function of the material properties of the porous silicon. Previous work did not address multiple propulsion events and the trade-offs between area of propellant, density of propulsion events on a single chip, or the effects of confinement. In this dissertation, the author carefully studied the effects of the porous silicon morphology on thrust and impulse, and the effects of scaling area of energetic porous silicon on thrust and the trade-offs associated with achieving multiple propulsion events. The author demonstrated fabrication of three dimensional printed nozzles and performed a parametric study to understand the effects of confinement on thrust performance.

## 1.2 Generating Thrust

Generating thrust is useful for a number of applications where an object must be propelled or launched from rest. In this work the author focused on how thrust could be harnessed for systems like microrobots and nano-satellites to understand how thrust can be scaled and the trade-offs associated with propulsion event density [18, 19, 20]. Small jumping robots need to overcome force velocity limitations of motors when generating thrust, and generally rely on motor-spring systems for thrust generation. For example, the jumping Grillo robot, measuring 50 mm long, requires approximately 5 W of instantaneous power to be delivered to the rear legs for a jump. This power is generated from elastic energy in two separate springs stored by a motor driving 0.3 W [21].

Alternatively, nano-satellites rely on the conversion of chemical to mechanical energy, or potential to kinetic energy to produce thrust. The amount of stored chemical energy that a CubeSat can carry at launch is limited to 100 W-Hours, which is equivalent to 360 kJ [22]. These systems may require valves for mixing fuel and propellant to increase mission life and safety. The amount of thrust needed by microrobots and nano-satellites is determined by the overall size of the platform and the number of propulsion events needed during operation. A closer look is taken to better understand how these two systems generate thrust.

## 1.2.1 Microrobots Generating Thrust

The inspiration for microrobots that can propel themselves over obstacles comes from some of nature's best athletes, particularly the flea. The flea can jump to heights more than 100 times its body length because of a mechanism that acts as a catapult, which stores elastic energy and quickly releases that energy by torque reversal triggering [2]. Figure 1.1 shows a scanning electron micrograph (SEM) of a flea with outstretched hind legs and a drawing of the right hind leg and part of the thorax, showing the joint and skeletal reinforcements.

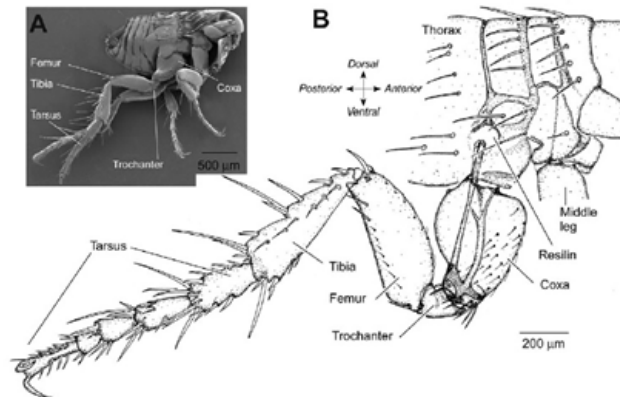


Figure 1.1: SEM image of a flea with outstretched hind legs. (B) Drawing of the right hind leg and part of the thorax [1].

The flea's ability to jump inspired the miniature robot shown in Figure 1.2, which is approximately the size of a coin with a 26.5 mm diameter [2]. The robot uses three shape memory alloy (SMA) springs to function as artificial muscles. The SMA can also act as the resilin pad, which is the elastomer through which elastic energy is stored. SMA springs provide high power-mass density, and operate in such a way that the direction of the actuation force can be changed [2].

The flea inspired robot, whose body is made by layering sheets of copper laminated Kapton (polyimide) and glass fiber, can jump 64 cm when 0.6 A of current is applied to the SMA wires.

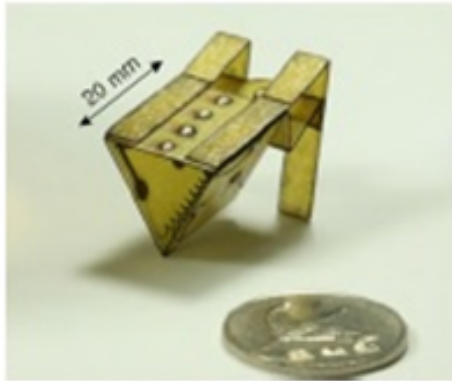


Figure 1.2: Bio-inspired robot uses SMA springs to catapult itself 64 cm into the air [2].

The Mini-Whegs is considered a small robot measuring 10.4 cm in length with the ability to run and jump using a single propulsion motor drive train and steering components, which interface with an on-board radio control unit [3]. Because the platform is not at the millimeter scale, it is manually assembled and uses commercial off-the-shelf (COTS) components for actuation. Assembly of the system is achieved using an upper and lower shell made of *Delrin*<sup>®</sup> that is held together by a set of nylon screws. The components are positioned vertically beneath the shell and held in place by short internal walls. Jumping is achieved through the use of a spring and carefully designed linkages shown in Figure 1.3 to ensure greater stiffness and minimize internal friction. With a controllable jumping mechanism, it can leap as high as 18 cm.

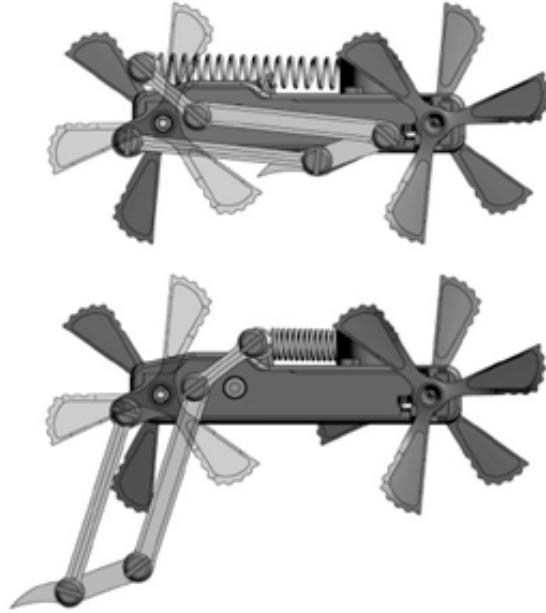


Figure 1.3: Side view illustration of the Mini-Whegs 9J showing both the retracted (top) and released (bottom) spring positions [3].

The 5cm, 7g jumping robot designed in [4] is capable of jumping over obstacles 27 times its own size. Shown in Figure 1.4, the jumping robot consists of a gear box, which includes a motor, gearwheels, and cam. To release the energy needed during the acceleration phase of the jump, the robot uses a small pager motor to actuate the cam and rotate the leg lever arm. This process slowly charges and stores energy in two torsional springs connected to the main legs, which can be released on demand. To recharge the mechanism for one jump cycle in 3.5 s, 352 mW of power is consumed at 3.7 V. While this robot requires relatively low power, implementing a similar mechanical design at reduced size scale poses a challenge to both assembly and integration.

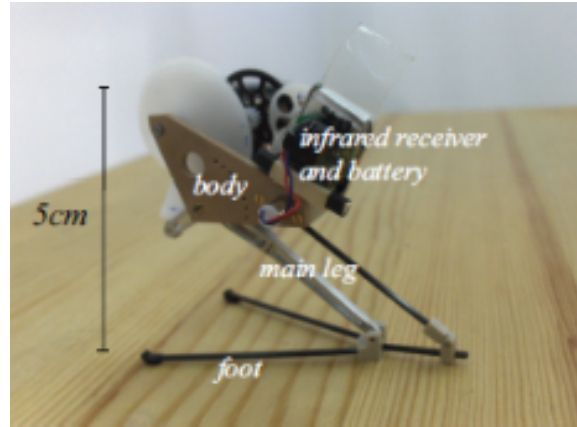


Figure 1.4: Jumping robot uses a gearbox, including motor, gear wheels, cam, and pager motor to jump [4].

Similar to the jumping robot in [4], the locust-inspired jumping robot shown in Figure 1.5 is approximately the size of an adult dessert locust that can range in length from 50 to 60 mm. The robot, weighing 23 g, can achieve jump heights of up to 3.35 m, while covering a distance of 1.37 m by cocking a torsional spring. This is done by “wrapping a tendon-like wire around the shaft of a miniature motor” [14]. The leg structures are designed out of carbon rods, and the motor is driven by a Li-Po battery. The maximum available torque is 0.08 Nm, when operating at 4.8 V.

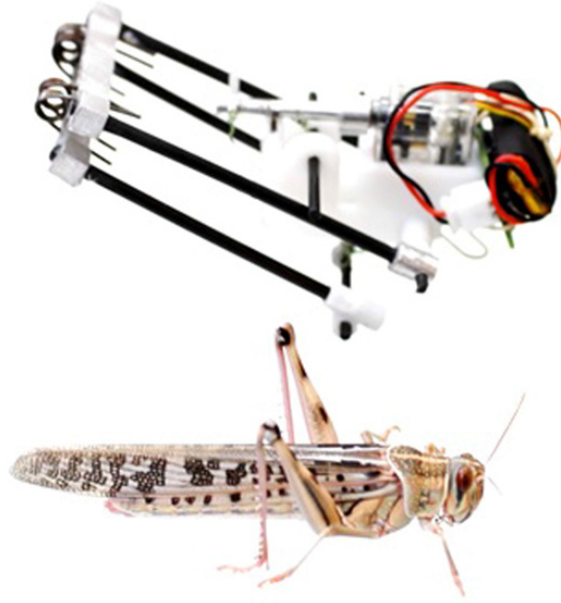


Figure 1.5: Locust inspired jumping robot uses a motor and torsional spring to jump. [14]

At smaller and smaller size scales, jumping becomes a more challenging feat to achieve. The 68 mg at-scale jumping robotic insect in [5], measuring 2 cm in body length, mimics the locomotion found in water striders. It has been shown that water striders "rotate the curved tips of their legs inward at a relatively low descending velocity with a force just below that required to break the water surface (144 mN/meter)" [5]. In order to mimic the water strider, the jump must generate large momentum and take-off velocity to move from the surface of the water. The robot shown in Figure 1.6 uses flexure hinge-based composites. Actuation of the hinges is achieved using a sheet nickel titanium (NiTi) shape memory alloy actuator. The actuator is 100  $\mu\text{m}$  wide, 80  $\mu\text{m}$  thick, and 1 mg in weight. Results show that the robot can attain an initial velocity of 1.6 m/s with a jump height of 142 mm while producing a maximum reaction force of 9.27 mN

[5].

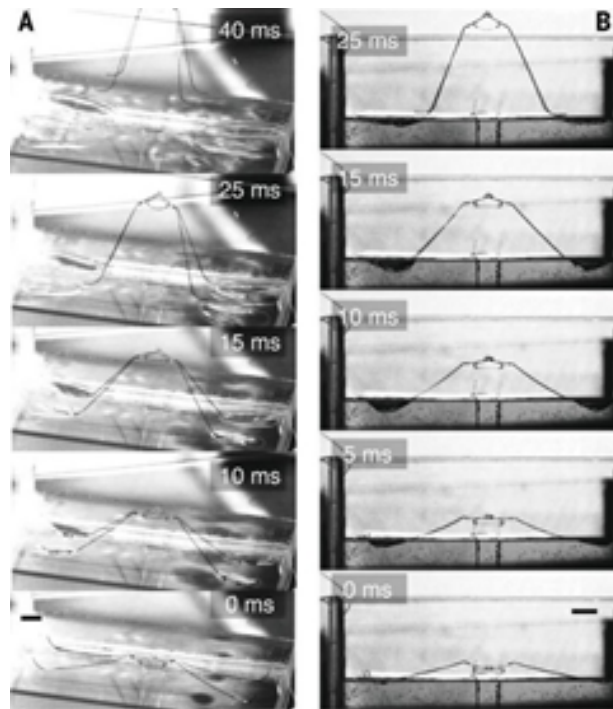


Figure 1.6: (A) Distortion of the water surface created by the legs. (B) As the robot is actuated, the legs do not penetrate the surface of the water [5].

Locomotion at the micro-scale has been demonstrated in [6], where the robot consists of two rigid masses that are connected by elastomer springs shown in Figure 1.7 and Figure 1.8. The robot leg is located in the center of the device, while the U-shape structure is the body. Compression of the structure results in the spring undergoing a strain, which represents potential energy. Upon release of the structure, the spring is unloaded and kinetic energy propels the robot upward. The overall size of the robot is 4 mm x 4 mm. When actuated, the robot can reach heights of 32 cm, which is 80 times its own height.

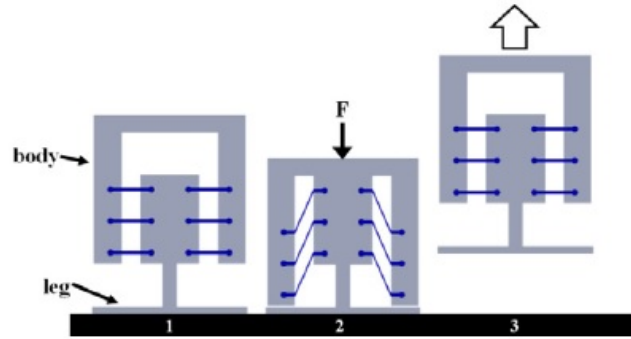


Figure 1.7: Schematic showing the three phases of jumping (1) equilibrium position (2) applied external force (3) immediately after take-off [6].

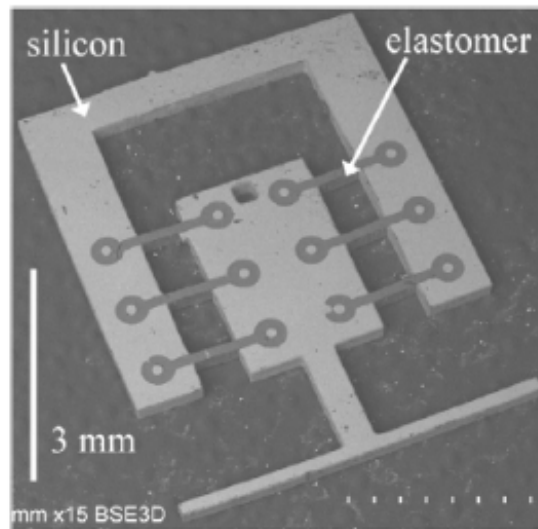


Figure 1.8: SEM of jumping mechanism using elastomer springs [6].

Similar to robots, the electrostatic inchworm motor described in [7] is an example of thrust demonstrated at small scales. The motor can store 4.9 nJ of energy into a micro-rubber band. The micro-rubber band, or elastomer, represents the energy storage system, while the electrostatic inchworm motor is the actuator used to quickly release the energy upon activation. The electrostatic inchworm motor is comprised of multiple sets of gap closing arrays (GCAs); two drive ar-

rays that move the shuttle mass forward, and two clutch arrays that connect the drive actuator to the shuttle [7]. Figure 1.9 shows a robot prototype with legs being held in place by electrostatic clamps and an elastomer connected to the robot body frame. For this application the actuator requires a long throw of 5 mm and a force of 10 mN. When the elastomer is released, the leg propels a 0402-sized capacitor with a mass of approximately 0.6 mg some 1.5 cm along a glass slide. For this particular demonstration, there was 1.2  $\mu$ J of stored and clamped energy, which corresponds to a vertical jump of 1.2 cm.

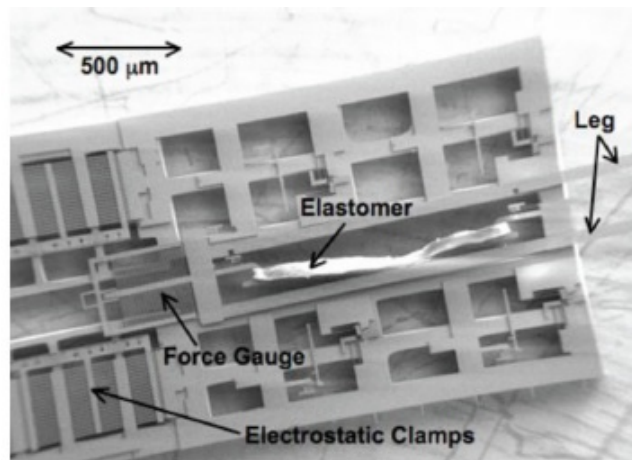


Figure 1.9: Micro-robot with legs held in place by electrostatic clamps and an elastomer used to store energy for motion [7].

Biological systems will continue to inspire tremendous breakthroughs in the design and implementation of small scale robots. Table 1.1 summarizes the size, weight, type of locomotion, and actuation mechanism for several centimeter scale robots. In several instances, the robots are referred to as micro-robots when in actuality they are centimeter in scale.

Table 1.1: Summary of Centimeter Scale Robotics

Robot	Size	Locomotion	Actuation	Weight
Mini-Whegs [3]	10.4cm length	Run, Jump	Motor, Spring	191.4g
Leg-in-Rotor [15]	300mm x 300mm	Roll, Jump	Pneumatic	>2kg
Scout [23]	40mm dia., 115mm length	Roll, Jump	Servo, Spring	200g
Hopping Robot [4]	10's of cm	Jump	Motor, Spring	450kg
Sandia [24]	0.1m x 0.1m x 0.2m	Jump	Chemical	2.5kg
TAUB [14]	50-60 mm length	Jump	Motor, Spring	23g
Micro-robot [25]	77 mm cube	Jump	Solenoid	>200g

All of these robots require motors or other external forces to store energy in a spring or elastomer material, which is then released for a jump. However, motors require on-board power for operation, which means that the robot must be large enough to accommodate the battery, or be tethered to an off-board power supply. Achieving multiple jumps, while possible with some of the robots discussed, requires power to reset the motor, and replenish energy that was expended or released from the spring/elastomer.

### 1.2.2 Nano-satellites Generating Thrust

Thrust can also be generated by converting stored chemical energy into mechanical or kinetic energy. Devices that rely of this method of energy conversion are typically referred to an micro-thrusters and this approach is commonly used by nano-satellites to maneuver in space. A number of chemical and electrical micro-thrusters, such as solid propellant, vaporizing liquid, colloidal, and cold gas micro-thrusters have been previously demonstrated in [26, 27, 28, 29, 30]. Table 1.2 compares several previously reported or deduced performance metrics for

different types of thrusters.

Table 1.2: Summary of performance metrics for micro-thrusters

Type	Peak Thrust (mN)	Impulse ( $\mu\text{N} \cdot \text{s}$ )	Specific Impulse (s)
Colloid [29]	0.0012-0.00485	-	-
Colloid [31]	0.004	-	200
Colloid [32]	0.0003	-	300
Monopropellant	150	-	-
Solid Propellant [33]	0.1-1	170-1130	-
Solid Propellant [8]	50-340	21.1-115	3-15
Solid Propellant [34]	0.1	100	-
Solid Propellant [18]	10-15	-	15
Solid Propellant [35]	35	-	42
Solid Propellant [9]	-	140000	-
Solid Propellant (this work)	674	271	333
Vaporizing Liquid [28]	0.15-0.46	-	-
Vaporizing Liquid [36]	0.005-0.120	-	-
Vaporizing Liquid [37]	0.034-0.068	670-1400	3.4-6.9
Cold Gas [38]	1	100	-
Cold Gas [39]	55	550	65
Cold Gas [39]	46	-	43
Hybrid Cold-Gas [30]	0.1-0.10	-	45
Pulsed Plasma [39]	0.006	-	300
Pulsed Plasma [40]	-	57	1500
Pulsed Plasma [41]	1.4	750	1150

Table 1.2 does not represent the entirety of micro-thruster devices that exist in this field, but rather it is a best effort attempt to summarize some of the performance metrics that are available in literature. Each type of thruster has unique design constraints and capabilities.

Chemical thrusters offer the advantage of large peak thrust but are energy limited given the fixed amount of chemical reactants. Integration of the propellant with the thruster can also be a unique challenge as size scales approach smaller and smaller dimensions. The solid propellant thruster demonstrated by

Zhang et al [8] uses a gunpowder-based solid propellant, with 90 % gunpowder, 6 % ammonium perchlorate, 3 % aluminum, and 1 %  $\text{Fe}_2\text{O}_3$  to produce peak thrust of 340 mN at sea level, while achieving an impulse of  $115 \mu\text{N} \cdot \text{s}$ . As highlighted in [8], the micro-thruster shown in Figure 1.10, has the advantage of not requiring an elaborate system of pumps, valves, and fuel lines, which aide in the miniaturization of the overall system. Because it uses a solid propellant, the chances of propellant leakage is minimized. The propellant must be manually loaded into the chamber and the lid attached to confine the propellant. Ignition is achieved using a titanium (Ti)/gold (Au) metal resistive heating element with an ignition delay of 12.94 seconds and 2.07 J of input energy.

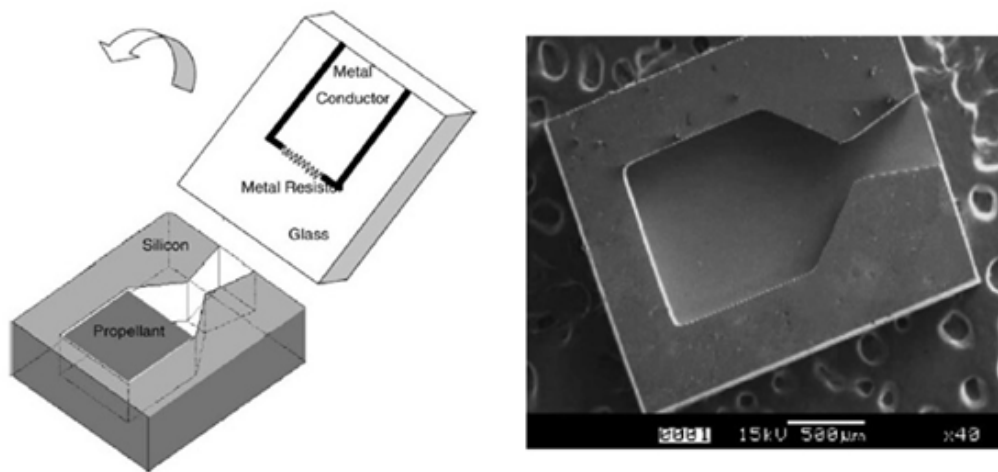


Figure 1.10: Schematic of a micro-thruster showing the chip with the embedded propellant and a separate chip with the igniter (B) SEM of a propellant chip [8].

The solid propellant thruster in [9] produces a relatively large impulse of  $0.14 \text{ N} \cdot \text{s}$  using nanocrystalline porous silicon as a propellant, but also relies on a strong explosion that destroys the silicon chip and limits its use. The porous silicon is fab-

ricated using an electrochemical anodic etch with hydrofluoric acid and ethanol electrolyte. An external power supply is used to drive the formation of porous silicon. After etching, the porous silicon is oxidized by immersing the device in an excessive amount of sodium perchlorate for a variety of times ranging from a few minutes up to several hours. Once activated, ignition is achieved using a 100 nm thick aluminum film, which is deposited onto the unpolished side of a wafer. Two copper wires are attached to the aluminum film using a conductive paint. The thruster is designed by attaching the porous silicon sample to plastic plates using silver paste and then attaching the nozzle tube onto the plate with blue tack. Figure 1.11 shows both a schematic and actual picture of the system. The inner diameter of the tube is 3 cm, with a wall thickness of 2 mm, and a length of 2.5 cm. The diameters of the nozzles range from 0.4 to 3 cm, with an overall system mass ranging from 32.5 to 30.2 g respectively.

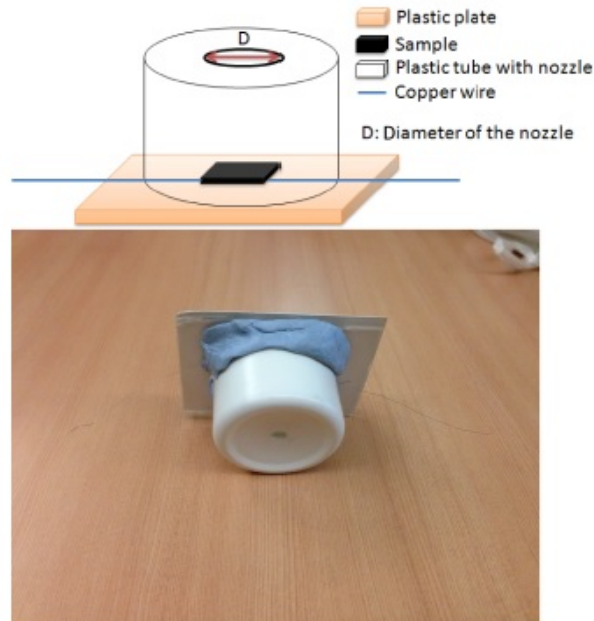


Figure 1.11: Thruster designed using explosive porous silicon [9].

The micro-thruster in [42] is a planar 2-D liquid mono-propellant micro-thruster fabricated using co-fired ceramic tapes with ignition achieved by electrolysis. The volume of the combustion chamber measures 820 nL. Triggered through the decomposition of hydroxlyammonium nitrate, thrust output of 150 mN at 45 V has been measured. The bi-propellant micro rocket in [43] is micromachined from silicon and measures 20 x15 x 3 mm in size. The engine can produce approximately 15 N of thrust with a specific impulse of 300 seconds.

Electrical thrusters offer high specific impulses without the complexity of propellant integration at smaller scales, but require energy to be delivered from a separate source (versus the propellant itself). The colloid thruster in [31] can produce a specific impulse in the hundreds of seconds, which is desirable for nano-spacecraft applications. Colloid-based micro-thrusters generally require

large voltages to provide electrostatic acceleration of charged liquid droplets for propulsion. The pulsed plasma microthruster in [40] generates the largest specific impulse of the devices reviewed, reaching values of 1500 s. These devices require the formation of a plasma by generating an electrical arc passing through a fuel.

Several of the micro-thrusters discussed above rely on stored chemical energy, either as a liquid or solid propellant, which is converted to mechanical energy through mixing with an oxidizer. The ability to generate thrust is determined by how effectively fuel and oxidizer can be mixed to produce an exothermic reaction, which generates gas and possible pressure wave. Integrating these chemically energetic systems on a nano-satellite can increase the complexity of the overall system design. Like the motor-spring mechanism used to generate thrust on microrobots, the chemical energy associated with micro-thrusters is depleted after each thrust event, and multiple sources of stored chemical energy must be available to increase thrust event density. In this work, the author studied energetic porous silicon as a solid propellant micro-thruster and the effects of scaling thrust and the limitations of thrust event density.

### 1.2.3 Summary of Thrust Generation

In an attempt to compare the performance of several jumping robots to that of chemical and electrical micro-thrusters discussed above, Table 1.3 shows calculated impulse generated by several robots. The impulse (J) calculated is a function

of the robot mass and the change in velocity generated during a jump as shown in Equation 1.1. The change in velocity is calculated in Equation 1.2 where acceleration is due to gravity. Given the jump height or distance ( $d$ ), time can be solved in Equation 1.3. The achievable impulse varies with the mass of the robot. The impulse generated by the larger robots in [3, 23] is comparable to that generated by the solid propellant micro-thruster discussed in [9], which is on the order of 100's of  $\text{mN} \cdot \text{s}$ . The microrobot with the elastomer actuator represents the smallest design with an impulse of  $20 \mu\text{N} \cdot \text{s}$ , which is comparable to the impulse generated by the solid propellant in [8] and the plasma thruster in [40]. While similar performance metrics can be achieved whether designing a micro-thruster for jumping to mimic biology or to maneuver a satellite, the goal remains to develop micro-thrusters to enable the miniaturization of these platforms. They have their own set of unique challenges in terms of integration and power consumption. Design trade-offs must be made to increase functionality and in many cases achieve autonomy.

$$\vec{J} = m \cdot \Delta\vec{V} \quad (1.1)$$

$$\Delta\vec{V} = \vec{g} \cdot t \quad (1.2)$$

$$d = \frac{1}{2}gt^2 \quad (1.3)$$

Table 1.3: Summary of Jump Performance of Small-Scale Robots

Robot	Actuator	Weight (kg)	Jump	
			Height (m)	Impulse
Mini-Whegs [3]	Metal helical spring	0.191	0.18	358 mN · s
Scout[23]	Metal bending spring	0.2	0.3	485 mN · s
Miniature Jumper [44]	Torsional spring	0.007	1.35	36 mN · s
Glumper [24]	Torsional spring	0.7	1.17	3.35 mN · s
Jollbo [24]	Bending spring	0.465	0.184	51 mN · s
Jumping robot [6]	Elastomer	8e-6	0.32	20 $\mu$ N · s

### 1.3 Porous Silicon

Silicon has and continues to be the most widely used substrate for the fabrication of integrated circuits and micro-electro-mechanical systems (MEMS). When converted into a porous film through an electrochemical etching process, the material has tremendous optical and thermal properties that have been used in the development of devices such as chemical sensors and optical waveguides [45, 46]. Porous silicon is a sponge-like structure that has a large specific surface area (901 m<sup>2</sup>/g) [47]. Some of the earliest work on porous silicon was produced more than 50 years ago through research conducted at Bell Labs where scientists performed electrolytic etching of n-type silicon, which was aided by illumination of the substrate to provide holes that drove etching [48].

Porous silicon as an energetic material was not discovered until 1992, when it was reported that potassium nitrate or nitric acid could react with porous silicon to produce an explosive-like reaction. The phenomenon occurred as re-

searchers were investigating the chemiluminescence of anodized silicon when a concentrated drop of nitric acid came into contact with freshly etched porous silicon [49]. Later in 2001, similar reactions were observed when porous silicon was placed in liquid oxygen. Finally in 2002 researchers reported that after scratching a porous silicon chip that was impregnated with gadolinium nitrate, the chip blew up [50]. These discoveries led to increased efforts to understand and exploit the energetic behavior of porous silicon. The reaction is made possible because of the high surface area silicon that serves as a fuel which is then infused with oxygen through the application of an oxidizer that penetrates into the pores. The porous silicon plus oxidizer system can be initiated with either heat, friction, or focused light [51].

Propellants and pyrotechnics, like energetic porous silicon, are typically composed of fuel and oxidizer, and energy density can be maximized by adjusting the fuel to oxidizer ratio. Reaction rates are lower than explosives, because they are dominated by kinetic diffusion [52]. Diffusion of oxidizer in the pores is influenced by pore shape and interconnectivity [53], and reaction rates are dependent on diffusive transport into the pores. Embedding oxidizer into the nanopores to increase oxidizer pore filling remains a challenge due to inadequate infiltration into the porous network. Due to the randomness of the porous silicon, very few methods can be used to analyze and characterize diffusion. Some of these methods include gas sorption, cryo-porometries, and imaging with micro-computed tomography. But even with these techniques, useful statistical data is difficult to acquire from pores below 100 nm in size [53].

Because of the challenges associated with modeling and characterizing kinetic diffusion due to the size of the pores, this study does not address reaction transport despite its importance to understanding thrust from porous silicon. A thorough understanding of these kinetic effects requires a model of the pore networks that takes into account heat and mass transfer, as well as surface adsorption kinetics, and this continues to be a challenge in the field [54].

Average combustion rates up to 3050 m/s in porous silicon with a specific surface area of 840 m<sup>2</sup>/g and porosity ranging from 65 % to 67 % were demonstrated in [10]. The combustion rate was measured using microfabricated diagnostic bridgewires in conjunction with high speed video captured at up to 930,000 frames per second; the microfabricated bridgewires were patterned on the porous silicon such that the reaction propagation front would physically break the bridgewires showing electrical discontinuity on an oscilloscope. The etch depth varied from 65 μm to 95 μm, and pore size varied from 2.4 to 2.9 nm. The combustion rates appear to depend on surface area and pore size, which affects kinetic diffusion during the exothermic event.

Much lower reaction rates of 94 m/s (with a standard deviation of 7 m/s) were demonstrated in [55], with porous silicon etched with 10 % HF concentration, porosity of 72.2 %, and pore size of 6.4 nm (1.7 nm standard deviation). This reaction rate was measured using fiber-optic velocity probes and highspeed video. The reaction rates are an order of magnitude larger than those measured in [10] even for porous silicon having similar porosity. The significant difference in reaction rates measured might be due to the high surface area achieved in [10].

The larger pore sizes in [55] should indicate smaller surface area, which is a relative measure of how much fuel is near the oxidizer. Therefore lower reaction rates should result from decreased surface area.

Fabrication of porous silicon is compatible with micro-fabrication techniques and can be incorporated with MEMS to provide an energy source on-chip. The energy output can be tuned by changing the morphology for enhanced performance in terms of achievable thrust and impulse. As a result, energetic porous silicon is a viable material for achieving propulsion, which has been successfully demonstrated in work published by the author in the Journal of Microelectromechanical Systems [56] showing the propulsion of a 318 mg hexapod robot to a vertical height of 8 cm. This was demonstrated without looking at the effects of varying the morphology of the porous silicon. It has been shown that the exothermic reaction generated by oxidized porous silicon is highly dependent on the morphology of the sponge-like material, which includes parameters such as surface area and porosity. It was shown in [57] that the specific surface area of porous silicon can vary between 191 and 901  $\text{m}^2\text{g}^{-1}$ , and porosity can range between 49 and 80 %. The rate at which the porous silicon burns upon ignition spans some three orders of magnitude from 5.2 to 1950  $\text{ms}^{-1}$  according to [57]. Energy densities up to 22.5  $\text{kJg}^{-1}$  have been demonstrated for porous silicon with 75 % porosity [57]. In addition to the material being highly tunable, it can be integrated alongside a MEMS device using conventional micro-machining techniques as demonstrated in [58] where the porous silicon was integrated with a MEMS acceleration switch.

## 1.4 Research Goals

In this work, energetic porous silicon was explored as a micro-thruster for propulsion by first characterizing the effect of porous silicon morphology on the force and impulse generated. The morphological properties studied include porous silicon porosity, which was varied by changing the lateral porous silicon etch depth, the concentration of the electrolyte etch solution, and the resistivity of the silicon wafer. The author performed force measurements to quantify thrust and impulse based on these properties.

The author also studied the effects of scaling the area of energetic porous silicon and critical device spacing to prevent sympathetic ignition of adjacent porous silicon devices to understand both thrust performance, along with limitations and trade-offs of propulsion event density and available thrust events on a  $1 \text{ cm}^2$  chip. The effects of area scaling and simultaneous ignition on thrust were also studied to understand how thrust performance could be enhanced by igniting multiple thrust events on a single chip.

The effects of confining the energetic porous silicon reaction with a nozzle was studied and the author presented two different approaches to confine the gas produced by the exothermic reaction for the purpose of showing enhancement to thrust performance. The first approach involved confining the gas using a silicon capping chip that was designed with a chamber and orifice. The two chips were bonded using a low temperature solder dipping process, which presented a number of integration challenges associated with chip bonding and attachment.

As a result, the author demonstrated an alternative fabrication approach in which the nozzle was three dimensional printed using a a Formlabs Form 2 printer. The author performed a parametric study to analyze thrust performance as a function of varying the physical properties of the chamber and nozzle. The author varied the throat diameter, and the divergent angle  $\theta$ . A comparison of thrust and impulse performance was done to quantify the effects of integrating the nozzle.

## Chapter 2

### Repeatability of Fabrication and Characterization Methods

#### 2.1 Introduction

To evaluate energetic porous silicon as a micro-thruster, it was important to ensure the repeatability of the etch process by maintaining control over the porosity and pore structure across the porous silicon devices that were fabricated and tested in this study. Additionally the repeatability and accuracy of the measurement system used to capture the force data was studied prior to collecting statistically significant data about porous silicon performance as a micro-thruster. Special attention was given to the method and configuration used to mount the porous silicon chip to the force sensor.

#### 2.2 Fabrication

Porous silicon was fabricated using a galvanic etch process discussed in [10] and illustrated in Figure 2.1, which does not require a customized etch cell or an external power supply. Figure 2.2 shows the cross-sectional fabrication process flow for an individual porous silicon device. Prior to etching, a p-type, boron doped wafer was coated on both sides with a low pressure, chemical vapor deposited (LPCVD) nitride. Wafers with the nitride coating were purchased from Rogue

Valley Microdevices, Inc. The nitride served as a hydrofluoric acid (HF) resistant etch mask. The nitride was first removed from the backside of the wafer using a Unaxis VLR 700 etch tool, and then a 170 nm thick platinum (Pt) layer was deposited onto the backside of the wafer. The resistivity of the wafer was measured prior to the Pt deposition using a 4 Dimensions Model 280 4-point Probe/Sheet Resistivity Measurement System. The Pt was important to the galvanic etch process, because etching relies on ionic charges (reduction at the Pt cathode, and oxidation at the Si anode) to drive formation of the porous silicon.

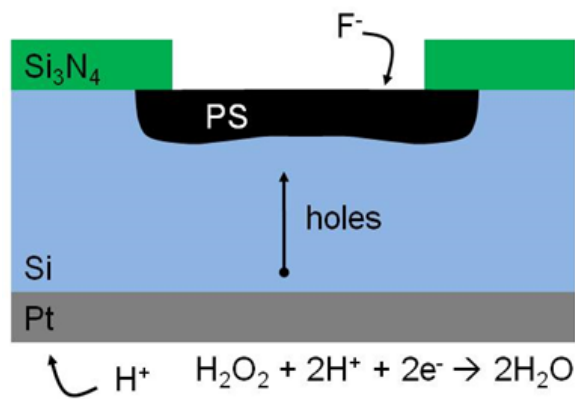


Figure 2.1: Illustration of the galvanic porous silicon etch process [10]

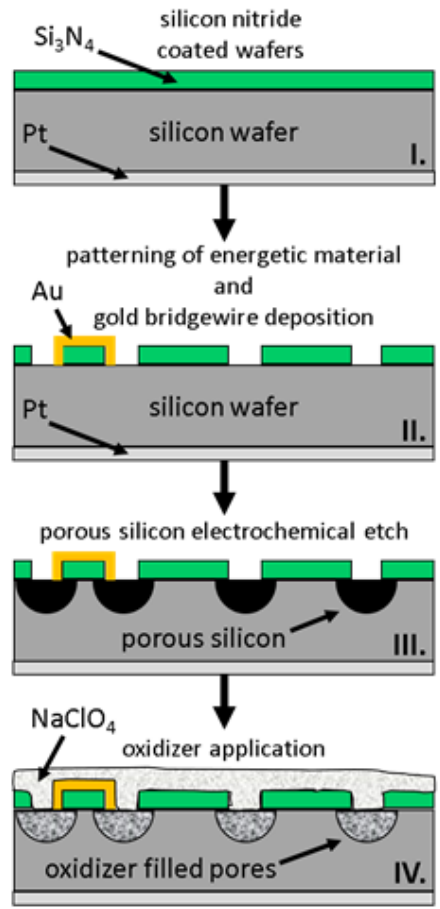


Figure 2.2: Cross-sectional process flow illustrating the fabrication of porous silicon and oxidizer activation.

On the side of the wafer where nitride remained, an array of 2 mm diameter, circular devices was lithographically patterned using a Karl Suss MA6/MB6, and the nitride was etched using a reactive ion etch (Unaxis VLR 700) to open windows of exposed silicon. After patterning the array of devices, an electronic initiator was lithographically patterned, and a metal stack consisting of 100 Å Cr, 1000 Å Pt, and 3800 Å Au was evaporated (Evatec BAK 641 E-beam Evaporator) and patterned by lift-off. The metal stack was chosen to ensure low electrical resistance, and therefore low ignition voltage.

The electronic initiator or bridgewire, shown in Figure 2.3, was 9 mm in length by 200  $\mu\text{m}$  in width, with a tapered section in the middle that measured 100  $\mu\text{m}$  in length by 25  $\mu\text{m}$  in width. Ignition via Joule heating required approximately 20  $\mu\text{J}$  of energy. The initiator was connected to 2 mm by 2 mm square bond pads (not shown), allowing wire leads to be soldered, and porous silicon to be ignited once activated with sodium perchlorate.

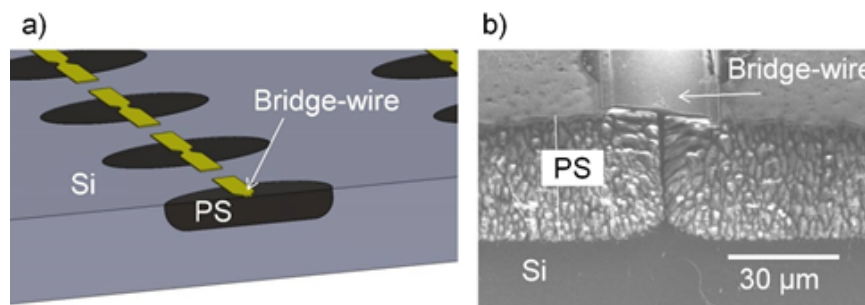


Figure 2.3: (A) Illustration of an array of 2 mm diameter porous silicon devices with bridgewires. (B) A scanning electron micrograph (SEM) of the cross section of a porous silicon device showing the metal bridgewire initiator and porous silicon undercutting the bridgewire as a result of the etch.

Before etching the porous silicon, the wafer was coated with a layer of photoresist and diced into smaller pieces, called coupons, using a Disco DAD 3240 dicing saw. Each coupon consisted of 4 individual 2 mm diameter devices. Prior to the etch, a wafer pre-clean was performed with acetone, methanol, and deionized water to remove photoresist. Individual coupons were etched by submerging the coupon in an etch bath consisting of a mixture of HF, ethanol (EtOH), and hydrogen peroxide ( $\text{H}_2\text{O}_2$ ). The HF and EtOH volumetric ratio was 3:1, and the amount of  $\text{H}_2\text{O}_2$  was 2.4 % of the total HF and ethanol volume. The etch ratio was later varied to look at the effects of changing the etch ratio on the structure

of porous silicon. After etching, the porous silicon was rinsed with methanol to remove any residual HF. Wire leads were soldered to the 2 mm square bond pads to enable ignition via Joule heating. Figure 2.4 shows a coupon consisting of 4 individual 2 mm diameter devices.

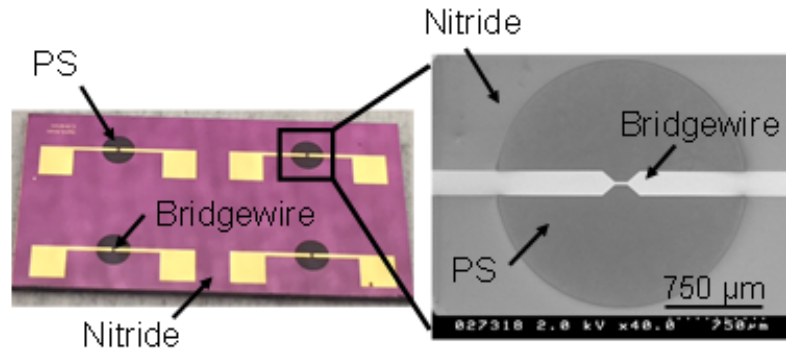


Figure 2.4: (Left) Single diced coupon consisting of four individual 2 mm diameter porous silicon devices (dark circular regions). (Right) A scanning electron micrograph (SEM) of an individual device showing a close-up of the center of the bridgewire.

All porous silicon devices were made energetic by infusing the pores with 3.2 moles/L of sodium perchlorate dissolved in methanol. The dispensed volume was controlled using a micro-pipette, and oxidizer was allowed to dry for 30 minutes before devices were ignited. Based on energy-dispersive x-ray spectroscopy (EDX), it is believed that the oxidizer penetrates to the bottom of the porous silicon layer [57]. However, a significant amount typically remains on the surface, which does not likely participate in the reaction, but which does complicate a straightforward determination of oxidizer mass. Based on findings reported in [57], the amount of residual sodium perchlorate left in the pores after methanol evaporation corresponds to careful gravimetric measurements of

sodium perchlorate in the pores, suggesting that a straightforward calculation involving pore volume and oxidizer concentration in methanol may be used to predict fuel-oxidizer equivalence ratios in the resulting composite. Based on porosities reported in this work, the fuel-oxidizer equivalence ratios ranged from 5 to 35, with the lowest ratio corresponding to the highest initial porous silicon porosity.

### 2.3 Etch Repeatability

Initial attempts to evaluate the thrust performance of porous silicon devices fabricated by the galvanic etch resulted in variability in the measured force output as a function of time. Devices were etched using silicon wafers within the range of 5 to  $8 \Omega \cdot \text{cm}$ . Etch depths were calibrated based on the wafer resistivity and etch time. Test coupons were first etched, and the porous silicon was then dissolved in a solution of sodium hydroxide (2.5 g) and water (50 mL) to verify etch depth with a stylus profilometer.

While etch depth was nominally constant, the author attempted to further investigate the source of variability in thrust performance by first analyzing the structure of the porous silicon produced by the etch process. To do this, the author performed a series of volumetric analysis measurements on the porous silicon based on Brunauer-Emmett-Teller method [59] using a Micromeritics TriStar II Surface Area and Porosity tool. The tool measures physical adsorption of gas molecules inside particles. To ensure the accuracy of the analysis technique, there

must be approximately 2-3 mg of porous silicon available to analyze in the sample tube. However, each coupon had a much lower mass of porous silicon. To increase mass, three larger silicon coupons consisting of 25 individual 2 mm porous silicon devices etched to a nominal depth of 30  $\mu\text{m}$  were used instead. Each 2 mm diameter porous silicon device was approximately 100  $\mu\text{g}$  in mass. The coupons were etched separately in a hydrofluoric acid resistant beaker, and were positioned at various locations inside the beaker during the etch process. The etch solution was reused to etch all three coupons, and the etchant was stirred at 900 RPM. All coupons tested were diced from the same larger 4 inch silicon wafer to ensure constant resistivity. A 3:1 hydrofluoric acid to ethanol etch was performed for four minutes on each of the coupons. Upon completion of the etch, each coupon was cleaved into smaller pieces and placed inside sample tubes to undergo a 1 hour de-gas process to dry out residual moisture in the pores. The sample tubes were then loaded into the TriStar II and analysis performed on the pores. Table 2.1 shows the results of the volumetric analysis, which indicate that while the etch depth was relatively constant, there was variability in the surface area, pore volume, and porosity.

Table 2.1: Volumetric analysis measurements performed on three separate silicon coupons, each consisting of 25 individual 2 mm porous silicon devices. Each coupon was placed at a different location in the etch beaker during the etch.

Conc. (HF:EtOH)	Depth ( $\mu\text{m}$ )	Surf. Area ( $\text{m}^2/\text{g}$ )	Volume ( $\text{cm}^3$ )	Porosity (%)
3:1	23-30	721.7	0.6768	61.2
3:1	21-23	848.2	0.8079	65.3
3:1	21-24	591.9	0.6384	59.8

Another set of three separate etches were performed, using silicon of identical resistivity. The etchant again consisted of 150 mL HF, 50 mL EtOH, and 4.8 mL H<sub>2</sub>O<sub>2</sub>. New etch solution was mixed up before each etch, and the etch time was held constant at 4 minutes. The silicon coupons were held in place using a clamp, and a plastic holder that was notched out to accommodate the clamp. The fixture and clamp, shown in Figure 2.5, were designed to keep the coupon submerged in the same relative location from one etch to the next. The third etch was slightly mis-positioned in the etch beaker. Table 2.2 shows a summary of the porous silicon structural properties when the position of the coupon was controlled inside the etch bath and the etch bath was replaced before each etch. It was believed that the hydrogen peroxide was depleted during the etch therefore needing to be replaced.

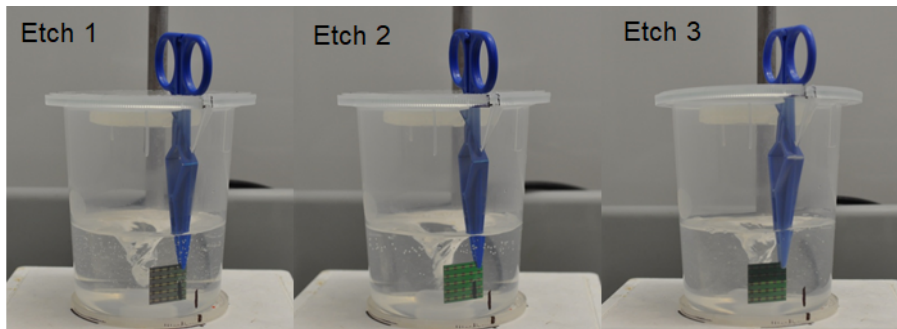


Figure 2.5: Three separate etches performed in HF resistant beakers, where the silicon coupon was suspended at approximately the same location in the beaker using a blue clip, held in place with a notched plastic fixture

Table 2.2: Volumetric analysis measurements performed on three separate silicon coupons, each consisting of 25 individual 2 mm porous silicon devices. Each coupon was placed at the same relative location in the beaker.

Conc.	Depth ( $\mu\text{m}$ )	Surf. Area ( $\text{m}^2/\text{g}$ )	Volume ( $\text{cm}^3$ )	Porosity (%)
3:1	31-34	968.6	1.2	74.0
3:1	31-34	971.1	1.2	73.0
3:1	31-34	947.4	1.2	73.0

The author concluded that in order to maintain consistent pore characteristics between etches, the location of the silicon coupon in the etch bath needed to be held constant and new etchant was needed for each etch. After conducting more than 12 experiments, each taking approximately 45 minutes, including etching, mounting to the force sensor, and oxidizing, the author noticed that some of the porous silicon devices were not completely burning during the reaction as shown in Figure 2.6. Three separate coupons were etched identically using a 3:1 mixture of hydrofluoric acid to ethanol, and 4.8 mL of hydrogen peroxide. The location of the coupons was controlled and the etch time was held constant at 4 minutes. Again the partial burning was observed. It was unclear whether this was associated with oxidizer filling, or local variations in the porous silicon structure that were preventing oxidizer from effectively penetrating the pores. Force measurements were performed and reported in Table 2.3

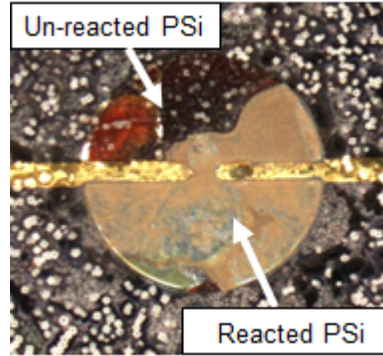


Figure 2.6: Region of un-reacted porous silicon. White crystalline structures scattered across the chip are residual oxidizer crystals.

Table 2.3: Summary of force and impulse measurements taken from three partially burned porous silicon devices.

Force Output (mN)	Reaction Duration ( $\mu\text{s}$ )	Impulse ( $\mu\text{N} \cdot \text{s}$ )
400	780	300
120	400	48
180	650	117

The source of the partial burn was thought to be attributed to variations in the electrical properties of the Pt electrode sputter deposited on the backside of the silicon. It was shown in [10] that annealing the Pt after deposition produced a platinum silicide that enhances electrical connectivity to the substrate resulting in more stable porous silicon layers when produced by the galvanic etch. Therefore the author performed force measurements on a set of five porous silicon devices where the Pt electrode was not annealed, and then tested a set of four porous silicon devices that had an annealed Pt electrode. All devices were derived from a p-type, boron doped silicon wafer with a resistivity of  $6 - 9 \Omega \cdot \text{cm}$ . The non-annealed devices were etched in a 3:1 solution of HF to EtOH with 1.2 %  $\text{H}_2\text{O}_2$  by volume. The concentration of  $\text{H}_2\text{O}_2$  was reduced to slow down the etch and

stabilize the porous silicon. The etch depth varied from 28 - 33  $\mu\text{m}$  across four devices on a silicon coupon. The measured porosity was 71 %. Figure 2.7 shows force output as a function of time varied from approximately 100 mN to 700 mN over five different tests.

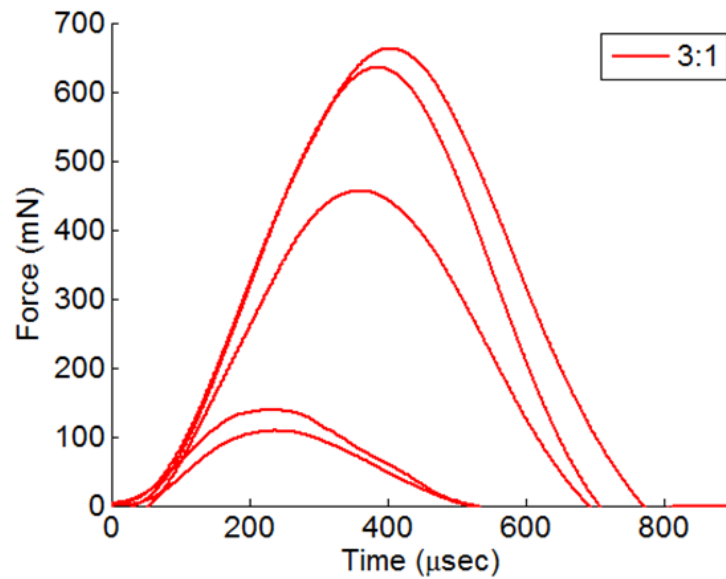


Figure 2.7: Force vs time generated for five un-annealed porous silicon devices.

The four annealed devices were etched for 2 min and 22 seconds to achieve a target depth of 30  $\mu\text{m}$ . The actual measured depth was 26.5 to 27.8  $\mu\text{m}$ . The Pt electrode was annealed for 2 minutes at 350°C in nitrogen. The decision to anneal at 350°C for 2 minutes was based on the process discussed in [10]. Figure 2.8 shows the force output as a function of time for porous silicon devices fabricated with annealed Pt electrodes. The peak force varied from 488 mN to 619 mN. The porosity of porous silicon was 76.5 %. The increased repeatability in the force output was further verification that all porous silicon devices fabricated for this study needed to have an anneal step performed on the Pt electrode prior to etch-

ing. Because the anneal was performed at 350°C, the anneal was done before any lithography to avoid inadvertently hard baking photoresist to the silicon wafer.

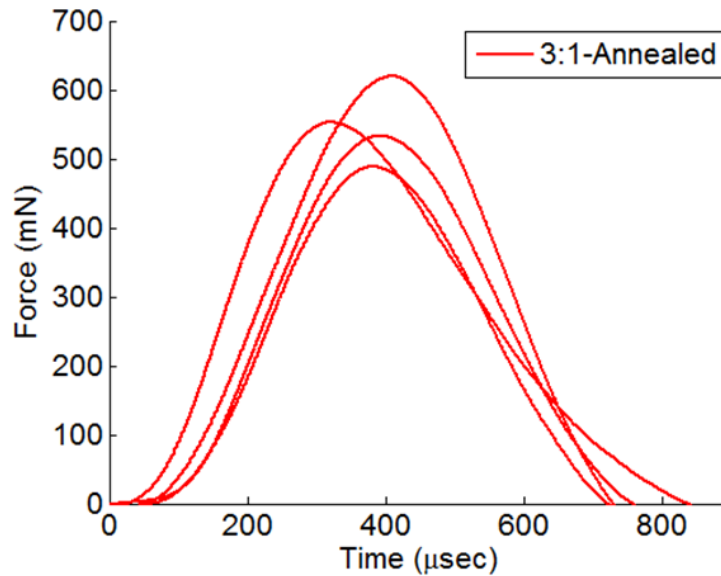


Figure 2.8: Force vs time generated for four annealed porous silicon devices.

## 2.4 Force Measurement Repeatability

To evaluate dynamic thrust generated by the energetic porous silicon, the author used an experimental set-up shown in Figure 2.9. The setup consisted of a Kistler 9215A force sensor, which is a high sensitivity piezoelectric sensor manufactured with an external thread and a sealed ceramic-insulated connect plug [60]. The sensor range is 1 mN to 200 N with a natural frequency of 50 kHz. The sensor was threaded into a block of aluminum to hold it in place and to minimize vibrations. The top of the sensor had a threaded hole where a mounting cap, known as an M2 tap, was threaded. Figure 2.10 shows the Kistler 9215A sensor and the smaller M2 tap that threads into the top of the sensor. Deflections imparted onto

the M2 tap were measured by a Kistler Type 5010 Dual Mode Amplifier that converted the charge signal generated by the Kistler 9215A into a voltage signal that was measured on an oscilloscope.

The voltage output was converted to force based on the charge amplifier measurement scale setting of 0.1 N/V. The sensor was calibrated by placing three different known calibration masses (1.5 g, 6.5 g, and 40 g) onto the sensor, which produced forces measuring 15 mN, 64 mN, and 397 mN respectively. These were representative of the target values measured in this study. The measured force was within 1 % of the reference force for each case. Although these were static measurements, they provided confirmation that the sensor and charge amplifier were calibrated within manufacturer specifications. Output waveforms were filtered using a second-order Savitzky-Golay filter with a frame size of 301. The total sample size of each force vs. time plot was approximately 5000 with a sample rate of 2.5 Mega samples per second.

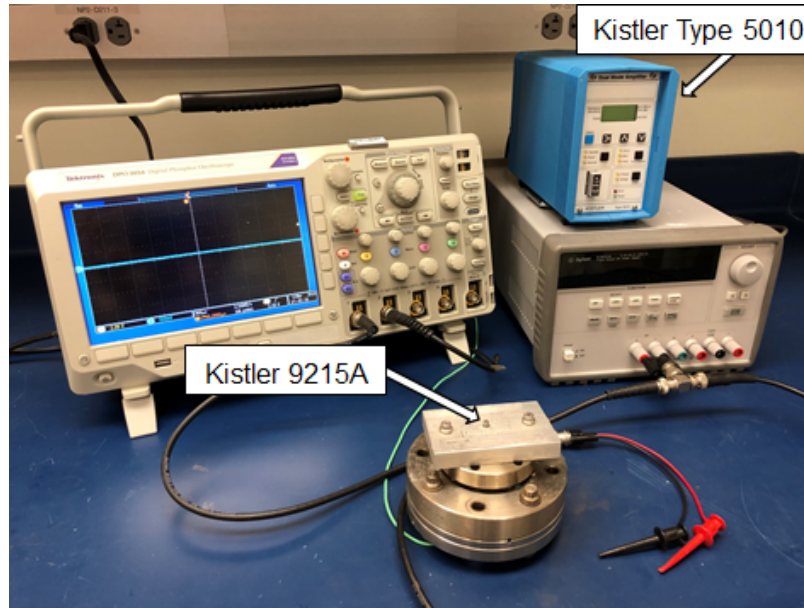


Figure 2.9: Experimental set-up used to evaluate force generated by energetic porous silicon. The Kistler 5010 converts charge signal from the piezo in the Kistler 9215A force sensor into voltage waveform.

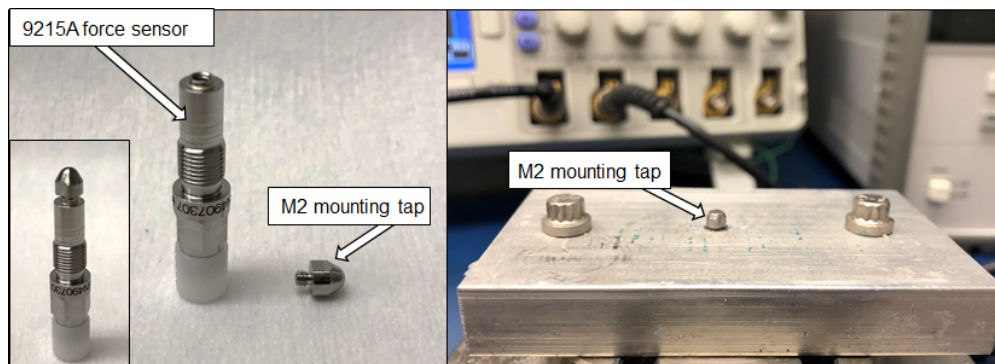


Figure 2.10: Image of the Kistler 9215A sensor and the M2 tap used to interface with the sensor. The porous silicon device was mounted on the M2 tap.

Individual 2 mm diameter porous silicon devices were cleaved from a coupon and attached to a M2 tap shown in Figure 2.11 using a piece of wax because of the destructive nature of the test. The piece of wax, approximately  $1 \text{ mm}^3$ , was melted with a soldering iron tip before the porous silicon chip was attached. To ensure that the thrust axis was aligned with the sensing axis, the author visibly

confirmed that the porous silicon device was level and mounted perpendicular to the sensor. For each test, the porous silicon devices were fabricated and infused with oxidizer using the same procedure and the samples were mounted as similarly as possible on the sensor head. The oxidizer was added and allowed to dry in a dry room, with relative humidity below 1 % because of the hydroscopic nature of sodium perchlorate. Force sensor measurements were carried out in the same dry room.

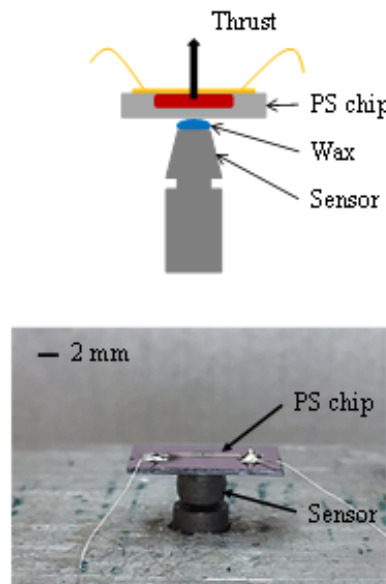


Figure 2.11: Experimental set-up (top: schematic, bottom: photo of actual test setup) used to measure force produced by porous silicon device. Devices are not drawn to scale.

Initial attempts were made to modify the M2 tap that came with the Kistler 9215A sensor because the author was concerned about not having sufficient surface area on the M2 tap to properly attach the porous silicon chip such that it was level with the sensor. The first modification involved epoxying the tap to a larger

aluminum block shown in the Figure 2.12, and then screwing the tap into the Kistler 9215A sensor. A set of four porous silicon devices were etched to evaluate the mounting setup. Porous silicon was etched for 4 minutes in a 3:1 mixture of HF to EtOH, and 0.96 mL of hydrogen peroxide. Two drops of 3  $\mu$ L of 3.2 M sodium perchlorate were dispensed onto each porous silicon device, and allowed to dry for 30 minutes. The resulting etch depth was 27 to 28  $\mu$ m measured across four devices. Figure 2.13 shows the force measured using the modified M2 tap with the large mounting block. There was significant bouncing of the sensor as the voltage signal appeared to fall below zero before trying to recover. The average peak force was 461.3 mN with a standard deviation of 243.3 mN. This may have been the result of having an additional mass attached to the M2 tap. The mass of the modified M2 tap was 3.0 g, as opposed to the mass of the M2 cap by itself, which was 0.3 g.

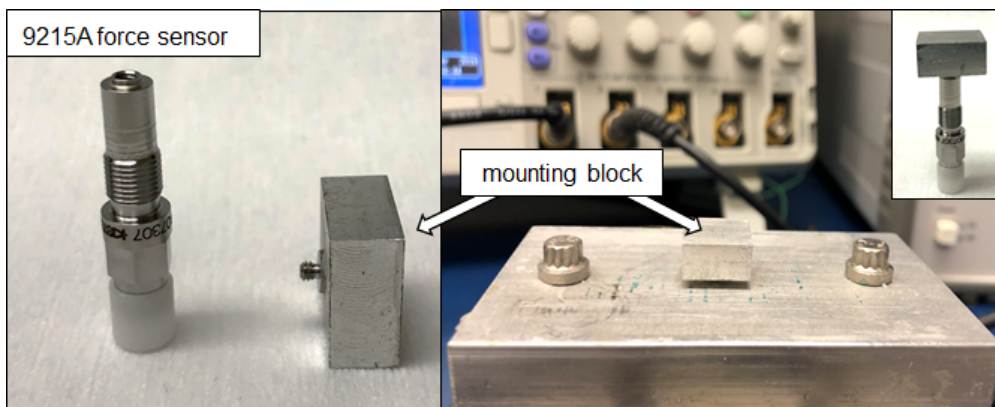


Figure 2.12: Aluminum block was attached to the M2 tap to provide more surface area for mounting the porous silicon device.

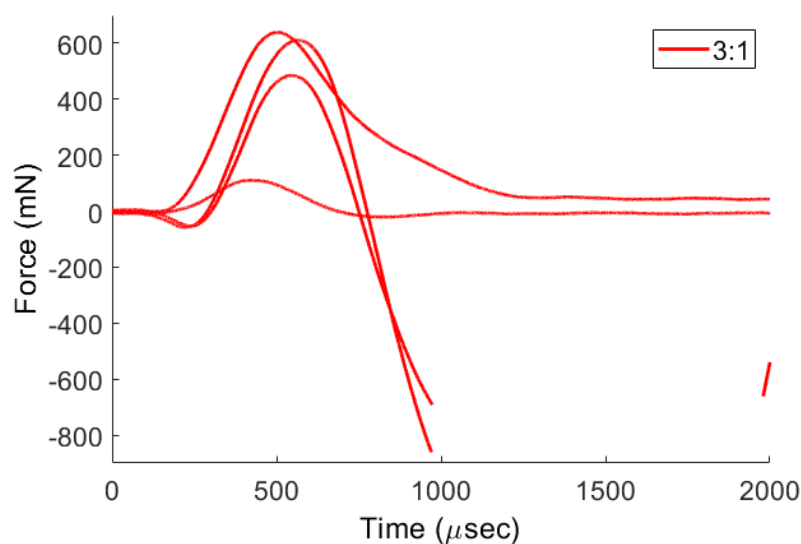


Figure 2.13: Force output generated when porous silicon devices were attached using the modified M2 tap with aluminum block

The author repeated the experiments using the M2 tap provided by Kistler to mount the porous silicon devices. The author flattened the tip of the M2 tap using a Dremel tool to create a relatively flat surface to attach the porous silicon chip. Careful attention was given to make sure that the porous silicon device was perpendicular with respect to the sensor. Porous silicon was etched using the same recipe, with comparable etch depths ranging from 22 to 23  $\mu\text{m}$ . Again, 6  $\mu\text{L}$  of 3.2 M sodium perchlorate was applied and allowed to dry for 30 minutes. Figure 2.14 shows the force generated when porous silicon devices were mounted onto this M2 tap. The average peak force was 82.5 mN with a standard deviation of 2.1 mN. Therefore all subsequent experiments were performed with the M2 tap with the slightly flattened tip.

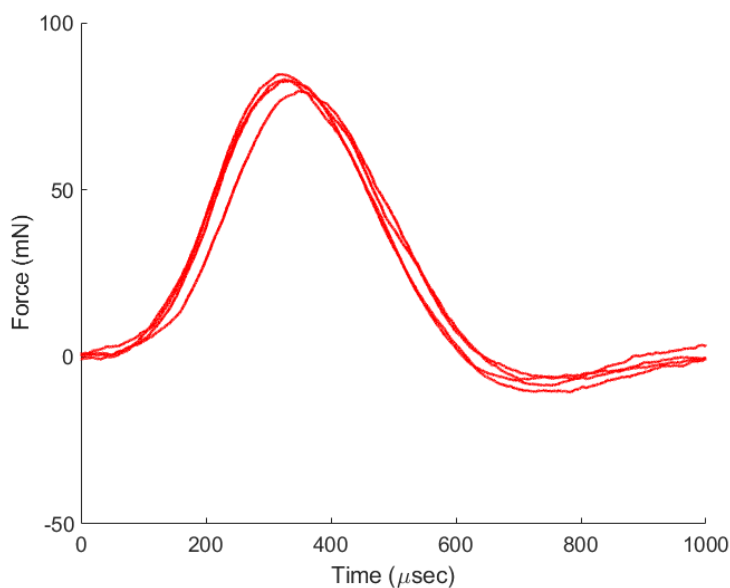


Figure 2.14: Force output generated when porous silicon devices were attached using the original M2 tap

## 2.5 Oxidizer Loading

A Cole-Parmer EX Plus micro-pipette was used to manually dispense sodium perchlorate oxidizer onto the porous silicon. Early experiments were done by applying approximately 6  $\mu\text{L}$  of oxidizer, resulting in residual oxidizer covering the surface of the porous silicon and some of the surrounding silicon nitride mask. It was unclear whether the excess oxidizer participated in the reaction as ejected hot porous silicon particles burned in air. To address this concern, the porous silicon devices were made energetic by oxidizing one device with 1  $\mu\text{L}$  of 3.2 M dissolved in methanol, and another device with 6  $\mu\text{L}$  of the same oxidizer. The Cole Parmer EX Plus micro-pipette was used to apply the oxidizer and the oxidizer was allowed to dry for 30 minutes. Still images of high speed video shown

in Figure 2.15, captured with a Photron FastCAM SA5, show qualitative similarities between two porous silicon devices that were etched to a nominal 40  $\mu\text{m}$  depth. The 6  $\mu\text{L}$  of oxidizer was applied as two separate drops of 3  $\mu\text{L}$  of  $\text{NaClO}_4$ . It was determined that these devices were structurally sound, and did not have subsurface cracks prior to application of the oxidizer.

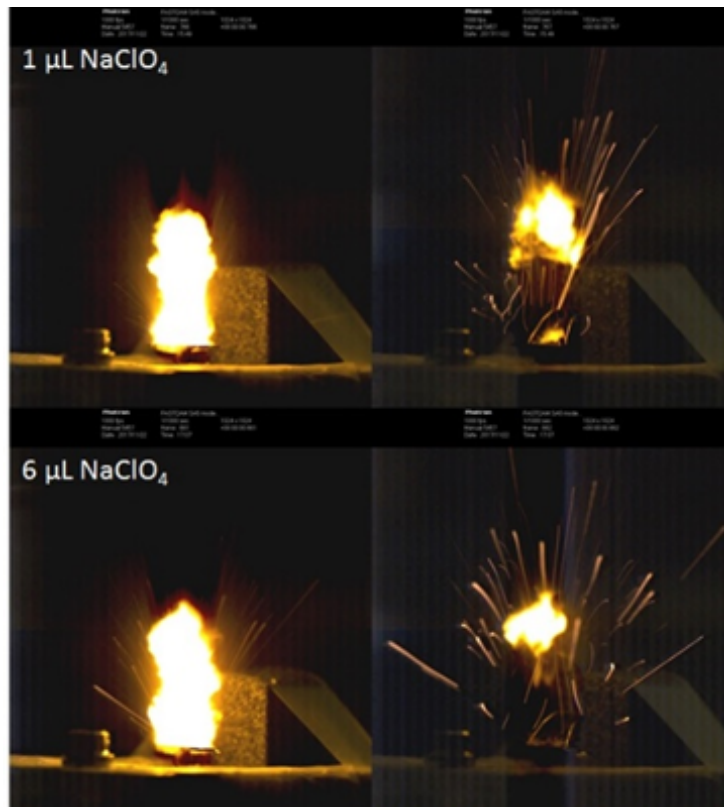


Figure 2.15: (top) High speed video frame capture showing flame generated by a single 2 mm diameter porous silicon device oxidized with 1  $\mu\text{L}$  of sodium perchlorate (bottom) Similar device oxidized with 6  $\mu\text{L}$  of sodium perchlorate.

The force versus time curves were measured for both devices, both generating an approximate peak force of 800 mN. In both experiments, the porous silicon chip cracked upon ignition, and produced an observably louder audible signature in comparison to devices etched below 20  $\mu\text{m}$ . The double peak formation observed

on the sensor output had been previously seen when the output of the porous silicon was approximately 1 N or greater, and was the result of exciting multiple resonant frequencies in the piezoelectric sensor [61]. These results indicated that the reaction output appeared to be independent of the oxidizer loading. The 1  $\mu\text{L}$  of oxidizer used in the above experiments was localized to the porous silicon, whereas the 6  $\mu\text{L}$  covered both the porous silicon region and the silicon chip. This led the author to believe that the source of non-uniformity even across a single coupon was due to the electrical properties of the platinum electrode used to drive the galvanic etch process as previously discussed.

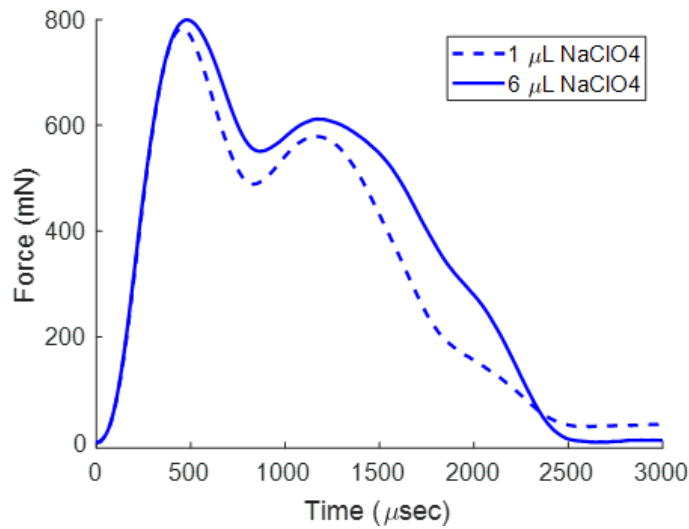


Figure 2.16: Force versus time curves comparing oxidizer loading.

Table 2.4: Summary of peak force, and impulse based on different oxidizer loading amounts.

Oxidizer Amount	Peak Force (mN)	Impulse ( $\mu\text{N} \cdot \text{s}$ )
1 $\mu\text{L}$	799.6	952.6
6 $\mu\text{L}$	782.7	1100.0

## 2.6 Conclusion

Prior to studying energetic porous silicon as a solid propellant micro-thruster, the author attempted to address potential issues that could affect repeatability. Although every possible attempt was made to control the position of the wafer in the etch bath, and nitrogen annealing was performed on all devices fabricated for this study, there was still evidence of lack of repeatability in the force and impulse measurements reported. Some of these issues were believed to be associated with the quality of the Pt backside electrode. Early studies that were published in [62] demonstrated very good repeatability in the measured force output across similarly fabricated porous silicon devices. The Pt electrodes used for these wafers were deposited at the U.S. Army Research Lab using a Varian etch tool. After the tool was decommissioned, the Pt deposition was outsourced to an external vendor. It was unclear whether this contributed to the reduced quality of the etched porous silicon.

Although attempts were made to measure the wafer resistivity after the Pt deposition, limitations to the 4 point probe measurement tool prevented the author from determining variation in electrical contact across the entire wafer. Further investigation can be performed, including Ohmic contact measurements of the Pt after deposition. While careful study of these variabilities should be investigated in future work, the results gathered in this work still allowed the author to observe and measure clear trends in the performance of thrust and impulse as a result of varying a number of porous silicon material characteristics.

## Chapter 3

### Effect of Morphology on Propulsion Performance

#### 3.1 Introduction

In this chapter, the author performed an in-depth characterization of the effects of porous silicon morphology on the material's performance as a propellant, and the material in this chapter was previously published in *Journal of Micromechanics and Microengineering* [62]. Thrust and impulse are important metrics for propulsion, but previous studies on reaction propagation [57, 63] have not characterized energetic porous silicon in terms of its ability to generate thrust and impulse. This study focuses on small active areas ( $3 \text{ mm}^2$ ) with slower burn rates in comparison to previous work that resulted in fractured chips [9]. This work builds on research published by the author in [61] that showed initial performance characterization for a single porous silicon micro-thruster fabricated with fixed etch parameters. In contrast to [61], the current study examines the effects of changing porous silicon etch parameters on porosity and thrust performance.

#### 3.2 Experimental Methods

To investigate thrust and impulse, the author first varied porosity by changing the HF to EtOH ratio of the etch solution from 3:1, 12:1, and 20:1, while hold-

ing the depth of each layer to a target of 30  $\mu\text{m}$ . In addition to looking at the effect of electrolyte concentration, the electrolyte ratio was held constant at 3:1 and the depth of the porous silicon layer was varied from approximately 10  $\mu\text{m}$  to 40  $\mu\text{m}$ . Finally, wafer resistivity was varied while holding both the electrolyte concentration constant at 3:1 and the target etch depth at 30  $\mu\text{m}$ . The author used wafers that measured 0.016  $\Omega\text{-cm}$ , 3.6  $\Omega\text{-cm}$ , and 3  $\text{k}\Omega\text{-cm}$  to fabricate porous silicon. The wafer resistivity was determined by the wafer vendor, Rogue Valley Microdevices, and was verified in the cleanroom using a four-point probe measurement system. To ensure that repeatable porous silicon was produced from one etch to another it was critical to control the placement of the coupon in the etch bath, as well as use a fresh mixture of etch solution for each etch. The author was able to reduce the variability in porosity by less than 2 % by following this procedure, ensuring that the morphology of the porous silicon remained consistent from etch to etch.

### 3.2.1 Gravimetric Determination of Porous Silicon Porosity

Gravimetric analysis to measure porosity was done on individual coupons consisting of four porous silicon devices using a Mettler Toledo XP26 scale with a readability precision of 1  $\mu\text{g}$ . A coupon was used to measure porosity gravimetrically because there was sufficient etched material to more easily differentiate changes in mass. The actual precision of the scale was determined to be 10  $\mu\text{g}$ , which was the standard deviation of 50 measurements on the same coupon with

an average measured mass of 318.49 mg. The total porous silicon mass for an etch depth of 30  $\mu\text{m}$  was greater than 240  $\mu\text{g}$ , so mass differences determined using these methods were assumed to be reasonably accurate. Each porosity value in this study was measured on three coupons etched under the same conditions, except for the variation in etch depth, for which only a single coupon was measured at each condition.

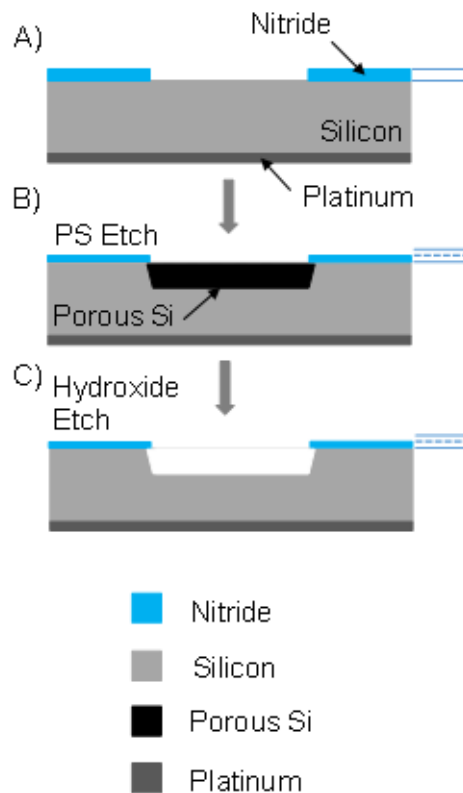


Figure 3.1: Figure showing the individual steps taken to evaluate porosity gravimetrically, including accounting for change in mass due to nitride and porous silicon etching.

Figure 3.1 shows the steps used to measure porosity. First, the mass of the coupon ( $m_1$ ) in Figure 3.1 (A) was measured before porous silicon etching was performed and before the edges of the coupon were coated with silicone. Be-

cause the surface area ratio of exposed Si to backside Pt affects the etch rate, the edges of the silicon chip were coated with silicone (Duraseal 1533) to restrict etching to the intended regions of exposed silicon. The two-part silicone was mixed in a weighing dish, and then manually painted onto the edges of the coupon, and allowed to cure for 2 hours. Residual silicone was removed from the backside to ensure that the Pt contact was fully exposed during the etch. After etching, the silicone was peeled from the edges of the coupon, and the mass of the coupon was measured ( $m_2$ ) in Figure 3.1 (B). This mass represented the mass of the coupon immediately following the etch. Finally, porous silicon was removed from the silicon substrate using aqueous sodium hydroxide (Figure 3.1 (C)), by dissolving 2.5 g of sodium hydroxide flakes in 50 mL of deionized water. Upon removal of the porous silicon, the final mass of the silicon coupon was measured ( $m_3$ ).

To determine porosity accurately, it was important to also account for changes in the mass of the nitride etch mask on top of the coupon, as well as other changes to the sample mass that may occur such as microscopic regions of porous silicon etching through small pinholes in the backside Pt layer ( $m_4$ ). To measure these additional mass changes, four identical blank coupons each with nitride on the frontside, Pt on the backside, and silicone on the edges were placed in a 3:1 HF:EtOH etch bath for times ranging from 1 to 8 minutes. Although no significant amount of porous silicon was created or etched during this process, a resulting linear mass loss rate of 432  $\mu\text{g}/\text{min}$  was determined, and this value was used to interpolate an appropriate value for  $m_4$  for each subsequent experimental case involving the 3:1 etch condition. For the 12:1 and 20:1 etch conditions, a sin-

gle blank coupon was etched at each concentration for the same etch times used for the non-blank porous silicon samples, resulting in  $m_4$  values of 1.02 mg and 1.09 mg for the 12:1 and 20:1 conditions, respectively. These single data points corresponded to mass loss rates of 428 and 504  $\mu\text{g}/\text{min}$ , for the 12:1 and 20:1 conditions.

Equation 3.1 was used to calculate porosity (P) based on the masses that were measured. The numerator represents the mass of the bulk silicon removed as a result of the porous silicon etch, while the denominator represents the remaining mass after bulk silicon and remaining porous silicon was removed, allowing the author to determine the actual mass of porous silicon formed during the etch.

$$P = \frac{m_1 - (m_2 + m_4)}{m_1 - (m_3 + m_4)} \quad (3.1)$$

### 3.2.2 Varying Concentration and Etch Depth of Porous Silicon Etch

The porosity of porous silicon was varied by first changing the ratio of hydrofluoric acid to ethanol used in the etch solution. The ratios used were a 3:1, 12:1, and 20:1 mixture of HF to ethanol. While varying the concentration of the etchant, etch time was controlled to ensure that the depth of the porous silicon was close to a target depth of 30  $\mu\text{m}$ . Layer thickness was verified by destructively etching away the porous silicon and measuring the step height with a stylus profilometer (Tencor P15) on two samples, with the average depth reported later in this

chapter. A total of four devices were tested for thrust at each of the three concentrations.

In addition to looking at the effect of varying etch ratio, the porous silicon layer target thickness was varied from 10  $\mu\text{m}$  to 40  $\mu\text{m}$  in target increments of 10  $\mu\text{m}$ . The ratio of hydrofluoric acid to ethanol was held constant at 3:1, while the depth was varied by varying etch time. Actual etch depths were reported in the results as averages of two samples. For the force measurements, a total of four devices were tested for each etch depth, while a single coupon was tested at each condition for porosity.

### 3.2.3 Varying Resistivity of Silicon Wafer

The porosity was also varied by changing the resistivity of wafers used to etch porous silicon. Wafers of three different resistivity values (0.016  $\Omega\text{-cm}$ , 3.6  $\Omega\text{-cm}$ , and 3  $\text{k}\Omega\text{-cm}$ ) were used to fabricate the porous silicon. For these experiments, the etch depth was again controlled to a target thickness of 30  $\mu\text{m}$ . Actual etch depths were again measured and reported as the average of two samples. A 3:1 concentration of hydrofluoric acid to ethanol was used for each of these experiments. A total of four force measurements and three separate porosity measurements were taken for each resistivity.

### 3.2.4 Calculating Impulse and Specific Impulse

Impulse was calculated by integrating filtered thrust over time using trapezoidal integration in MATLAB. The specific impulse, calculated in Equation 3.2, is a function of gravity ( $g$ ) acting on the system, the total impulse ( $I_m$ ), and the mass of the propellant ( $m_p$ ), which includes both the mass of the porous silicon fuel and the sodium perchlorate oxidizer.

$$I_{sp} = \frac{I_m}{m_p \cdot g} \quad (3.2)$$

The approximate mass of the porous silicon can be calculated based on the volume of a porous silicon device, density of silicon, and fraction of silicon remaining. As discussed previously, the amount of oxidizer in the pores was equivalent to filling the pores with the oxidizer/solvent solution and then removing the solvent. Therefore, the mass of oxidizer was calculated based on total pore volume, solvent concentration, and molar mass of sodium perchlorate. As an example, a 2 mm diameter, 30  $\mu\text{m}$  deep porous silicon device with 72.9 % porosity had a porous silicon mass of 60  $\mu\text{g}$  and a calculated oxidizer mass of 23  $\mu\text{g}$ , for a total propellant mass of 83  $\mu\text{g}$ .

### 3.2.5 Measuring Impulse with Pendulum

A pendulum experiment was also used to measure impulse generated by the porous silicon micro-thruster and validate force sensor measurements. The experiment was performed for a device etched using a 3:1 electrolyte concentration

with a 3.6  $\Omega$ -cm wafer. The device measured nominally 30  $\mu\text{m}$  in depth. The mass of the chip, which was composed of a single porous silicon device, was 0.112 g. A rigid wire (30 AWG Kynar Insulated Wire-Wrap Wire) measuring 0.114 m in length was used for the pendulum arm as well as for igniting the device. A protractor was mounted behind the swinging pendulum arm at the pivot point. The displacement of the pendulum arm was observed visually using a Photron Fast-CAM SA5 high speed camera at 2000 frames per second. All tests were carried out in a dry box filled with nitrogen with a relative humidity of  $< 1\%$ .

Impulse was calculated from the pendulum's oscillatory behavior described in Equation 3.3 for small angular displacement  $\theta$ , where  $\omega_0$  is the natural frequency,  $\dot{\theta}$  is the angular velocity, and  $\zeta$  is the damping ratio. In a system where damping is present, the damping frequency  $\omega_1$  can be represented as a function of the natural frequency  $\omega_0$  shown in Equation 3.4.

$$\ddot{\theta} + 2\zeta\omega_0\dot{\theta} + \omega_0^2\theta = 0 \quad (3.3)$$

$$\omega_1 = \omega_0\sqrt{1 - \zeta^2} \quad (3.4)$$

The damping ratio was determined using high speed video to measure the pendulum's angular displacement as a function of time, and fitting the measured maximum displacement of each oscillation to an exponential curve to determine oscillation decay. The solution to Equation 3.3 with an initial angular position of

zero is:

$$\theta(t) = Ae^{-\zeta\omega_0 t} \sin(\sqrt{1 - \zeta^2}\omega_0 t) \quad (3.5)$$

The second initial condition was that at time  $t=0$ , the angular velocity was equal to an initial angular velocity experienced by the pendulum system. Assuming that thrust was delivered instantaneously at the start of pendulum motion, and recognizing that the integration of Newtons Second Law in terms of torque and angular acceleration yielded the integration of a force applied at a distance,  $L$ , from the pendulum pivot point, the initial angular velocity is:

$$\dot{\theta}(0) = \frac{LI_m}{I} \quad (3.6)$$

where  $I_m$  is the impulse delivered by the thruster and  $I$  is the moment of inertia of the system. Because the mass of the wire is non-negligible in comparison to the mass of the porous silicon, the system cannot be evaluated as a point-mass model. Instead, inertia is calculated as a point mass (the micro-thruster chip) at the end of a rod of length  $L$  with non-zero mass (the wire). This equation was used to solve for the coefficient  $A$  in Equation 3.5. The angular displacement is expressed in terms of the impulse as shown below.

$$\theta(t) = \frac{LI_m}{\omega_1 I} e^{-\zeta\omega_0 t} \sin(\sqrt{1 - \zeta^2}\omega_0 t) \quad (3.7)$$

To solve for the impulse, the time at which the oscillating devices velocity was equal to zero, or the point in time at which the device reached maximum

displacement, was measured. Both time at maximum displacement and the measured maximum angular displacement were substituted into Equation 3.7, and the impulse was calculated by re-arranging the equation.

In addition to using this single maximum angle measurement to measure impulse, the author used high speed video to track the displacement of the porous silicon micro-thruster over several periods and applied these measurements directly to the general solution in Equation 3.3. The angular displacement versus time was plotted and the period and frequency of the oscillations were calculated directly. A least squares fit was performed on the data to determine the coefficient  $A$  and  $\zeta$  in Equation 3.5. Given the coefficients  $A$  and  $\zeta$ , the author was able to solve for impulse based on Equations 3.6 and 3.7.

### 3.3 Results

#### 3.3.1 Concentration of Etch Solution

Table 3.1 shows the measured gravimetric porosity and resulting equivalence ratio for each of the three concentrations. The porosity measurements showed that for 12:1 and 20:1 etch concentrations, the mean porosities were 31.7 % and 30.0 % respectively, whereas the mean porosity for the 3:1 concentration was a much higher 72.9 %. Filtered force measurements are shown in Figure 3.2 for four devices and Table 3.1 lists the mean and standard deviation of peak force, impulse, and specific impulse for each concentration. The 3:1 electrolyte concentration generated the largest mean peak thrust of 662 mN along with the largest mean

impulse of  $261 \mu\text{N} \cdot \text{s}$ . This large impulse resulted in a specific impulse of 320 s. Of these results, the best performing device had a peak thrust of 674 mN, an impulse of  $271 \mu\text{N} \cdot \text{s}$ , and a specific impulse of 333 s. The devices etched at 12:1 and 20:1 produced similar but lower peak thrusts and impulses. These similarities may be related to the similar porosity of the porous silicon as seen in Table 3.1. Specific impulse was an order of magnitude lower for these concentrations. The significantly higher values at the 3:1 concentration may be due to higher porosity which allowed more oxidizer into the pores and resulted in an equivalence ratio closer to unity. All of the reactions were complete within 1 ms.

Table 3.1: Results for varied electrolyte concentrations. The error is the standard deviation over 4 trials (3 trials for porosity). The equivalence ratio is based on the average porosity.

Conc.	Depth ( $\mu\text{m}$ )	R ( $\Omega\text{-cm}$ )	P (%)	Equiv. Ratio	Peak Thrust (mN)	Imp ( $\mu\text{N} \cdot \text{s}$ )	$I_{sp}$
3:1	29.2	3.6	$72.9 \pm 5.7$	5.57	$662 \pm 11.7$	$261 \pm 18.2$	$320 \pm 22.4$
12:1	28.3	3.6	$31.7 \pm 10.5$	32.3	$48 \pm 2.4$	$15 \pm 1.4$	$20 \pm 1.9$
20:1	29.0	3.6	$30.0 \pm 6.4$	35.0	$57 \pm 7.6$	$16 \pm 2.2$	$21 \pm 2.9$

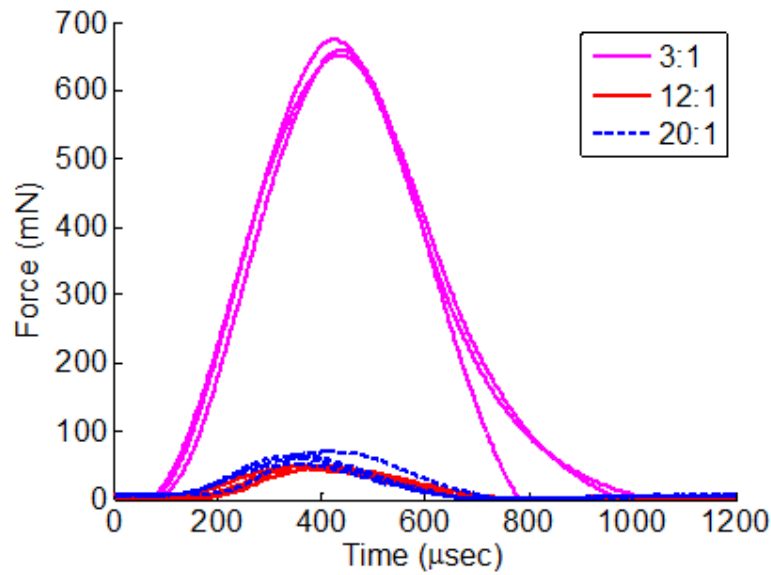


Figure 3.2: Thrust profiles based on the varied electrolyte concentrations.

### 3.3.2 Porosity versus Etch Depth

The porosity of porous silicon devices was varied by changing the etch depth of the porous silicon as discussed above. For each etch depth investigated, four devices were used to measure thrust. Only one porosity measurement was taken for each etch depth. The wafer resistivity ( $3.6 \Omega\text{-cm}$ ) and electrolyte concentration (3:1) used to fabricate these porous silicon devices were held constant. Figure 3.3 shows a plot of etch depth as a function of etch time. The etch depth up to a target depth of  $40 \mu\text{m}$  increases linearly with time.

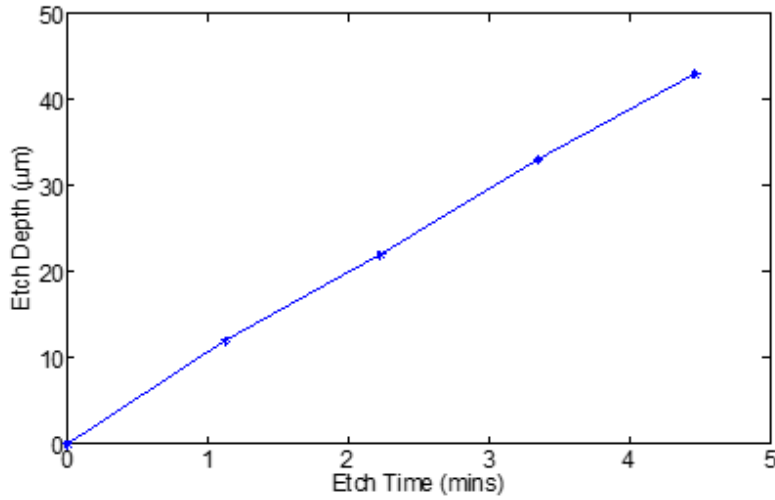


Figure 3.3: Etch depth as a function of etch time.

Table 3.2 lists porosity measurements for the different etch depths. In general, porosity increased as etch depth increased. Changes in porosity as a function of etch depth can be explained by the structure model of porous silicon presented in [64]; the crystalline diameter is reduced over time so more irregularities in the sponge-like matrix arise, increasing the void space in the porous silicon layer.

Table 3.2: Results for varied etch depth. The error is the standard deviation over 4 trials (3 trials for porosity). The equivalence ratio is based on the average porosity.

Conc.	Depth (μm)	R (Ω-cm)	P (%)	Equiv. Ratio	Peak Thrust (mN)	Imp (μN · s)	$I_{sp}$
3:1	12.5	3.6	40	23	29±1.3	8±0.5	24±1.6
3:1	22.5	3.6	64	8.4	50±4.8	14±1.2	20±2.0
3:1	29.2	3.6	72.9	5.7	662±11.7	261±18.2	320±22.4
3:1	40.3	3.6	71	6.1	157±86.7	60±39.5	56±28.9

Thrust was also measured for each etch depth. Figure 3.4 shows a plot of the force versus time for target depths of 10 μm, 20 μm, and 30 μm deep porous silicon devices generated by the Kistler 9215 force sensor and Table 3.2 lists the

peak thrust, impulse, and specific impulse for all etch depths. The 30  $\mu\text{m}$  devices are the same devices seen in the previous section and generate the same 662 mN mean peak thrust, 261  $\mu\text{N} \cdot \text{s}$  mean impulse, and 320 s mean specific impulse. The 10  $\mu\text{m}$  and 20  $\mu\text{m}$  deep samples resulted in significantly lower thrust and impulse, although both increased porosity and equivalence ratios closer to unity may be expected to result in more thrust. Therefore the significant increase at 30  $\mu\text{m}$  may also be due to a critical depth or material mass which partially confines the initial reaction, increasing its internal pressure before allowing the majority of gas to escape at higher velocity.

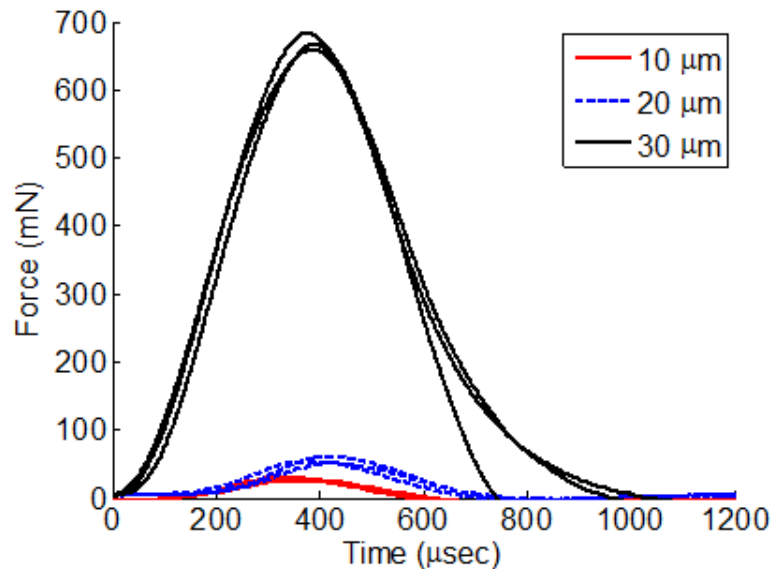


Figure 3.4: Thrust profiles shown as a function of increasing etch depth. Etch depth varied from 10  $\mu\text{m}$  to 30  $\mu\text{m}$  by increments of 10  $\mu\text{m}$ .

Evaluation of the 40  $\mu\text{m}$  deep porous silicon devices resulted in significant variability in force output as shown in Figure 3.5. It was observed that at 40  $\mu\text{m}$ , the porous silicon began to exhibit physical cracks even before a reaction was initi-

ated, which introduced mechanical instability in the layer. These mechanical instabilities have the potential to affect reaction kinetics, and were likely the cause for the variation in thrust performance. Figure 3.6 shows a 30  $\mu\text{m}$  deep porous silicon device with no signs of visible cracking, versus a 40  $\mu\text{m}$  deep device with surface cracks.

To evaluate the observed variation in the output, seven samples were tested at 40  $\mu\text{m}$  etch depth. Despite a porosity and equivalence ratio similar to the 30  $\mu\text{m}$  deep samples, mean peak thrust and impulse numbers were lower at 157 mN and 60  $\mu\text{N} \cdot \text{s}$ , and the devices exhibited very high standard deviations of 86.7 mN and 39.7  $\mu\text{N} \cdot \text{s}$  respectively. These lower propulsion metrics were likely due to the introduction of physical cracks at this depth.

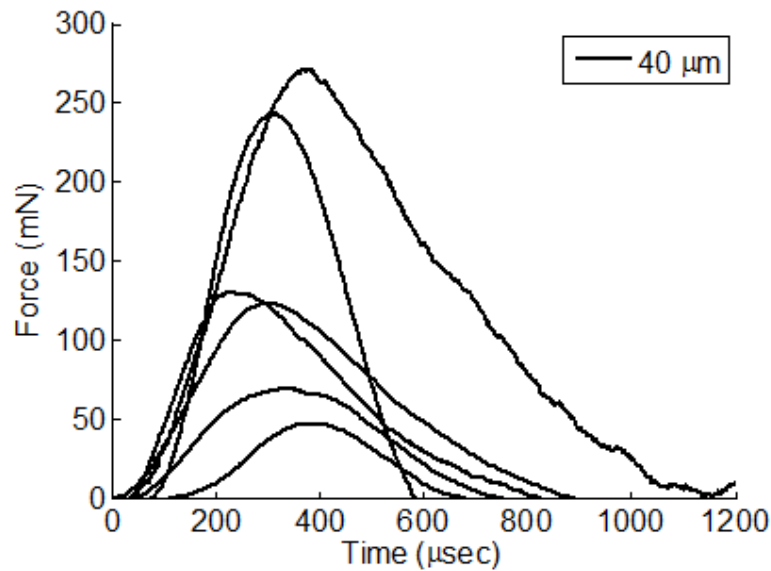


Figure 3.5: Thrust profiles for six porous silicon devices etched 40  $\mu\text{m}$  deep.

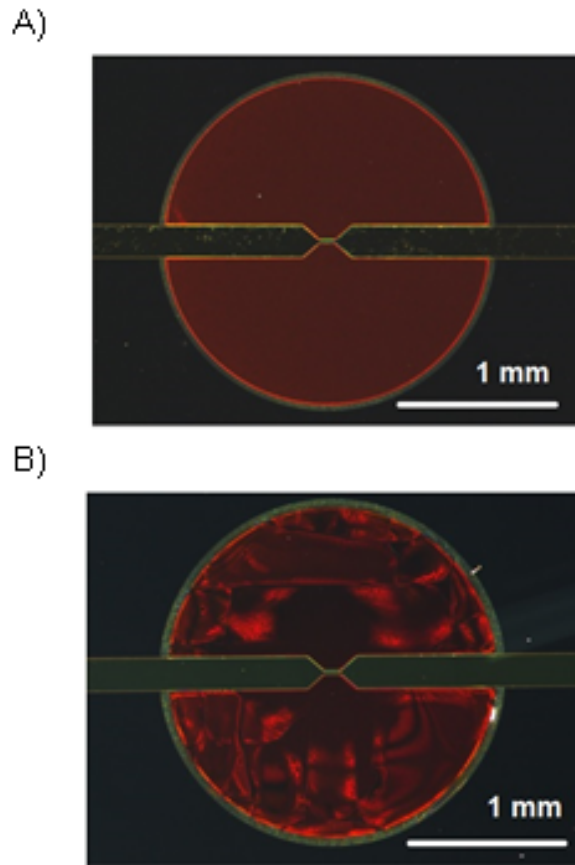


Figure 3.6: (A) 30  $\mu\text{m}$  deep porous silicon sample without surface cracks (B) 40  $\mu\text{m}$  deep porous silicon sample showing surface cracks.

### 3.3.3 Porosity versus Wafer Resistivity

The porosity measurements are summarized in Table 3.3 with 3 measurements used to calculate standard deviation at each resistivity. Porous silicon devices fabricated using 0.016  $\Omega\text{-cm}$  wafers had an average porosity of 45.9 %. Devices fabricated using 3.6  $\Omega\text{-cm}$  resistivity had an average porosity of 72.9 %, while average porosity for devices etched from high resistivity (3  $\text{k}\Omega\text{-cm}$ ) was 37.1 %.

Figure 3.7 shows the thrust performance of porous silicon devices etched

using the three different resistivity wafers and Table 3.3 summarizes the propulsion performance metrics. Devices etched from the 3 k $\Omega$ -cm wafer performed similarly to the 0.016  $\Omega$ -cm wafer, with both generating mean impulses of approximately 20  $\mu\text{N} \cdot \text{s}$  and peak thrusts of 80 mN and 68 mN respectively. Both the low resistivity wafer (0.016  $\Omega$ -cm) and high resistivity wafer (3 k $\Omega$ -cm) were similar in porosity, which likely contributed to similar thrust performance.

Table 3.3: Results as a function of wafer resistivity. The error is the standard deviation over 4 trials (3 trials for porosity).

Conc.	Depth ( $\mu\text{m}$ )	R ( $\Omega$ -cm)	P (%)	Equiv. Ratio	Peak Thrust (mN)	Imp ( $\mu\text{N} \cdot \text{s}$ )	$I_{sp}$
3:1	29.1	0.016	45.9 $\pm$ 1.7	17.7	68 $\pm$ 5.2	19 $\pm$ 1.4	23 $\pm$ 1.7
3:1	29.2	3.6	72.9 $\pm$ 5.7	5.57	662 $\pm$ 11.7	261 $\pm$ 18.2	320 $\pm$ 22.4
3:1	30.7	3000	37.1 $\pm$ 1.4	25.4	80 $\pm$ 32.1	23 $\pm$ 10.3	26 $\pm$ 10.9

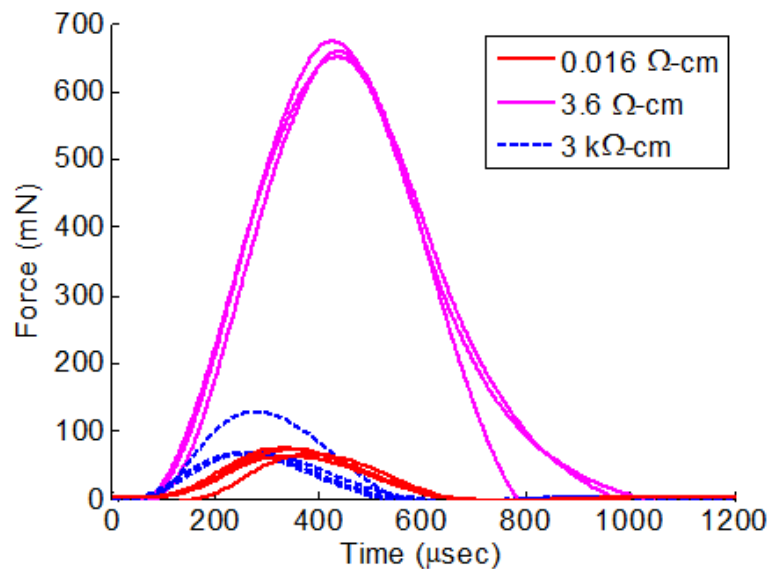


Figure 3.7: Thrust profiles based on the change in silicon wafer resistivity.

### 3.3.4 Pendulum Validation of Impulse Measurements

The pendulum experiment was performed to validate the thrust and impulse measurements collected using the Kistler 9215 force sensor. Porous silicon devices used in this experiment were etched using a 3:1 electrolyte ratio, where the etch depth was held at a target depth of 30  $\mu\text{m}$ . A total of three experiments were carried out using the pendulum and porous silicon devices of comparable porosity, with observed maximum angular displacements of  $9^\circ$ ,  $9^\circ$ , and  $13^\circ$ . An initial attempt to validate the pendulum experiment using only the maximum angular displacement resulted in lower than expected values for impulse. Therefore to validate the results collected by the pendulum, a least squares fit was performed on the displacement versus time data.

The author captured high-speed video of several pendulum oscillations at 2000 frames per second, one example of which is represented by the observed displacement data points in Figure 3.8, resulting in a calculated impulse of  $132 \mu\text{N} \cdot \text{s}$  ( $13^\circ$ ), which was on the same order as the measured result of  $261 \pm 18.2 \mu\text{N} \cdot \text{s}$  obtained using the force sensor. Using the same fit model terms applied to the other observed angular displacement of  $9^\circ$  resulted in a calculated impulse of  $100 \mu\text{N} \cdot \text{s}$ . Although these values were about half of the values measured by the force sensor, they do help to validate the approximate order of magnitude of results obtained with the force sensor. The lower impulse numbers obtained with the pendulum experiments were likely due to non-linearities not fully captured by the pendulum model, including rotational motion along the axis of the pen-

dulum arm, non-linear friction at the pivot, and a non-rigid pendulum arm.

Figure 3.9 shows still images of the thrust event. The first image shows the initial state of the micro-thruster. The second image shows the moment after ignition, while the third image shows the maximum displacement of the pendulum arm. Based on the maximum displacement at  $9^\circ$ ; the small angle approximation is valid. What appears to be small fragments of silicon being ejected from the surface of the porous silicon device are actually residual salt crystals from the sodium perchlorate being ejected from the device, further illustrating that residual oxidizer on the surface does not typically participate in the reaction.

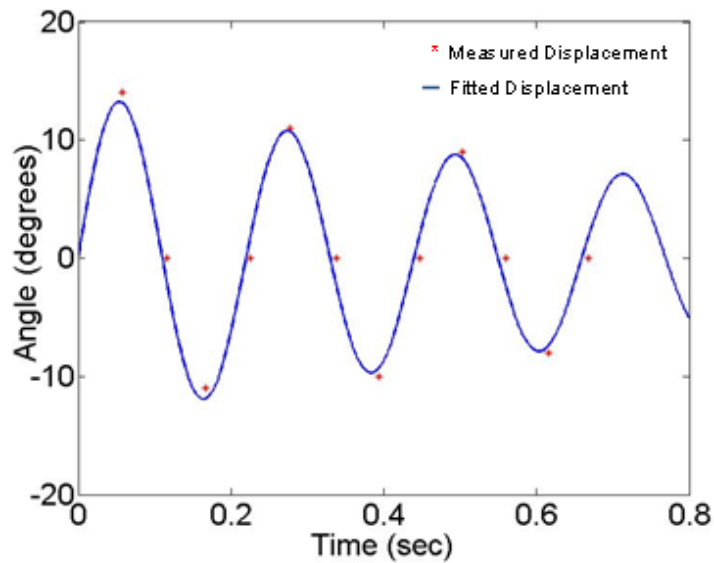


Figure 3.8: Angular displacement of the pendulum captured on high-speed video.

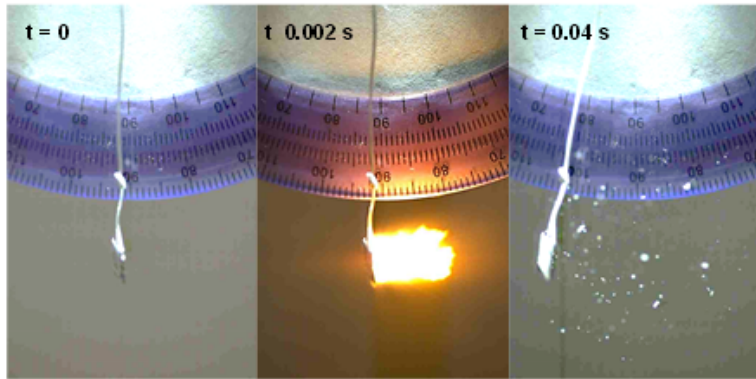


Figure 3.9: Side by side images showing  $9^\circ$  of displacement upon actuation.

## 3.4 Discussion

### 3.4.1 Use of Porosity instead of Surface Area and Pore Size in Porous Silicon

While the combustion performance of energetic porous silicon is directly affected by the pore size and surface area of the porous silicon, porosity is a much simpler quantity to measure for small area devices. Previous work showed that it is difficult to obtain reliable pore size and pore volume using volumetric analysis based on the Brunauer, Emmett, and Teller (BET) method for porous silicon mass below 3 mg [65]. A coupon of 4 porous silicon devices etched out of a single silicon chip for this study resulted in 250  $\mu\text{g}$  of porous silicon material, so a minimum of 12 coupons would be required for one BET measurement. In addition, the coupon would need to be cleaved or diced to fit in the tool's sample tube, likely resulting in additional errors from material loss during cleaving. The size

of the sample tube is constrained by the tool dimensions.

Porosity was measured along with surface area and pore size using the BET method for much larger samples (81 mm<sup>2</sup>) in previous work [57]. A sample etched with similar parameters to the best performing devices in the current study (3:1 etch solution ratio, 1-10 Ω-cm, and 36 μm) had a measured porosity of 72.9 % with a surface area of 895 m<sup>2</sup>/g and a pore size of 3.32 nm. The results from [57] demonstrated no clear trends between porosity and surface area or pore size, and that different combinations of the three may be easily fabricated. Therefore, a more extensive investigation of how thrust varies along the multidimensional axes of porosity, surface area, and pores size may be the subject of future study. However, it is interesting to note that devices with a porosity of approximately 70 % resulted in both the best propulsion performance in the current study, and the highest flame speeds in previous work [66, 57].

### 3.4.2 Thrust and Impulse based on Porosity

As shown in the results above, etchant concentration, porous silicon etch depth, and wafer resistivity all affected the porosity of the porous silicon devices. It is possible to compile a more general observed effect of porosity on thrust by combining the data collected. The results shown in Figure 3.4 exclude porosity variations due to etch depth as the volume of porous silicon was not held constant in these experiments. The data shown in Figure 3.10 are average values based on discrete data points from Tables 3.1 and 3.3, with connecting lines for

clarity. Thrust and impulse were highly correlated. This result is not surprising as the time over which thrust occurred was relatively constant, spanning only 0.6 - 1 ms in Figure 3.2, Figure 3.4 and Figure 3.7 . For porosities below 45 %, the measured thrust and impulse were relatively constant, while the significant increase in thrust and impulse at a porosity of approximately 73 % was most likely due to the more favorable fuel:oxidizer equivalence ratio. In order to reach an equivalence ratio of 1.0, a porosity of approximately 93 % is predicted.

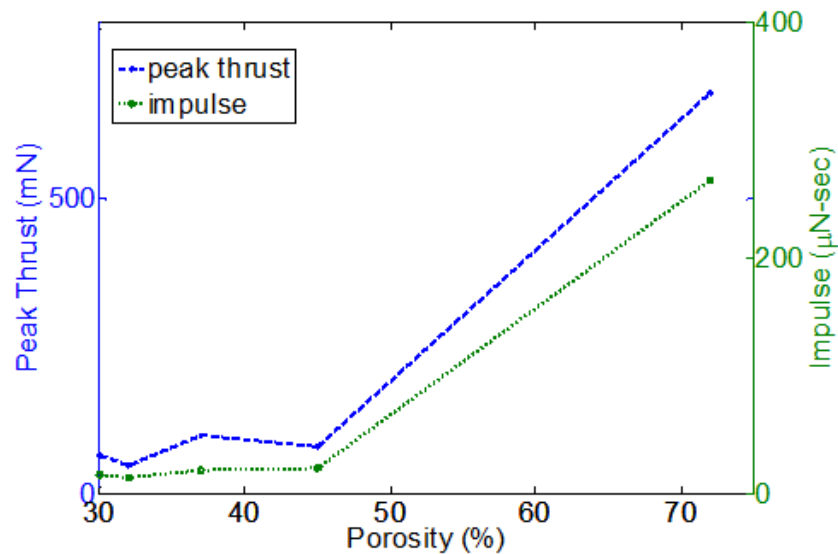


Figure 3.10: Comparison of impulse and peak thrust.

However, higher porosities may not necessarily result in higher thrust output. Although more data is required to better understand how thrust and impulse change with porosities above 73 %, it is interesting to note previous results in which the highest flame speeds occur near porosities of 70 %, but then drop as porosity increases further [57]. The reason for this drop in flame speed is primarily due to increased surface cracking, which is thought to allow additional

oxidizer to fill the larger voids between cracks, and act as an additional thermal load to slow the heating of unreacted porous silicon. In the present study, cracks in the samples featured in Figure 3.6 were also correlated to lower performance, although for different reasons. In this case, the cracks likely indicated additional mechanical instability of the film, which means it would have been more likely to be ejected under lower pressures, possibly before it even had a chance to fully burn. Therefore, it is plausible that increased porosity may only lead to increased cracks, and may act to reduce instead of increase thrust performance. In any case, more data at porosities above 73 % could lead to a better understanding of a possible optimal porosity for thrust.

### 3.5 Conclusion

In this chapter, propulsion performance metrics (peak thrust, impulse, and specific impulse) were measured for 3 mm<sup>2</sup> regions of unconfined energetic porous silicon that did not result in fracturing of the device chip. Propulsion performance metrics were shown to be dependent on the porosity of the porous silicon which was varied by changing the concentration of hydrofluoric acid to ethanol in the etch solution, the etch depth of porous silicon, and finally by changing the resistivity of the silicon wafer used for fabrication. Changing the hydrofluoric acid in the mixture of hydrofluoric acid to ethanol from 20:1 down to 3:1 resulted in a 16x increase in mean impulse (from 16  $\mu\text{N} \cdot \text{s}$  for the 20:1 to 261  $\mu\text{N} \cdot \text{s}$  for a 3:1 etch ratio). It was also shown that the highest propulsion performance was

measured for 30  $\mu\text{m}$  deep samples. Although deeper 40  $\mu\text{m}$  samples performed relatively well, the thrust output was not repeatable because of cracks that developed as a result of etching the porous silicon deeper. This produced both instability and variability in the porous silicon structure. The author also showed that when comparing wafer resistivity, porous silicon devices etched with 3.6  $\Omega\text{-cm}$  wafers outperformed both the lower and higher resistivity wafers by a 11x increase in impulse (from 23  $\mu\text{N} \cdot \text{s}$  for the 3000  $\Omega\text{-cm}$  to 261  $\mu\text{N} \cdot \text{s}$  for the 3.6  $\Omega\text{-cm}$  wafer). Based on the impulse data gathered, the 30  $\mu\text{m}$  deep porous silicon devices etched using a 3:1 ratio of hydrofluoric acid to ethanol with a 3.6  $\Omega\text{-cm}$  wafer performed better for propulsion.

## Chapter 4

### Scaling Effects for Multiple Thrust Events

#### 4.1 Introduction

Scaling micro-thrusters down in size to enable multiple propulsion events on smaller sub-centimeter platforms presents unique challenges to integration and thrust performance due to limitations in propellant size and spacing. While multiple propulsion events may be desirable, replenishing energy expended to achieve a single thrust event becomes difficult. Trade-offs between magnitude of thrust needed for propulsion and propulsion event density are based on the size and operational requirements of the platform. A 1-kg class nano-satellite for example, requires 10 to 1000  $\mu\text{N}$  of thrust, while a 10-kg micro-satellite requires thrust ranging from 0.1 to 10 mN for on-orbit maneuvering [38]. These systems are capable of reaching velocities ranging from 10 m/s to 1000 m/s. Some of these requirements can be met with solid-propellant micro-thrusters like that discussed in [67], which produces thrust ranging from  $\mu\text{N}$  to N using aluminum bismuth trioxide and aluminum iodine pentoxide nanoenergetic composites. When size is not a limiting factor, systems like the liquid micro-pulsed plasma thruster in [68] can generate thrust using a liquid propellant, stored in a 50  $\mu\text{L}$  tank, which is injected between high voltage electrodes. The necessary size, weight, and power is available to accommodate a micro-pump and control electronics.

Limitations to propulsion event density hold true for robots. At larger size scales it becomes less difficult to replenish stored chemical energy or mechanically reset a motor-spring system. For example, the robot in [69] uses a combustion-powered actuator to propel its own mass of 1.25 kg, along with an additional payload of 3.75 kg, to a height of 7.5 m. Jumping is demonstrated using on-board propane as the fuel, and nitrous oxide as the oxidizer. A mixture of propane and nitrous oxide is injected into a chamber and ignited by a glow plug and a filament, which is used as a catalyst to accelerate the reaction. The combustion event drives a piston downward, resulting in an opposite upward motion that propels the robot. The mechanism for propulsion, whether through the conversion of chemical or mechanical energy, is limited by the ability to replenish the energy. While finite operational lifespan is inevitable, the goal is to better understand the trade-offs between how much thrust can be produced from a single event, and how many of these events can be distributed on-board for maximum functionality.

## 4.2 Scaling Microthrusters

Attempts have been made to deliver multiple propulsion events at smaller size scales. The microthruster in [38] consists of an array of 15 solid propellant thrusters designed by stacking three wafers, including an initiator wafer with polysilicon heaters, a tank wafer, and a silicon diaphragm wafer. Ignition of a 100  $\Omega$  resistor with 100 V causes the resistor on the initiator wafer to vaporize, produc-

ing a pressure wave that ignites 1 mg of lead styphnate primary explosive. Arrays of resistors allow for selective ignition of one or more thrusters at a time. A single thruster can generate an impulse of  $1.8 \text{ mN} \cdot \text{s}$ . The solid propellant micro-thruster array in [11] has 100 individually addressable  $1.5 \text{ mm}$  by  $1.5 \text{ mm}$  thrusters in a total area of  $576 \text{ mm}^2$ , and each micro-thruster can generate thrust ranging from  $0.3$  to  $2.3 \text{ mN}$ . The solid propellant micro-thruster in [70] consists of 36 chambers, with chamber diameter of  $1.5 \text{ mm}$  and length of  $3.6 \text{ mm}$ . Using a formulation of ammonium perchlorate and glycidyl azide polymer, each thruster can produce  $0.18$ - $0.29 \text{ mN}$  of thrust. At these size scales the ability to replenish fuel and oxidizer becomes difficult and these thrusters serve a one-time use function, increasing the need to array multiple devices for greater propulsion event density.

Propulsion of microrobots has been demonstrated at the centimeter scale and below by converting stored energy, such as elastomeric or spring energy, into kinetic energy. Achieving a vertical jump height of  $1.2 \text{ cm}$ , the  $10 \text{ mg}$  autonomous microrobot in [7] uses micro-rubber bands that are actuated with an electrostatic inchworm motor. The elastomer must be physically stretched to store  $4.9 \text{ nJ}$  of energy into the rubber band. The miniature robot in [71] uses a shape memory alloy (SMA) spring actuator to propel itself to a vertical jump height 30 times its body size. With a body size of  $2 \text{ cm}$ , and a weight of  $1.1 \text{ g}$ , the robot is size-limited and unable to carry an on-board  $3.7 \text{ V}$  ( $10 \text{ mAh}$ ) battery needed to heat the actuators. Power must be supplied off-board to heat the actuators, which also require time to cool down before initiating further jumps. The magneto-elastic soft milli-robot

in [72], measuring 3.7 mm in length and 1.5 mm in width, is made of a silicone elastomer embedded with magnetic neodymium-iron-boron microparticles. The milli-robot can roll, walk, and jump over standing obstacles, but requires external magnetic actuation using custom-made electromagnets, whose size is not negligible. These propulsion systems are impressive in terms of design, capability, and ingenuity, but each platform has limitations to achieving multiple propulsion events, which are dictated by size.

In this work, the author first studied the dependency of thrust and impulse generated by porous silicon as a function of the porous silicon area for a single thrust event. Four different areas of porous silicon were investigated: 1.6 mm<sup>2</sup>, 3.2 mm<sup>2</sup>, 4.8 mm<sup>2</sup>, and 6.4 mm<sup>2</sup>. The etch depth for each device was nominally 25 μm (deeper etched devices shattered upon ignition). The author also studied the effects of simultaneous ignition and scaling the area of energetic porous silicon. Thrust and impulse generated by a single 4.8 mm<sup>2</sup> energetic porous silicon device was measured, and compared with three individual 1.6 mm<sup>2</sup> devices that were electrically connected in parallel, with the area of the three smaller devices equivalent to the single larger device. Finally, the author studied the critical spacing between adjacent devices in an attempt to mitigate potential sympathetic ignition between adjacent devices and to determine the trade-offs between thrust and impulse and the density of micro-thrusters that could be integrated on a 1 cm<sup>2</sup> chip. This was important to enable the fabrication of multiple micro-thruster devices on a single chip.

### 4.3 Fabrication

While details of the porous silicon fabrication process were discussed in Chapter 2, variations to the geometry of the bridgewire design were necessary when scaling the area of the porous silicon fabricated for the scaling study. The bridgewire initiator was lithographically patterned, and a metal stack consisting of 100 Å Cr, 1000 Å Pt, and 3800 Å of Au was evaporated (Evatec BAK 641 Ebeam Evaporator) and patterned by lift-off. The metal stack was chosen to ensure low electrical resistance (approximately  $3\ \Omega$ ), and therefore low ignition voltage. The electronic igniter in Figure 4.1 was designed with a tapered bow-tie structure at the center of the initiator. The length of the initiator at the center of the bow-tie varied from 75  $\mu\text{m}$  to 150  $\mu\text{m}$ , and the width varied from 18.75  $\mu\text{m}$  to 37.5  $\mu\text{m}$  respectively depending on the size of the porous silicon, which ranged from 1.6  $\text{mm}^2$  to 6.4  $\text{mm}^2$ . Larger, 2 mm by 2 mm square bond pads were added to the initiator design to enable electrical contact to the initiator via probe tips or wires that could be soldered to the pads. Even with the variability in the design of the initiator, porous silicon devices were consistently ignited at 6V and a current limit set at 120 mA. The wafer was then coated with photoresist and diced into smaller pieces, called coupons. Figure 4.1 shows a silicon coupon consisting of three individual 2 mm diameter devices, as well as a zoomed in view of the bridgewire. Before etching, coupons were coated with photoresist, and diced out of the wafer with a Disco DAD 3240 dicing saw. A pre-clean of the wafer with acetone, methanol, and deionized wafer was performed to remove photoresist on the individual coupon,

prior to etching.

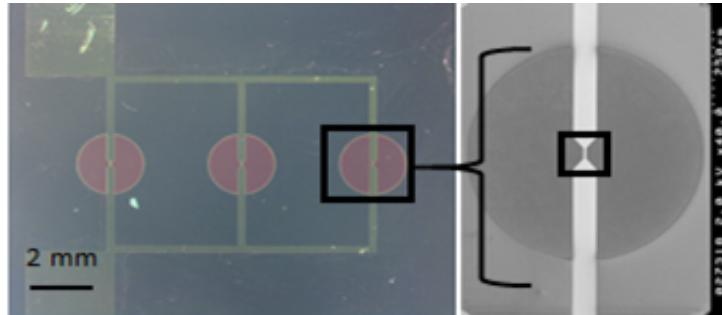


Figure 4.1: (Left) Silicon coupon consisting of three porous silicon devices with initiators connected in parallel (Right) Close-up of the initiator used to electrically ignite the porous silicon

The galvanic etch was performed by submerging the coupon in an etch bath consisting of a mixture of 3:1 hydrofluoric acid to ethanol, with 0.48 % hydrogen peroxide by volume. The etch time was chosen to maintain a nominal etch depth of 25  $\mu\text{m}$  across the coupons with devices of varied areas. For sympathetic ignition studies the etch time was reduced to maintain nominal etch depth of 7  $\mu\text{m}$ . Etch depth was measured by dissolving porous silicon in a mixture of water and sodium hydroxide, and measuring the step height using a stylus profilometer. In general the etch rate depended on wafer resistivity and the ratio of exposed silicon to backside platinum. Therefore the etch time was varied to account for these variables to the galvanic etch process. Upon completion of the etch, the devices were stored in a nitrogen dry box prior to performing force measurements to minimize surface oxidization of the pores. Once the devices were ready to activate, a 1  $\mu\text{L}$  drop of 3.2 M of sodium perchlorate was dispensed onto the porous silicon and allowed to dry for 30 minutes. Tests were performed in a dry room

with the relative humidity regulated to below 1 %.

## 4.4 Experimental Methods

### 4.4.1 Area Scaling Study

The dependency of thrust and impulse on the area of the porous silicon available to react was studied by varying the area of energetic porous silicon and holding the etch depth constant. Devices were lithographically patterned and etched with areas of 1.6 mm<sup>2</sup>, 3.2 mm<sup>2</sup>, 4.8 mm<sup>2</sup>, and 6.4 mm<sup>2</sup>. Force measurements were performed on a total of 16 devices. Four devices were tested for each area being studied. While the area was varied based on the diameter of the porous silicon device, efforts were taken to ensure that the etch depth across each sample set was held at a nominal depth of 25 μm. Etching deeper resulted in potential cracking of the porous silicon, which manifests in variability in the thrust measurements as shown in [62]. The resistivity of the silicon wafers varied from 5-8 Ω-cm.

### 4.4.2 Simultaneous Ignition Study

In addition to measuring thrust and impulse of individually scaled energetic porous silicon devices, the author compared propulsion performance of a single (4.8 mm<sup>2</sup>) device with that of three (1.6 mm<sup>2</sup>) connected in parallel and triggered simultaneously as shown in 4.2. Both sets of devices were etched using a 5.2 Ω-cm wafer for four minutes. The nominal etch depth for both sets of devices was 25 μm. After etching, 1 μL of 3.2M of sodium perchlorate was applied to each

device and allowed to dry for 30 minutes. The authors performed two force measurements for each of set of devices.

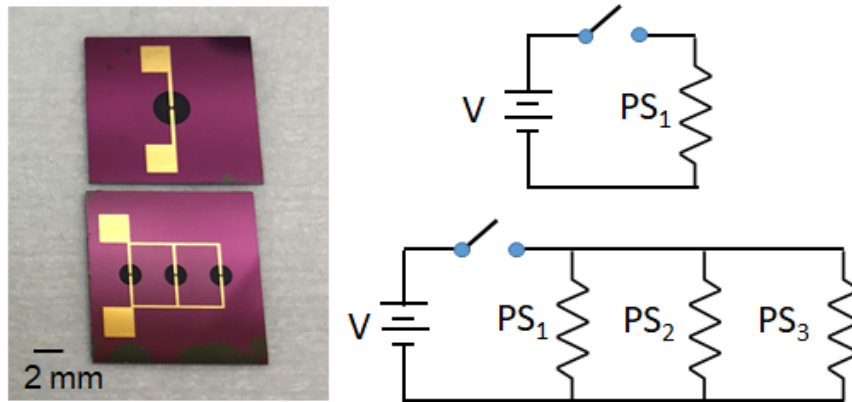


Figure 4.2: (Left) Illustration of a single  $4.8 \text{ mm}^2$  porous silicon device. Illustration of three individual  $1.6 \text{ mm}^2$  devices with individual bridgewires connected in parallel. (Right) Circuit schematic illustrating the resistor elements (bridgewire) for each porous silicon device.

### 4.4.3 Sympathetic Ignition Study

A study was done to determine the critical spacing between energetic porous silicon devices that was necessary to prevent sympathetic ignition. Two different areas of porous silicon devices were tested:  $1.6 \text{ mm}^2$  and  $3.2 \text{ mm}^2$ . These were chosen because they enabled the placement of more individual devices on a single  $1 \text{ cm}^2$  silicon chip. For each area, an array of six porous silicon devices, similar to that shown in Figure 4.3, was lithographically patterned and etched into a single coupon. For the coupon consisting of adjacent  $1.6 \text{ mm}^2$  devices, the spacing was increased from  $125 \mu\text{m}$  up to  $1500 \mu\text{m}$  as specified in Table 4.1. A total of four coupons were etched and tested for this specific area study. The coupons were

etched using a 3:1 mixture of hydrofluoric acid and ethanol, along with 0.96 mL of hydrogen peroxide in a galvanic electrochemical etch process. Although electrical bridgewire initiators were located on each porous silicon device, only one bridgewire was wirebonded to enable electrical ignition of a single porous silicon device. One micro-liter of sodium perchlorate oxidizer (3.2M) was applied to each device using a micro-pipette and allowed to dry for 30 minutes in a dry room prior to ignition.

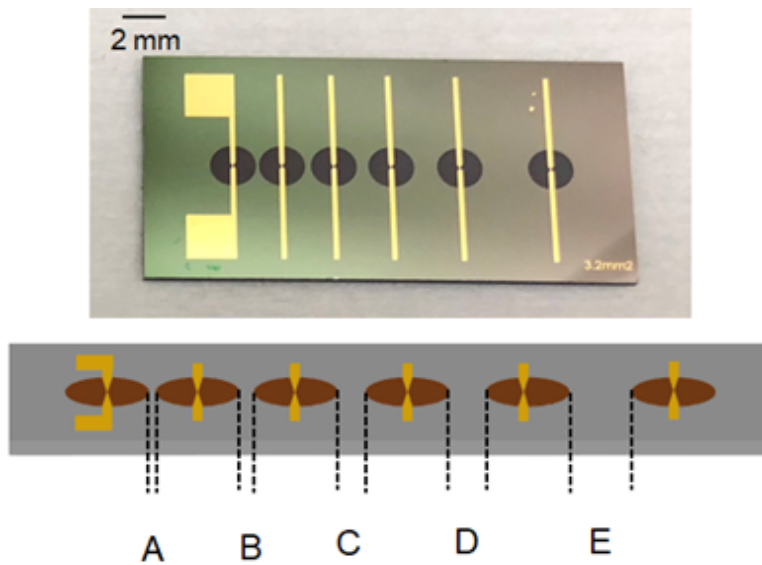


Figure 4.3: Illustration of device spacing for sympathetic ignition study.

Table 4.1: Summary of nominal separation distance (in microns) between adjacent devices

Gap	PS Area = 1.6 mm <sup>2</sup>	PS Area = 3.2 mm <sup>2</sup>
A	125 μm	125 μm
B	250 μm	250 μm
C	500 μm	500 μm
D	1000 μm	1000 μm
E	1500 μm	2000 μm

A total of three experiments were performed on the array of 3.2 mm<sup>2</sup> devices. One coupon, consisting of six individually spaced porous silicon devices, was etched for 3 minutes, a second coupon was etched for 1 minute, and a third for 30 seconds. The nominal gap spacing was increased from 125 μm to 2000 μm. These coupons were etched using a 3:1 mixture of hydrofluoric acid and ethanol. 3.2M of sodium perchlorate was applied to each porous silicon device and ignition was attempted in a similar fashion to the 1.6 mm<sup>2</sup> area devices. Sympathetic ignition was determined by electrically triggering a single bridgewire on each coupon and performing high speed video using a Photron FasCAM to capture the resulting ignition event at 100,000 frames per second. The porous silicon coupon was attached to a dual in-line package using double-sided Kapton tape to enable wirebonding between the porous silicon bridgewire and the electronics package.

## 4.5 Results

### 4.5.1 Area Scaling Study

A total of 16 experiments were performed to study the effects of scaling the area of porous silicon on the thrust and impulse produced. Four experiments were performed for each of the four areas evaluated in this study. Figure 4.4 shows the average force generated by each set of devices represented by the solid lines. The shaded boundaries represent average thrust plus and minus the standard deviation for each of the porous silicon areas studied. Table 4.2 summarizes the

average impulse as a function of area, and Table 4.3 summarizes the average force as a function of area.

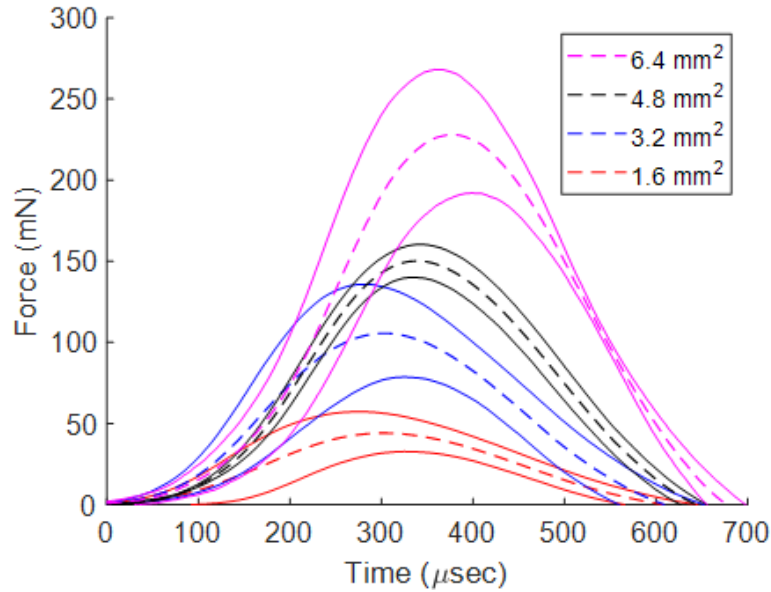


Figure 4.4: Plot of force versus time as a function of the porous silicon device area. Dashed lines represent average thrust, while solid lines represent upper and lower bounds of standard deviation.

Table 4.2: Summary of average impulse, and minimum and maximum impulse as a function of porous silicon area

Area	Avg ( $\mu\text{N} \cdot \text{s}$ )	Min ( $\mu\text{N} \cdot \text{s}$ )	Max ( $\mu\text{N} \cdot \text{s}$ )	Stdev ( $\mu\text{N} \cdot \text{s}$ )
1.6 mm <sup>2</sup>	13.5	8.0	19.2	3.2
3.2 mm <sup>2</sup>	31.9	20.3	43.5	9.3
4.8 mm <sup>2</sup>	44.9	40.2	49.5	1.5
6.4 mm <sup>2</sup>	84.0	45.5	126.7	38.6

Table 4.3: Summary of average force, and minimum and maximum force as a function of porous silicon area

Area	Avg (mN)	Min (mN)	Max (mN)	Stdev (mN)
1.6 mm <sup>2</sup>	44.1	32.7	57.3	9.6
3.2 mm <sup>2</sup>	105.6	78.6	135.7	28.7
4.8 mm <sup>2</sup>	150.2	140.1	160.5	5.0
6.4 mm <sup>2</sup>	259.7	194.0	346.0	104.9

Area scaling experiments were performed for shallower porous silicon etches. Thrust profiles shown in Figure 4.5 were measured for the a single  $1.6 \text{ mm}^2$  device with a nominal etch depth of  $7 \mu\text{m}$  and for a single  $3.2 \text{ mm}^2$  device with a nominal etched depth of  $7 \mu\text{m}$  to further study the trade-offs between device density and achievable thrust and impulse. A single  $3.2 \text{ mm}^2$  device produced an average peak thrust of  $30 \text{ mN}$ , and an average impulse of  $8.5 \mu\text{N} \cdot \text{s}$  based on two measurements taken with the force sensor. A single  $1.6 \text{ mm}^2$  device produced an average peak thrust of  $13.1 \text{ mN}$ , and an average impulse of  $3.7 \mu\text{N} \cdot \text{s}$  based on two measurements taken.

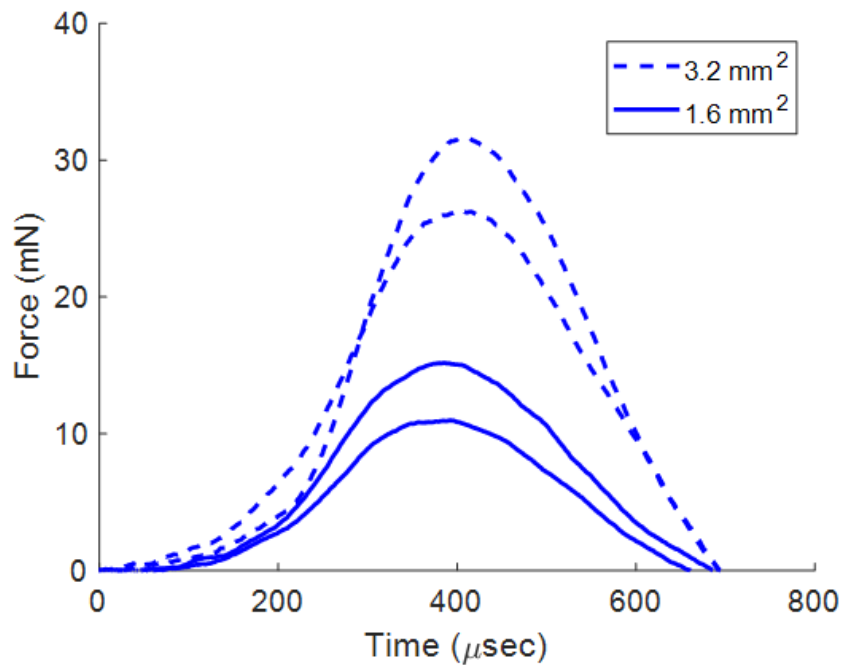


Figure 4.5: Plot of force versus time as a function of the porous silicon device area for  $7 \mu\text{m}$  deep porous silicon etch.

## 4.5.2 Simultaneous Ignition Study

Force and impulse were measured for a single 4.8 mm<sup>2</sup> device with a nominal etch depth of 20 μm. The measurement was repeated twice, and produced an average peak force of 113.7 mN and an average impulse of 28.7 μN · s. Similarly, an array of three 1.6 mm<sup>2</sup> devices, electrically connected in parallel, were ignited simultaneously. The test was repeated twice and each time the three devices produced a waveform consisting of two consecutive peaks, as shown in Figure 4.6. The average peak forces measured were 36.3 mN and 64.9 mN, with an average impulse of 30.6 μN · s. Table 4.4 summarizes numerical values for the average peak force and the average impulse generated for the different devices.

To explain the consistent double peak result from the simultaneous ignition of three devices, several hypotheses are explored. The peaks are separated by approximately 500 μs and can result from consistent delayed ignition between devices or might be an artifact from the measurement setup, specifically the force sensor. In previous tests of simultaneous ignition of multiple devices captured with high speed video, it was too challenging to separate out any delayed ignition from the video itself due to saturation in the images captured at 100,000 fps during ignition. Therefore, high speed video was not used as a diagnostic tool during these tests.

The first hypothesis is that the parallel ignition results in delays in ignition due to less power delivered to each device. The three (1.6 mm<sup>2</sup>) devices evaluated in the simultaneous ignition study were connected in parallel, each having an in-

tegrated initiator. Ignition was controlled using a Keithley 2400 Sourcemeter, at 6 V, with a current limit set to 1 A. Each initiator had a resistance of approximately 3  $\Omega$ . As a result of the wiring configuration shown in Figure 4.2, each device in the ignition sequence sees approximately 1/3 the current initially imparted through the first initiator. Therefore, in the 3-device case, approximately 1/3 W is being applied to each device versus 3 W for the single device. While this is a significant reduction in power applied to each bridgewire, it is not expected to create any ignition delays between devices due to this lower current. Future tests could measure variability between ignition and reaction with high speed video synced to the sourcemeter to confirm this.

The second hypothesis is that the double peaks result from how the chip was mounted. For single device measurements, care was taken to mount the sensor directly beneath the porous silicon. However, this was not possible with three active devices. While the sensor bandwidth is nominally reported as  $> 50$  kHz in frequency, it is possible that another resonance is being excited due to the applied moments from the off-center devices. Unfortunately, the datasheet does not provide more information about additional sensor resonant frequencies. Future tests could combine the nozzles developed in Chapter 6 with this experiment to better combine the three device reactions into a single reaction.

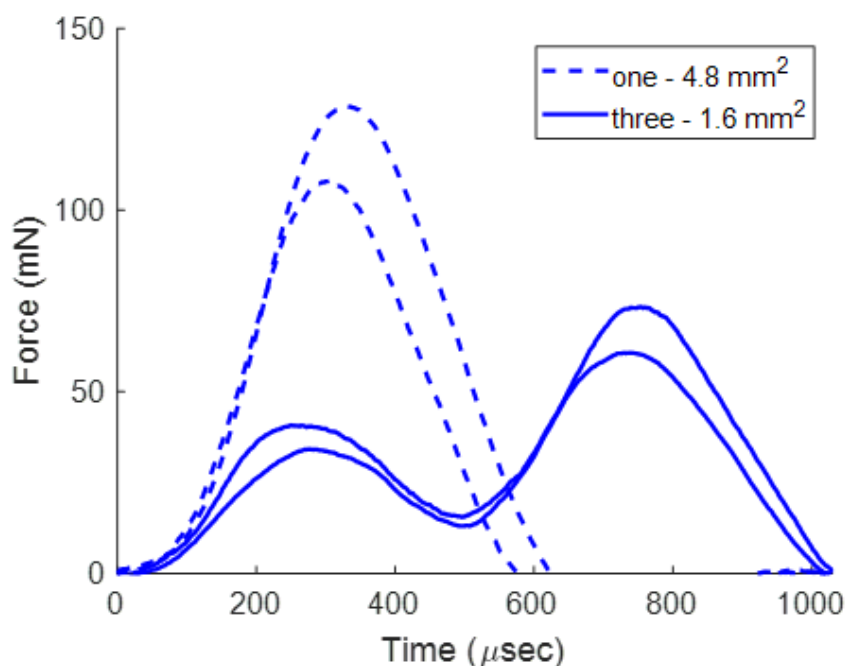


Figure 4.6: Force versus time for single ( $4.8 \text{ mm}^2$ ) device versus three ( $1.6 \text{ mm}^2$ ) devices. Experiment repeated twice

Table 4.4: Summary of peak force and impulse for a single  $4.8 \text{ mm}^2$  device in comparison to three  $1.6 \text{ mm}^2$  devices connected in parallel and ignited simultaneously. Results from the first of two experiments shown.

Sample	Peak Force (mN)	Impulse ( $\mu\text{N} \cdot \text{s}$ )
$4.8 \text{ mm}^2$ (one)	113.7	28.7
$1.6 \text{ mm}^2$ (three)	36.3, 64.9	30.6

Figure 4.7 shows high speed video frames captured of the reaction event for a single porous silicon device with an area of  $4.8 \text{ mm}^2$  (top image), and three porous silicon devices, each having an area of  $1.6 \text{ mm}^2$ , ignited simultaneously. The three devices were electrically connected in parallel in an attempt to simultaneously trigger all three devices. For the simultaneous ignition study, high speed video for each event was captured at 50 kfps rather than 100 kfps to enable a

higher resolution image. The nominal etch depth was  $20\ \mu\text{m}$  because at  $25\ \mu\text{m}$  the coupon consisting of three  $1.6\ \text{mm}^2$  devices fractured upon ignition.

Based on a qualitative observation, both devices generated a similarly large plume of hot particulates, which consumed the field of view on a 256 by 256 pixel resolution window. After approximately 10 frames, the flame front moved away from the surface of the energetic porous silicon. Appropriate steps should be taken when arraying these solid-propellant devices to ensure that undesirable sympathetic ignition does not occur. If sympathetic ignition was indeed the result of hot particulates landing on adjacent devices, a nozzle could be incorporated to direct the flow of hot particulates away from adjacent devices. Further study could be done to determine if sympathetic ignition was the result of flame jumps.

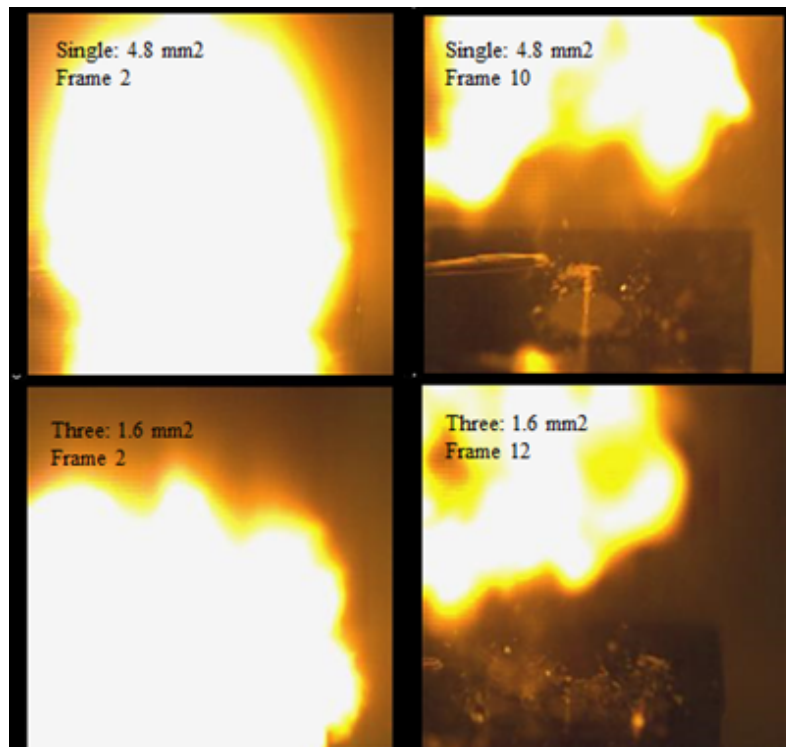


Figure 4.7: High speed frame capture of a single ( $4.8\ \text{mm}^2$ ) device reacting in comparison to three ( $1.6\ \text{mm}^2$ ) devices reacting simultaneously

### 4.5.3 Sympathetic Ignition Study

The array of  $1.6 \text{ mm}^2$  porous silicon devices was etched for 1 minute producing porous silicon with a nominal etch depth of  $10 \mu\text{m}$  (average etch depth of  $11.15 \mu\text{m}$  and standard deviation of  $0.49 \mu\text{m}$ ). All porous silicon devices ignited even at the largest device spacing of  $1500 \mu\text{m}$ . The etch time was reduced to 30 seconds, which produced porous silicon with a nominal etch depth of  $7 \mu\text{m}$  (average etch depth of  $7.34 \mu\text{m}$  and standard deviation of  $0.63 \mu\text{m}$ ). At this etch depth, the reaction propagated across five of the six devices, but failed to ignite the last device that was spaced  $1500 \mu\text{m}$  from its closest neighbor. Figure 4.8 shows a series of still images from the high speed video capture. The picture in the top left corner shows that the three closest devices appear to ignite almost simultaneously. After the visible plum of ejected gas appears to clear, there is an ignition of the fourth and fifth devices. These ignition events appear to happen independent of each other. The critical spacing measured in these experiments might be an upper bound, especially if potential effects of shock or heat transport can be mitigated are causing sympathetic ignition. Ideally if only igniting one pixel, then it might be possible to space adjacent devices closer.

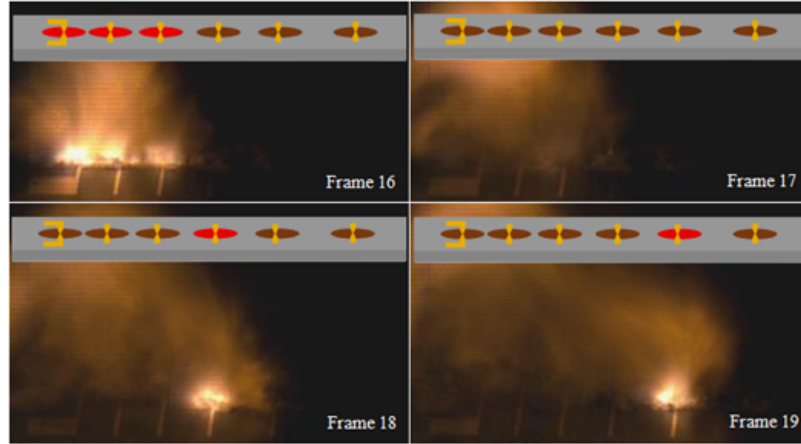


Figure 4.8: High speed video capture of series of  $1.6 \text{ mm}^2$  devices etched for 30 seconds.

The experiment was repeated twice with representative etch depths, and in both cases, four of the six devices reacted as shown in Figure 4.9. The critical gap spacing to prevent sympathetic ignition was  $1000 \mu\text{m}$  for a  $1.6 \text{ mm}^2$  diameter porous silicon micro-thruster with a depth of  $7 \mu\text{m}$ .

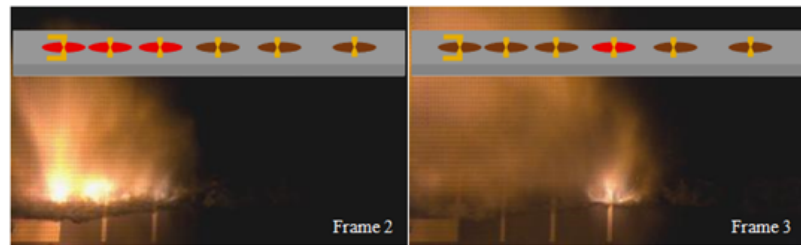


Figure 4.9: High speed video capture of series of  $1.6 \text{ mm}^2$  devices etched for 30 seconds.

For the devices having an area of  $3.2 \text{ mm}^2$ , the first experiment was performed on a coupon that was etched for 3 minutes. The nominal etch depth was  $30 \mu\text{m}$  (with an average etch depth of  $29.8 \mu\text{m}$ ) and a standard deviation of  $2.8 \mu\text{m}$ ). For the 3 minute etch, all five of the adjacent devices reacted spontaneously to the single ignition event. The etch time was reduced to 1 minute, resulting in a nominal etch depth of  $10 \mu\text{m}$  (average depth of  $8.9 \mu\text{m}$  and a standard

deviation of  $0.8\ \mu\text{m}$ ). Again, as shown in Figure 4.10, all of the devices reacted. The visible result showed an initial fireball in the first frame, which appeared to be the combined output of three adjacent devices. In the second and subsequent frames, the plume engulfed the entire capture window and saturated the camera optics at 100,000 fps.

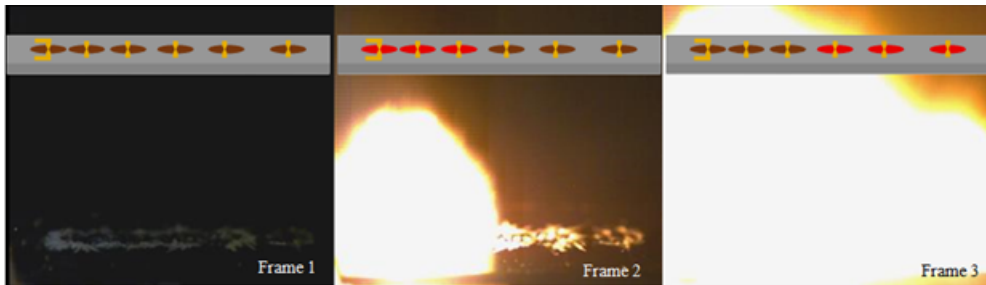


Figure 4.10: Still frames showing the sympathetic ignition of  $3.2\ \text{mm}^2$  porous silicon devices etched for 3 minutes

The etch time was reduced from 1 min to 30 sec, and the nominal etch depth was  $7\ \mu\text{m}$  (with an average etch depth of  $6\ \mu\text{m}$  and a standard deviation of  $0.5\ \mu\text{m}$ ). As a result, five of the six devices reacted, and the device spaced farthest,  $2000\ \mu\text{m}$ , from its adjacent neighbor did not react sympathetically. A summary of the separation distance based on the area of energetic porous silicon is summarized in Table 4.5

Table 4.5: Summary of average force, and minimum and maximum force as a function of porous silicon area

Area	Etch Depth ( $\mu\text{m}$ )	Separation ( $\mu\text{m}$ )
$1.6\ \text{mm}^2$	7	1000
$3.2\ \text{mm}^2$	7	2000

To better understand the causes of sympathetic ignition, approximate propagation rates were calculated from the high speed video available. The high-speed video (100,000 fps) images shown in Figure 4.8 from the 1.6 mm<sup>2</sup>, 7 μm deep porous silicon devices showed three devices igniting in the first frame, and the fourth device igniting two frames, or 20 μs later. Based on the separation distance of 500 μm between the third and fourth devices, an approximate propagation rate of 25 m/s was calculated. Based on the high-speed video (100,000 fps) captured for the sympathetic ignition of 7 μm deep, 1.6 mm<sup>2</sup> devices, shown in Figure 4.9, the first three devices again ignited simultaneously during a single frame. The fourth device ignited one frame later, indicating a 10 μs delay. Given the separation distance of 500 μm, propagation rate of 50 m/s was calculated. The 3.2 mm<sup>2</sup> devices in Figure 4.10 showed the first three devices igniting during a single frame, and the remaining three devices igniting one frame later. The separation distance between the third and fourth devices was 500 μm, resulting in a minimum propagation rate of approximately 50 m/s.

Several hypotheses are explored as the cause of this sympathetic ignition given these relatively low propagation rates of approximately 25-50 m/s. The first hypothesis is that shock waves from the initial ignitions caused the sympathetic ignitions. Based on the relatively low propagation rates measured, it is unlikely that sympathetic ignition is the result of a shock wave traveling through the silicon. It has been reported in [73] that based on measurements made using transducers, the speed of sound in porous silicon with a porosity of 50 % is close to 4500 m/s. The speed of sound in pure silicon is 8450 m/s [73].

A second hypothesis is that the ignition of adjacent devices might be the result of thermal conduction associated with hot particulates ejected from one device then landing on the nearest device. From projectile physics, the time for the projectile to travel and land will be defined by  $t = 2 \cdot v_i \cdot \sin(\theta) / g$ , where  $v_i$  is the initial velocity of the particle,  $\theta$  is the takeoff angle, and  $g$  is gravity. To get a time on the order of 10's of microseconds, the takeoff velocity needs to be very low (on the order of 1 cm/s with an extra small  $\theta = 1^\circ$ ). This results in a very small distance traveled ( $d = t \cdot v_i \cdot \cos(\theta)$ ) on the order of 100s of nm. As a result, this hypothesis seems very unlikely. In future work it would be worth acquiring the proper optics for the high speed camera to analyze the reaction front without saturating the optics.

A third hypothesis is thermal conduction through the silicon. Once again, many simplifying assumptions are made to test this hypothesis. While reaction temperature was not measured for porous silicon, a reasonable estimate is on the order of 3000 K [49]. Previous unpublished work by the author has shown that porous silicon will react when heated to approximately 450 K. Using the heat flow equation, the approximate time required to reach this 450 K temperature 0.5 mm away through silicon can be calculated. In this case, the author roughly estimates that the area is 1 mm x 0.01 mm based on the dimensions of each pixel. The change in heat is approximated as 10  $\mu$ J based on previous work showing the electrical energy required to ignite the porous silicon as 20  $\mu$ J. Thermal conductivity of silicon at around 1000 K is 30 W/m-K. Therefore, a very approximate time can be calculated as  $dt = DQ \cdot x / K / A / DT$ . This time is on the order of 6  $\mu$ s.

Despite the very approximate nature of this back of the envelope calculation, this result makes this a very strong hypothesis for sympathetic ignition. Future studies could create isolation trenches in the silicon between pixels to test this hypothesis further.

## 4.6 Discussion

The results in Figures 4.4 and 4.5 showed a clear trend when increasing the available reactive porous silicon area with an increase in measured thrust and impulse. The thrust and impulse scaled proportionally with the area of energetic porous silicon as shown in Figure 4.11. It was also shown in Figure 4.6 that when comparing the ignition of a single device ( $A = 4.8 \text{ mm}^2$ ) to that of three devices ( $A = 1.6 \text{ mm}^2$  each) connected in parallel and ignited simultaneously, the single device produced a force profile with a single, but larger peak thrust. The array of  $1.6 \text{ mm}^2$  devices produced multiple thrust peaks that were smaller in amplitude. However, the measured impulse for the single thruster was approximately equivalent to that produced by the three smaller thrusters ignited simultaneously. The ability to tune the thruster performance to optimize peak thrust or impulse offers advantages depending on how the thrusters are used for displacement and/or position correction. Certain applications, such as altering directionality of a nano-satellite in flight, may require smaller applied forces but larger impulse to generate necessary changes in linear momentum and velocity. The application of lower forces and larger impulse may be relevant in

environments where the effects of drag are minimal. This may prove beneficial for maneuvering micro-robots, where because of their small size scale and lower speeds, the effects of drag are smaller and they can more easily jump or traverse through air. For larger objects that are more susceptible to the effects of drag, or operating in turbulent environments, the platform may require a single thrust event that produces a larger peak force in order to achieve displacement.

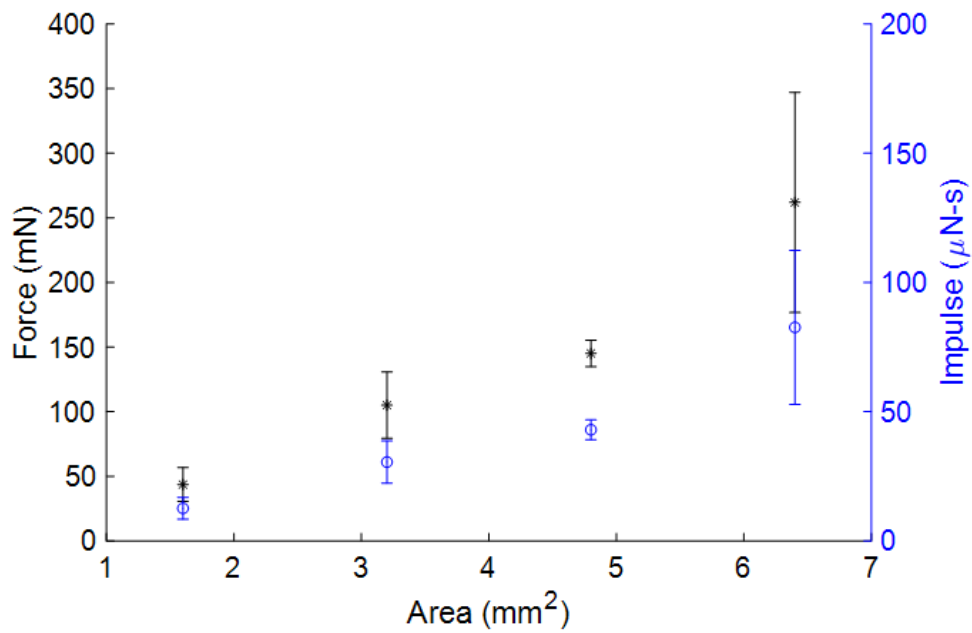


Figure 4.11: Summary of force and impulse as a function of porous silicon area plotted with error bars.

The data also showed that for a given porous silicon layer thickness, there was a minimum separation required between adjacent devices to prevent sympathetic ignition. While this minimum separation depended on the amount of material available to react, other potential dependencies may exist with regards to how the reaction propagates, whether through thermal conduction or a shock wave in

the silicon substrate. Generally the author observed that increasing the nominal etch depth to 30  $\mu\text{m}$  resulted in mechanical fracturing of the silicon chip, which made it difficult to integrate multiple devices for multiple propulsion events. For the purpose of this work, the author tailored the etch depth to avoid physically fracturing the chip, as well as identified an etch depth of 7  $\mu\text{m}$  based on the existing porous silicon geometry to show the avoidance of sympathetic ignition.

Table 4.6 summarizes the trade-offs between porous silicon micro-thruster density assuming integration of individual micro-thruster devices on a 1  $\text{cm}^2$  silicon die. Taking into account the minimum separation for the two different areas studied, the thruster chip composed of 4 individual 3.2  $\text{mm}^2$  provides more than twice as much thrust for a single device, but is limited to a total of four thrust events. The smaller (1.6  $\text{mm}^2$ ) devices allow for an array of 16 thrusters per square centimeter, where a single 1.6  $\text{mm}^2$  device generates approximately half the thrust and impulse of a single device 3.2  $\text{mm}^2$  device. If all devices were intentionally ignited simultaneously, the smaller 1.6  $\text{mm}^2$  would generate a combined thrust that is almost twice as large in comparison to the 3.2  $\text{mm}^2$ , and similar total impulse. Based on the performance tradeoffs, the decision to choose one area over another depends on the application as well as the amount of space available to integrate the thrusters.

An array of 3.2  $\text{mm}^2$  devices may be advantageous for a platform requiring larger thrust and impulse bits, while operating under constant force such as gravity, and turbulent flow resulting in the effects of drag. For smaller platforms to

Table 4.6: Summary of propulsion event density, along with thrust and impulse measurements based on the number of micro-thrusters per  $\text{cm}^2$ .

Area per device ( $\text{mm}^2$ )	1.6	3.2
No. Devices/ $\text{cm}^2$	16	4
Single thrust (mN)	13.1	30.0
Single impulse ( $\mu\text{N} \cdot \text{s}$ )	3.7	8.5
Simultaneous thrust (mN)	209.6	120
Simultaneous impulse ( $\mu\text{N} \cdot \text{s}$ )	59.2	34.0

redirect position or orientation under low drag conditions, the smaller impulse bits produced by the smaller ( $1.6 \text{ mm}^2$ ) porous silicon micro-thrusters may be sufficient, but have the advantage that two of the  $1.6 \text{ mm}^2$  device can combine to produce approximately the same single thrust and impulse as a single  $3.2 \text{ mm}^2$ , while leaving 14 out of the 16 available to react at a later time. From the standpoint of thrust event density, the array of sixteen  $1.6 \text{ mm}^2$  devices gives an 8:1 event density ratio, when two  $1.6 \text{ mm}^2$  devices are combined to produce comparable thrust to that of a single  $3.2 \text{ mm}^2$  device. This has the potential for larger achievable jump heights on a smaller platform due to the increased number of micro-thrusters available to react. This can also translate into great maneuverability to change directions when traversing rough terrain because of the ability to electrically program a greater number of thruster ignition sequences to have greater combined effects. While this is beyond the scope of this work, having the option to ignite single or multiple propellant devices simultaneously or sequentially can provide larger achievable jump heights, especially when micro-thrusters can be ignited mid-flight.

## 4.7 Summary

In this work, the author demonstrated the effects of scaling the area of energetic porous silicon on the thrust and impulse generated. Scaling the area of the energetic porous silicon, while holding the etch to a nominal depth of 25  $\mu\text{m}$ , resulted in a 6X increase in average peak force, from 44.1 mN to 259.7 mN, and average impulse, from 13.5  $\mu\text{N} \cdot \text{s}$  to 84  $\mu\text{N} \cdot \text{s}$ . In addition to scaling the area, the authors also scaled the amount of porous silicon by fabricating an array of porous silicon devices, whose combined area was equivalent to that of a single larger device. The measured force and impulse for the array of devices was determined by electrically connecting the devices in parallel to enable simultaneous ignition. For a single device of area ( $A = 4.8 \text{ mm}^2$ ) the resulting peak force and impulse was 124.1 mN and 29  $\mu\text{N} \cdot \text{s}$  respectively, whereas the three smaller ( $A = 1.6 \text{ mm}^2$ ) devices, when triggered simultaneously, produced a peak force of 91.9 mN and impulse of 28.2 Ns. The ability to incorporate multiple micro-thrusters on a single chip enables multiple actuators, though finite, that can be combined with other modes of actuation to provide greater operational use. The author also studied the interaction between adjacent devices by looking at sympathetic ignition. Future work can build upon this to look more carefully at the reaction mechanism as the reaction front propagates.

## Chapter 5

### Confining Thrust

#### 5.1 Introduction

In this chapter, the author builds upon the studies on the effects of pore morphology and device scaling on thrust and impulse to study the effects of confining the energetic porous silicon with a nozzle. Confining the gas produced by an exothermic reaction can improve propulsion performance by increasing exit pressure and velocity through a well designed nozzle. It may also allow for greater control over the direction of thrust.

In micro-thruster design, confinement has been demonstrated using a number of unique approaches to integrate the nozzle with the propellant (fuel and oxidizer mixture). The method of integration depends on the size, complexity, and operational use of the micro-thruster. The solid propellant thruster in [9] uses energetic porous silicon similar to that studied in this work, and produces a relatively large impulse of 0.14 N·s, when integrated with a plastic plate and a tube nozzle. The reaction produces an explosion, which destroys the porous silicon chip limiting the ability to have an array of multiple thrust events on a single chip. The inner diameter of the tube is 3 cm, with a wall thickness of 2 mm, and a length of 2.5 cm. The diameters of the nozzles range from 0.4 to 3 cm, with an overall system mass ranging from 32.5 to 30.2 g respectively.

The solid propellant in [11] is designed with an array of 100 individually addressable micro-thrusters, each measuring 1.5 mm by 1.5 mm. Thrust ranging from 0.3-2.3 mN per device is produced through the combustion of glycidyle azide polymer (GAP). The micro-thruster chambers are designed using both silicon and Foturan, which is a glass that can be patterned with photolithography. The nozzles are designed in a separate process using silicon wafers and deep reactive ion etching to define the divergent angle. Depending on whether silicon or glass is used for the chamber, attachment of the chamber to interface with the propellant is done using an anodic bond or epoxy. While demonstrating the ability to confine an exothermic reaction for thrust generation, the micro-thruster requires multiple processing and assembly steps, along with some manual integration.

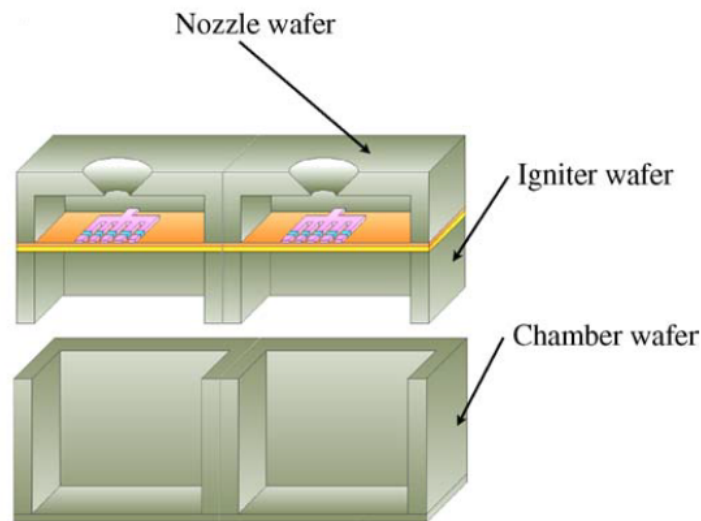


Figure 5.1: Illustration of micro-thruster fabricated with three wafers: chamber, igniter, and nozzle. Micro-thruster capable of producing up to 2.3 mN of force per device [11].

The smaller solid propellant micro-thruster demonstrated by Zhang et al [8] uses a gunpowder-based solid propellant, with 90 % gunpowder, 6 % ammonium

perchlorate, 3% aluminum, and 1%  $\text{Fe}_2\text{O}_3$  to produce peak thrust of 340 mN at sea level, while achieving an impulse of  $115 \mu\text{N} \cdot \text{s}$ . Propellant is manually loaded in a micromachined cavity and a lid attached, which allows room for the reaction gases to undergo combustion and expand through a nozzle. The reaction is confined by attaching a secondary chip made of glass and an embedded heater for ignition. As highlighted in [8], the micro-thruster shown in Figure 5.2, has the advantage of not requiring complex micro-fluidic systems, which aide in the miniaturization of the overall system. Because it uses a solid propellant, the chances of propellant leakage is minimized. The solid propellant micro-thruster in [12] can be expanded up to an array of  $8 \times 8$  propulsion elements using a three-layer stack consisting of the igniter, chamber, and nozzle layer. Shown in Figure 5.3 the chamber and igniter are fabricated with microcrystalline-glass-ceramic (MGC), and the propellant BTATZ ( $\text{C}_4\text{H}_4\text{N}_{14}$ ) is packed into the chamber. The nozzle layer is made out of silicon, and an ignition resistor triggers the propellant. The force generated by a single thruster is approximately 0.12 mN.

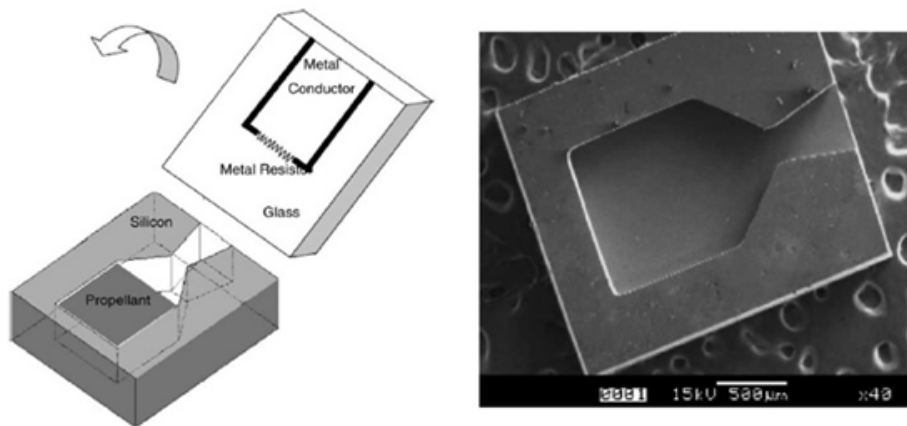


Figure 5.2: Schematic of a micro-thruster showing the chip with a cavity for embedding propellant and a separate chip with the igniter. (B) SEM of the propellant chip [8].

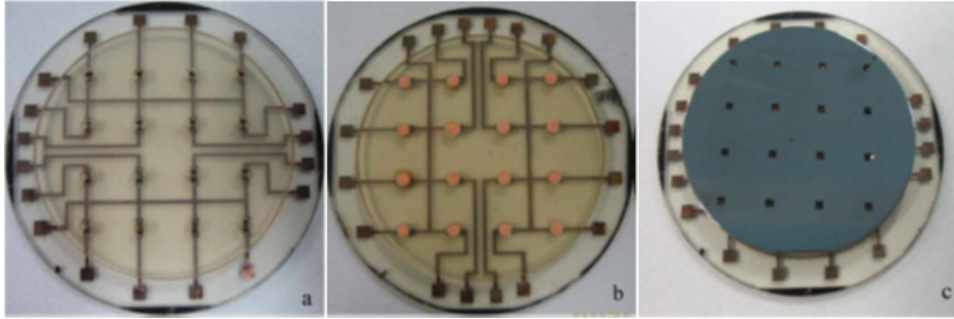


Figure 5.3: Assembled micro-thruster array consisting of (a) igniter layer, (b) chamber filled with BTATZ, and (c) the nozzle layer. Layers bonded together with silicone [12].

The goal in this work was to quantify confinement effects of solid propellant porous silicon micro-thrusters through the integration of both silicon micro-fabricated nozzles and 3D nozzles that were fabricated using additive manufacturing techniques. Ignition of the porous silicon was demonstrated with a monolithically integrated initiator, which unlike previous work shown in [9] and [8], minimizes the need for additional assembly when integrating the micro-thruster chamber and nozzle on chip.

A parametric study was done to characterize the effects of changing critical dimensions of the nozzle design on the measured thrust and impulse when integrated and ignited with the energetic porous silicon. For the 3D printed nozzles, the author varied the throat diameter of the nozzle and the divergent angle. The author showed improvements in thrust and impulse performance as a result of confinement. Details of nozzle fabrication and implementation are presented along with a quantitative analysis of the measured results.

## 5.2 Silicon Nozzle

### 5.2.1 Fabrication Methods

An initial design of the silicon nozzle was demonstrated in work published by the author in Proceedings of Transducers Eurosensors XXVII [61], which showed the integration of a micro-fabricated silicon confinement chip with a porous silicon device chip. The purpose of the confinement chip was to expand and accelerate the flow of gas produced by the porous silicon fuel and oxidizer reaction through a chamber and orifice, which was designed neglecting the nozzle divergent angle.

The porous silicon device chip was fabricated to enable the confinement chip to be mechanically bonded to the porous silicon chip. Similar to the process discussed in Chapter 2, a silicon nitride layer was first etched to expose the underlying silicon substrate, and an initiator was deposited to enable electrical triggering of the exothermic reaction. An additional processing step was introduced to electrically isolate the initiator from a metal bond ring that was needed to attach the cap chip. This was achieved by depositing a layer of Protek A2 (Brewer Science), a spin-on thermoplastic material, and patterning it on top of the initiator, serving as an electrical insulator. The Protek also served as a dam structure to prevent the oxidizer from flowing onto the bond ring. A bond ring, consisting of a 100 Å chromium, 1000 Å platinum, and 3800 Å gold was then lithographically patterned on top of the Protek A2 using metal evaporation and lift-off (Figure 5.4 (e)). Figure 5.4 shows a process flow illustrating the fabrication of the porous silicon device chip and the cap chip.

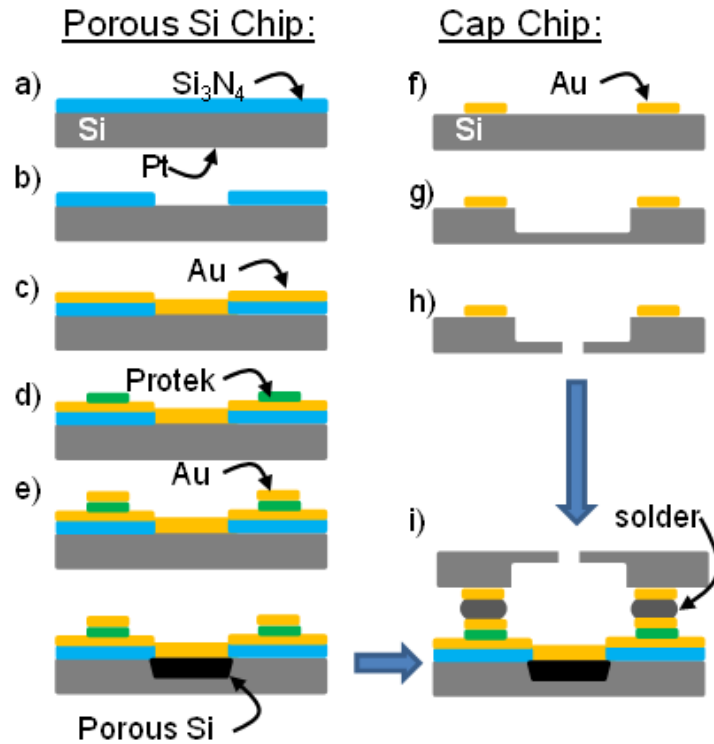


Figure 5.4: Process flow illustrating fabrication of porous silicon device chip (a through e), cap chip (f through h), and the bonding of the two chips (i).

The confinement chip was fabricated using a double side polished (DSP) silicon wafer. The first mask patterned a 100 Å chromium, 1000 Å platinum, and 3800 Å gold bond ring, allowing the confinement chip to be attached to the porous silicon chip. This bond ring was patterned by lift-off (Figure 5.4 (f)). A chamber was lithographically patterned and etched to a depth of approximately 300 μm using a deep reactive ion etch (DRIE) process (Figure 5.4 (g)). This was done to create some volume for the gas to expand. Then a backside alignment was done to pattern an orifice. The orifice, having straight sidewalls, was etched to approximately 200 μm through the wafer using DRIE as shown in Figure 5.4 (h). Finally the two chips were assembled by applying a low melting temperature

solder (Indalloy 117 from Indium Corporation) on the metalized bond rings [16]. Ideally both the porous silicon chip and the cap chip would be dipped into molten solder, through an ethylene glycol interface, allowing the solder to coat the gold bond rings that were lithographically patterned.

To avoid contamination of the porous silicon, only the cap chip was dipped in the solder. Oxidizer was then applied to the porous silicon chip, paying careful attention not to get excess oxidizer on the bond ring. Then the chips were heated to 70 °C to allow the solder to soften and flow. The bond ring on the cap chip was aligned with the porous silicon chip. After cooling, the two chips adhered to each other. Each porous silicon device and cap chip was individually bonded prior to testing. Figure 5.5 shows a fully assembled porous silicon device and cap chip. This fabrication process had a number of integration challenges because of insufficient solder coating the bond rings, and problems associated with the manual alignment process.

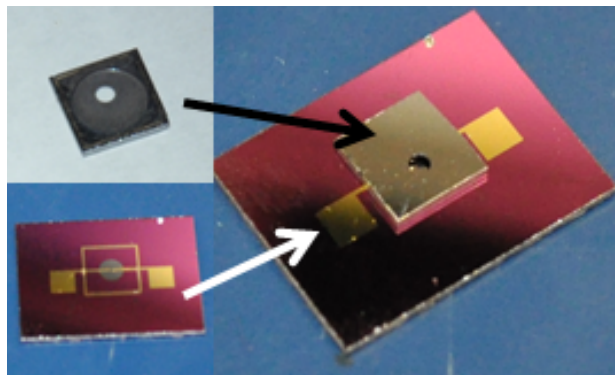


Figure 5.5: Fully assembled porous silicon device chip and cap chip.

Integration of the confinement chip and the porous silicon device chip presented

a number of unique challenges including the inability to completely coat the bond rings on both silicon chips. Figure 5.6 shows partial coverage of the solder on the square bond ring that encompassed a reacted 2 mm diameter porous silicon device. This resulted in weakened attachment points between the porous silicon device chip and the confinement chip, causing the confinement chip to become detached and launch itself into the air upon ignition.

Manually aligning the two silicon chips was also a challenge because of the tight alignment tolerance between the two bond rings and the need to ensure that the solder did not solidify before proper alignment was made. Additional process improvements could be made to include alignment pillars or fiducial marks to ensure more accurate alignment as well as increasing the width of the bond ring to aid in better wetting and adhesion of the solder.

Additionally, it was unclear whether the author was effectively removing residual ethylene glycol from the pores after the low temperature solder dipping process. This was a potential source of process variability that might have altered device performance. A different fabrication approach to building the micro-thruster, which was based on a 3D printing technique, will be discussed in the sections to follow.

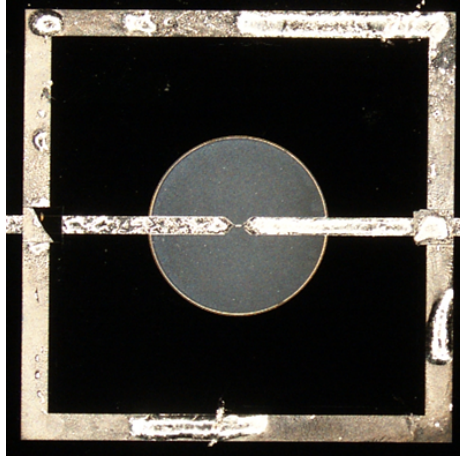


Figure 5.6: Partial coverage of bond pad with solder after dipping process.

### 5.2.2 Results

Thrust performance was measured with and without the attachment of the confinement chip. Porous silicon was etched in a 20:1 mixture of hydrofluoric acid to ethanol to a nominal etch depth of  $15\ \mu\text{m}$  to avoid shattering the chip. The original etch depth of  $40\ \mu\text{m}$  was reduced because upon ignition, the deeper etched porous silicon excited multiple resonance peaks in the sensor resulting in constructively interfering sine waves at 5.5 kHz and 13.5 kHz. Because more thrust was measured with this particular device etched at 20:1 hydrofluoric acid to ethanol, confinement was evaluated on the 20:1 etched sample rather than one etched using a 3:1 etch solution. Results showed that confining the porous silicon reaction produced an increase in measured force for similarly etched samples [61]. The force output and specific impulse were measured based on a comparison of an unconfined reaction with a confined reaction. The peak force generated by the unconfined porous silicon was approximately 400 mN, while the peak

force generated by the confined sample was over 800 mN. The confined force curve corresponded to an impulse of  $148 \mu\text{N} \cdot \text{s}$ , while the unconfined curve corresponded to  $35 \mu\text{N} \cdot \text{s}$ . The specific impulses were 126 s and 29 s, respectively. There was a 4.3x increase in impulse and approximately 2x increase in peak force as a result of confining the reaction.

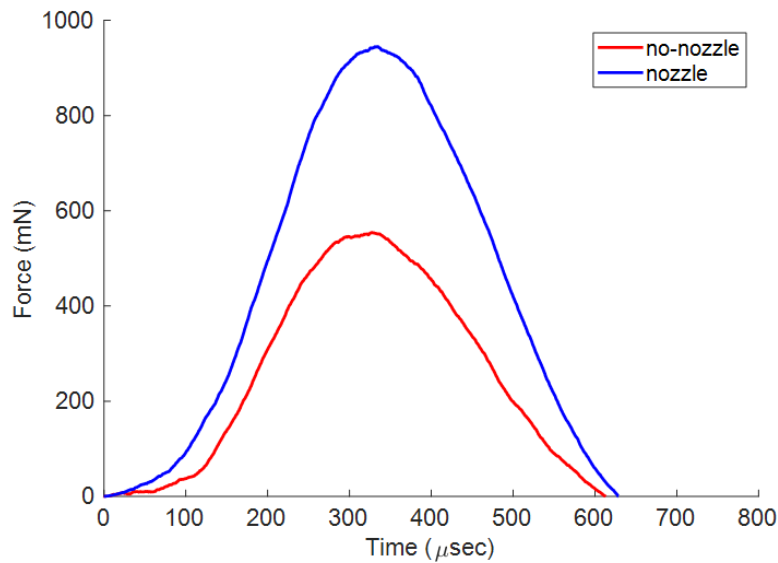


Figure 5.7: Comparison of confined versus unconfined thrust.

While the author demonstrated increased thrust performance with the silicon micro-fabricated nozzle, challenges associated with integration, both solder dipping and silicon chip alignment, prevented the author from reproducing the experiments. Alignment marks could have been incorporated into the lithographic mask design to guide the attachment of the cap chip onto the porous silicon chip. While attempts were made to incorporate a polymer (Protek) ring around the porous silicon to confine the oxidizer to the porous silicon to avoid contaminating the solder bond rings, these polymer rings delaminated during

the etch. Widening the bond rings may have enabled better wetting and coverage of the solder during the dipping process. To overcome these challenges, the author decided to 3D print nozzles using an additive manufacturing approach, which allowed for greater control over critical parameters of the nozzle design. The larger 3D printed nozzles also proved easier to integrate using epoxy attachment.

## 5.3 3-Dimensional Printed Nozzles

### 5.3.1 Fabrication and Parametric Design

While the previous approach showed improvement in thrust performance, in order to address challenges associated with fabricating the nozzle out of a silicon wafer, an alternative fabrication method was demonstrated in this research that involved 3D printing the nozzle, including both the chamber and convergent divergent nozzle. Nozzles were designed in SolidWorks with intended variations to several key parameters that were believed to effect thrust performance. The author developed a design of experiments, which involved varying critical parameters of the nozzle design. These parameters are illustrated in the drawing in Figure 5.8. Nozzle H was not tested because the results generated by Nozzles E-G indicated no improvement in thrust performance as a result of confinement. Nozzle I was not possible to fabricate because of limitations placed on nozzle length and the convergent divergent angle. The throat diameter of the micro-thruster  $D_t$  was varied ( $D_t = 0.75$  mm, 1.0 mm, 1.25 mm). The nozzle length ( $L_2$ ) was varied

to satisfy the relationship  $L_2/D_t$  equivalent to 3. Finally the angle of divergence  $\theta$  was varied ( $\theta = 10^\circ, 20^\circ, 30^\circ$ ).

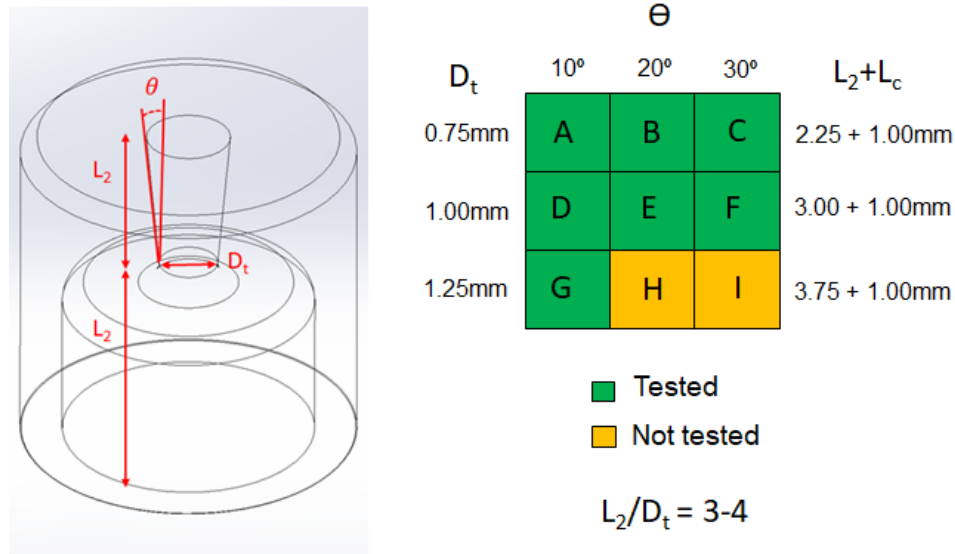


Figure 5.8: Summary of parameters varied in the design of the micro-thruster chamber and nozzle.

Nozzles were printed with Formlabs Form 2 Stereolithography (SLA) 3D printer using an additive manufacturing process that selectively cures a resin with a Class 1, 405 nm (250 mW) violet laser. Designs were drawn in SolidWorks 2018 and drawings were imported into Formlabs PreForm software, which allowed for specific nozzle designs to be arrayed, and printed during a single run.

The quantity of nozzles and the print resolution were the limiting factors considered when setting up a print. Figure 5.9 shows an array of nozzles, each nominally having the same physical dimensions. Each device was printed with a series of support structures to enable both the printing of finer resolution features, as well as to avoid building directly onto the build plate. Because the resin cures directly onto the build plate, without support structures it was very difficult

to remove printed parts. Printing three sets of these arrays took approximately 2.5 hours because the highest resolution (0.025 mm) was used when printing the parts. The author used a clear resin when printing nozzles. Figure 5.10 shows a single micro-thruster printed with a clear resin on the Form 2. After printing, the parts were removed from the build plate and placed in a UV curer and allowed to cure of 45 minutes at 65°C



Figure 5.9: An array of printed micro-thruster chambers and nozzles with support structures.



Figure 5.10: Images of a micro-thruster printed with Form 2 taken with Keyence Microscope

### 5.3.2 Design Verification

Because of the relatively small feature sizes of the nozzle, and the challenges associated with achieving small feature sizes with a resin based printer, the parts

were visually analyzed to determine whether dimensions for throat diameter and divergent angle were equivalent to their designed dimensions. Analysis was performed on 3 of the 7 design configurations, specifically Nozzles A, B, and C from Figure 5.8..

Micro-computerized tomography (Micro-CT) scans of printed nozzles were performed using a Xradia 510 Versa. The scans were performed with a 4X objective and an exposure time of 1 second, and a pixel size of approximately 4  $\mu\text{m}$ . The scan voltage and power were 80 kV and 7 W respectively. Figure 5.11 shows actual scans of the printed nozzles. It took approximately 15 hours to complete scans on three nozzles. Table 5.1 summarizes the parameters for the nozzle, which include throat diameter ( $D_t$ ), divergent angle ( $\theta$ ), and nozzle length  $L_2$ , and compares the dimensions as-designed with the actual dimensions after fabrication. The average throat diameter was 0.82 mm with a standard deviation of 0.09 mm, while the values for the divergent angles were within approximately 1  $^\circ$  or less of the designed values. The average nozzle length was 2.33 mm with a standard deviation of 0.11 mm. These results provided added confidence that the 3D printed nozzles were representative of the designed nozzles.

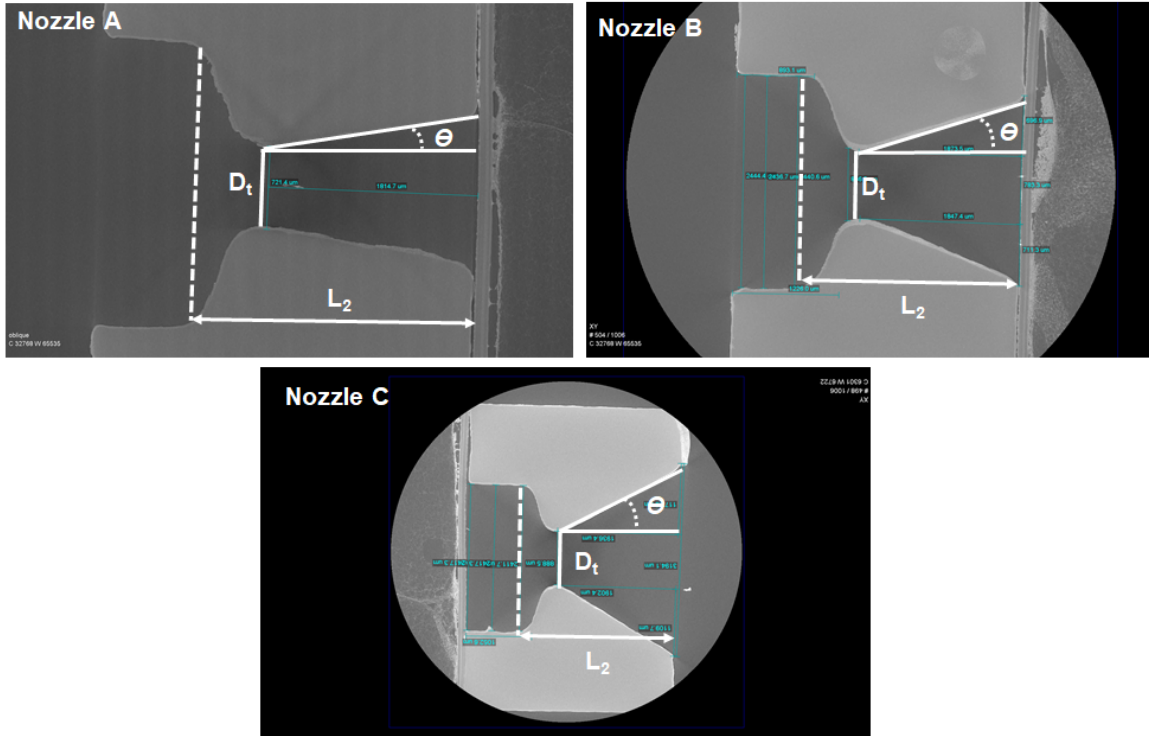


Figure 5.11: Images from micro-computerized tomography scan performed on 3D printed micro-thruster.

Table 5.1: Table provides a comparison of intended nozzle design parameters with actual dimensions measured after fabrication using Micro-CT scans.

	Designed Measured		Designed Measured		Designed Measured	
	$D_t$ (mm)	$D_t$ (mm)	$\theta$	$\theta$	$L_2$ (mm)	$L_2$ (mm)
Nozzle A	0.75	0.72	10 °	11.3 °	2.25	2.36
Nozzle B	0.75	0.84	20 °	20.4 °	2.25	2.42
Nozzle C	0.75	0.89	30 °	30.4 °	2.25	2.20

### 5.3.3 Assembly and Testing

Each nozzle was evaluated with similarly etched porous silicon material. Silicon coupons were etched using 3:1 HF to EtOH, with 0.96 mL of H<sub>2</sub>O<sub>2</sub>. The resistivity of the coupon was held between 5 Ω-cm to 7 Ω-cm. Etch time was chosen to etch porous silicon layers with a nominal etch depth of 20 μm. A test coupon

was etched and the porous silicon removed to verify that the etch time was properly calibrated for the intended etch depth. Prior to assembling and testing the micro-thruster, one out of the four devices on a coupon was oxidized and tested with the force sensor to obtain a baseline for the force generated without a nozzle present. Generally, one coupon was used to evaluate the performance of a single micro-thruster design. When additional coupons were needed to evaluate other designs or to gather additional data points, a calibration test was always performed without a nozzle present to ensure consistency across the measurements taken.

After performing the baseline calibration etch, wire leads were soldered to the remaining porous silicon devices. A ring of silicone was painted around the 2 mm diameter porous silicon device, and allowed to cure as shown in Figure 5.12. The purpose of the ring was to first contain the oxidizer, and to help with aligning the the micro-thruster over the porous silicon device. Although the porous silicon diameter was 2 mm, the chamber diameter was designed to be 2.5 mm in diameter, allowing for 0.5 mm of alignment tolerance. Silicone was also applied around the edges of the bottom (chamber side) of the micro-thruster, and the micro-thruster was attached to the porous silicon device after the oxidizer was applied and allowed to cure. Figure 5.13 shows a chamber and nozzle attached to the porous silicon device. An extra ring of silicone was manually applied around the edge of the nozzle to ensure that the chamber was properly sealed. Alignment was verified by visual inspection of the center section of the bridgewire initiator through the orifice.

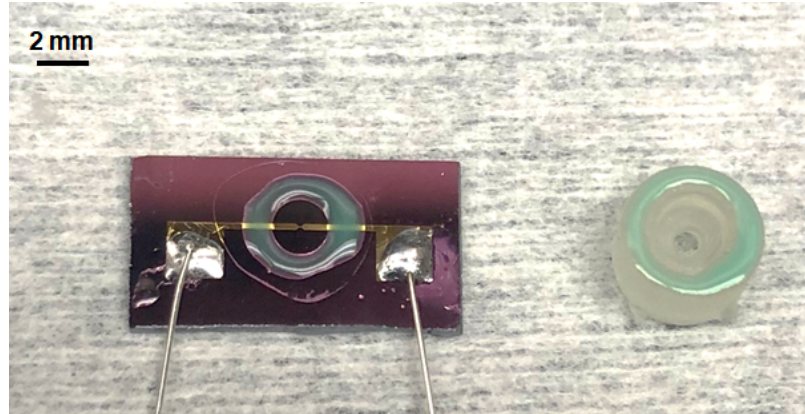


Figure 5.12: To make it easier to align the nozzle to the porous silicon chip, a ring of silicone was painted around the outer edge of the porous silicon device. Silicone was also painted on the bottom of the nozzle.

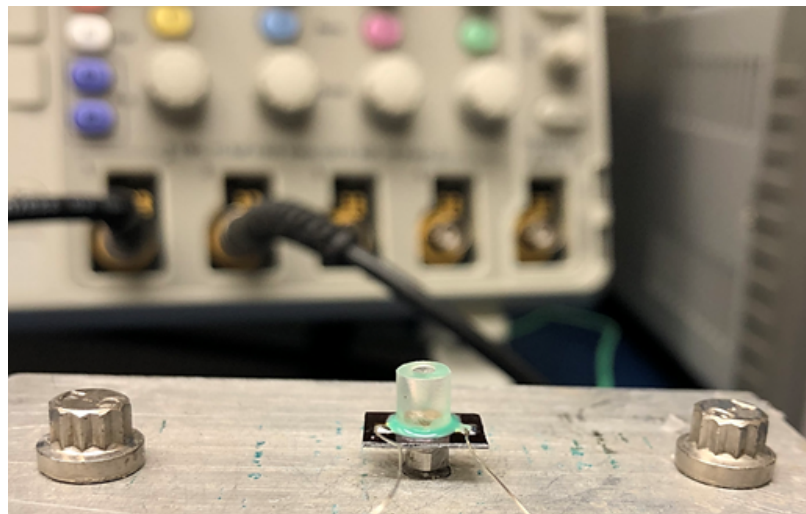


Figure 5.13: 3D printed nozzle attached to oxidized porous silicon device and mounted to force sensor.

## 5.3.4 Results

### 5.3.4.1 Micro-CT Post-Ignition

Nozzles A, B, and C were re-scanned in the Micro-CT tool after the nozzles were integrated with the energetic porous silicon and ignited. The purpose was to

verify that the heat generated from the combustion event was not deforming features of the chamber. Figure 5.14 shows images of the nozzles after ignition of the porous silicon. There was evidence of residual porous silicon particulates on the inner walls of the chamber, but no obstructions at the throat of the nozzle. Table 5.2 summarizes the critical parameters of the nozzle design before and after the nozzle was subjected to the exothermic reaction. The average measured throat diameter was 0.83 mm with a standard deviation of 0.07 mm, while the measured values for the divergent angles were within approximately two degrees of the designed values after the burn. The average nozzle length was 2.35 mm with a standard deviation of 0.10 mm. The most noticeable difference after the burn was slight variation in the divergent angle ( $\theta$ ), but the maximum delta of 2.6 ° before and after the burn was not believed to be sufficient to warrant changing the fabrication approach. Performing these scans before and after the combustion event provided verification that the 3D printing process was a viable approach to fabricating nozzles. The clear resin used to print the nozzles withstood the temperatures and burn duration produced by the porous silicon.

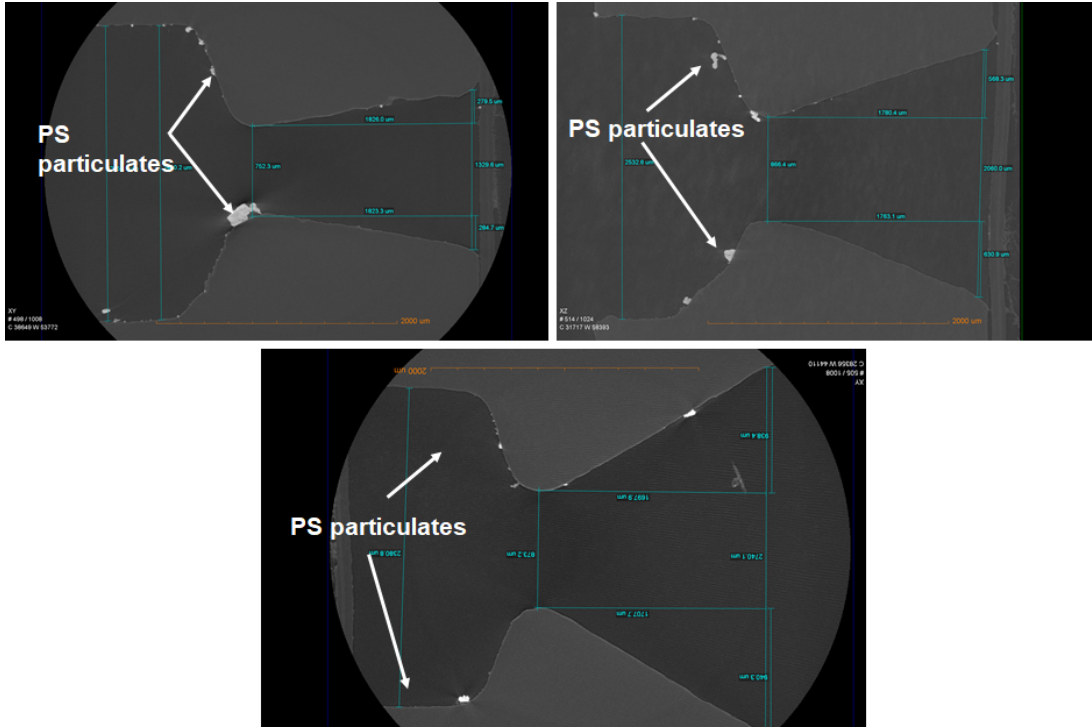


Figure 5.14: Images from micro-computerized tomography scan performed on 3D printed micro-thruster after nozzle were subjected to porous silicon burn.

Table 5.2: Table provides a comparison of intended nozzle design parameters with actual dimensions measured after subjecting the nozzle to the exothermic porous silicon reaction.

	Before $D_t$ (mm)	After $D_t$ (mm)	Before $\theta$	After $\theta$	Before $L_2$ (mm)	After $L_2$ (mm)
Nozzle A	0.72	0.75	11.3 °	8.7 °	2.36	2.37
Nozzle B	0.84	0.87	20.4 °	17.8 °	2.42	2.43
Nozzle C	0.89	0.87	30.4 °	28.9 °	2.20	2.24

### 5.3.4.2 Video Analysis

High speed video was captured with a Photron FastCAM SA5 to qualitatively compare the directionality of the plume of gas generated when the reaction was unconfined and when it was directed using the integrated nozzle. Figure 5.15

shows a comparison of two reactions both captured at 2000 frames per second. Without the nozzle, the flame appeared to propagate more radially outward and produced a large fireball that lacked directionality and was somewhat random in terms of flame dispersion. It was unclear whether residual oxidizer on the surface of the porous silicon was potentially re-igniting in air. The reaction with the integrated nozzle appeared to be much more focused in terms of directionality and the fireball was confined to the chamber.

Additionally, this analysis allowed the author to verify that the nozzle was securely attached to the silicon chip. Because a silicone epoxy (Loctite E-20 HP) was used to attach the nozzle to the porous silicon chip, the author needed to verify that the epoxy was properly cured and the seal between the porous silicon chip and the nozzle remained in-tact during the exothermic reaction. Figure 5.16 shows three consecutive frames captured at 1024 by 1024 dots per square inch resolution and 2000 frames per second. Because the nozzle was made of a semi-transparent resin, the chamber appears to glow as the plume of hot gas expands before being ejected through the nozzle. The video confirmed that the reaction byproducts were confined before being ejected through the nozzle. Any possible breach in the silicone would have caused the nozzle to detach itself from the porous silicon, and become a flyer.

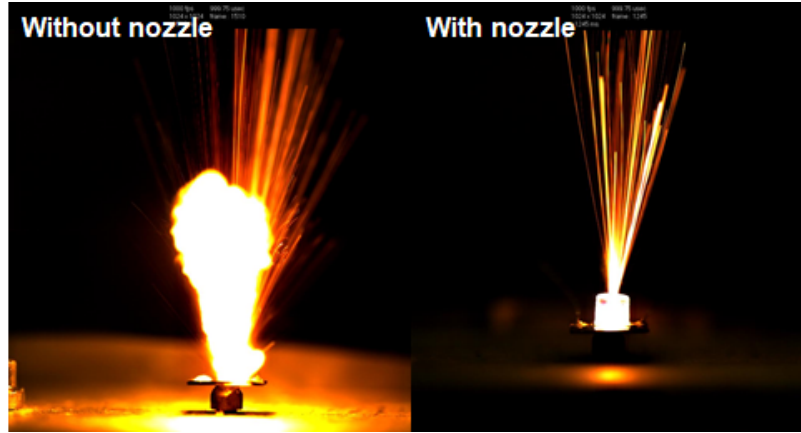


Figure 5.15: (left) Porous silicon reaction without a nozzle (right) and one with a nozzle.

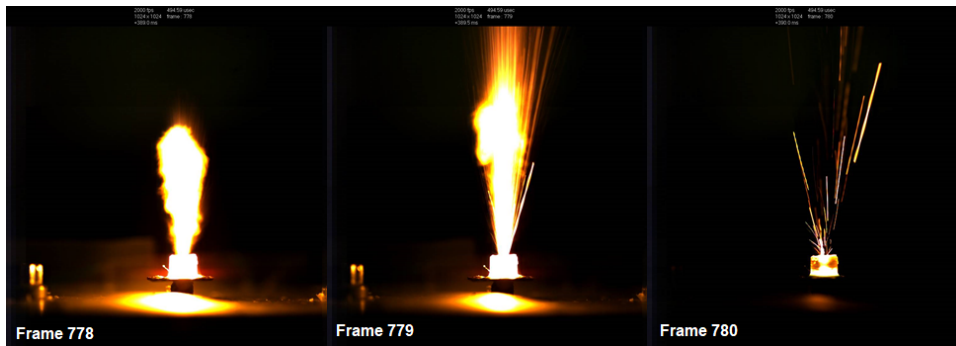


Figure 5.16: 3D printed nozzle attached to oxidized porous silicon device and mounted to force sensor.

### 5.3.4.3 Force Measurements

Figure 5.17 shows force versus time curves for seven different micro-thruster nozzle configurations that were evaluated. The most significant increase in thrust and impulse was measured from nozzles that had a throat diameter ( $T_d$ ) of 0.75 mm. Varying  $\theta$  did not produce noticeable changes in the thrust profiles. Based on the design parameters outlined in [74], the divergent angle  $\theta$  of the diverging part of the nozzle should be between  $15^\circ$  and  $20^\circ$ . Therefore the similarities in the measured results for varied  $\theta$  at a fixed ( $T_d$ ) of 0.75 mm verified the lack of

appreciable difference in performance.

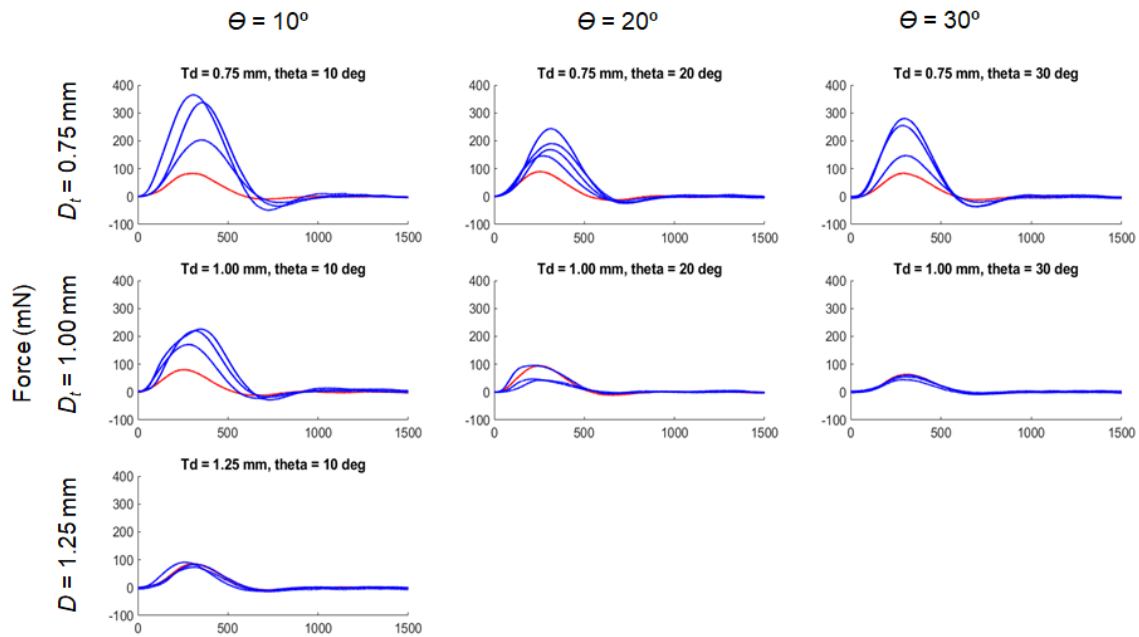


Figure 5.17: Force versus time curves for different micro-thruster nozzle configurations evaluated.

Figure 5.18 shows the average force versus time curves based on the individual measurements in 5.17 as well as the mean value plus and minus the standard deviation illustrated by the solid lines. Based on the average force measured, the best performing nozzle was observed from the nozzle with a chamber height of 1 mm, a throat diameter ( $T_d$ ) of 0.75 mm, and  $\theta$  measuring  $10^\circ$ . In comparison to the larger throat diameters evaluated, it appeared that having a smaller throat diameter provided the necessary confinement to accelerate the gaseous byproducts of the reaction. Improvements in thrust depend on the mass flow rate that can be achieved, which depends on the throat area.

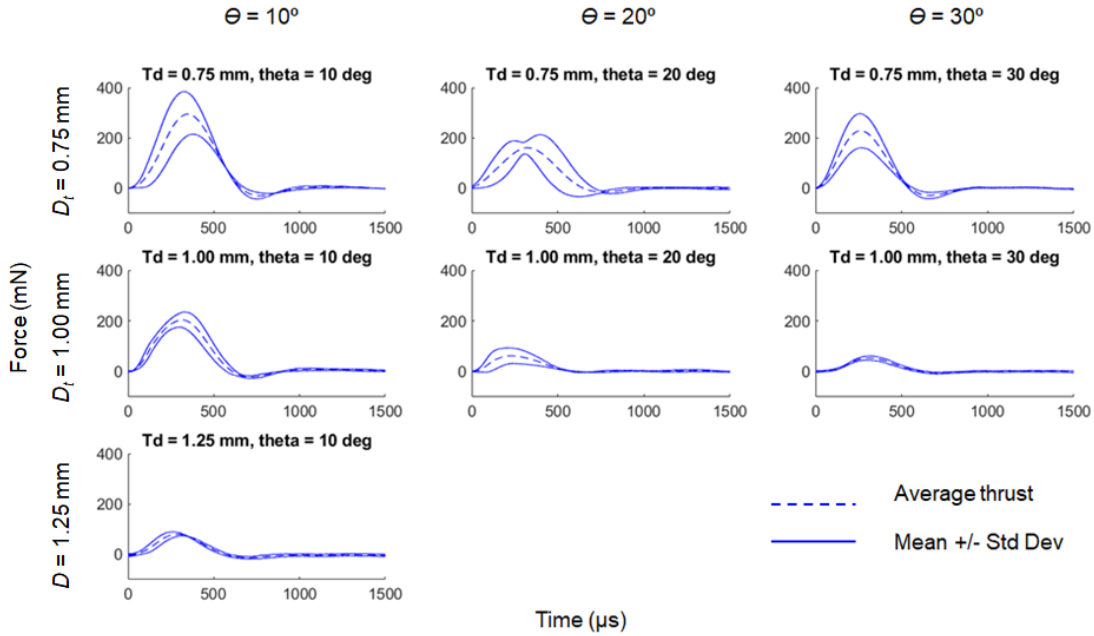


Figure 5.18: Force versus time curves for different micro-thruster nozzle configurations evaluated showing average force plus and minus the standard deviation.

Table 5.3 summarizes the results shown in Figure 5.18 highlighting the measured values for average peak thrust based on the different design configurations. A summary of average impulse based on micro-thruster nozzle configuration is shown in Table 5.4.

Table 5.3: Summary of thrust performance for the different nozzle configurations.

Nozzle	Peak Force	Avg. Force (mN)	Std Dev.
A	364.8	292.6	83.9
B	313.6	180.8	40.1
C	279.3	219.3	68.6
D	225.7	199.4	29.6
E	95.3	59.8	29.4
F	60.6	51.5	8
G	90.6	79.4	8.5
no nozzle	92.9	82.1	9.3

Table 5.4: Summary of impulse performance for the different nozzle configurations.

Nozzle ( $\mu\text{N} \cdot \text{s}$ )	Peak Impulse	Avg. Impulse ( $\mu\text{N} \cdot \text{s}$ )	Std Dev.
A	111.3	92.6	23.5
B	69.0	53.5	13.0
C	76.0	62.2	21.9
D	77.0	65.3	13.1
E	30.2	18.7	10.0
F	17.7	15.2	3.3
G	24.7	21.9	3.9
no nozzle	24.4	22.0	2.4

## 5.4 Summary

The author successfully demonstrated fabrication of a 3D printed nozzle and performed a parametric study to investigate the effect of changing design parameters of the nozzle, including the nozzle throat diameter and the divergent angle. Improvements to thrust were demonstrated through integration of a nozzle, in particular with Nozzle A ( $D_t = 0.75 \text{ mm}$ ,  $\theta = 10^\circ$ ). The average peak force produced by the energetic porous silicon devices without a nozzle was 82.1 mN with a standard deviation of 9.3 mN. The average impulse produced by devices without a nozzle was  $22.0 \mu\text{N} \cdot \text{s}$  with a standard deviation of  $2.4 \mu\text{N} \cdot \text{s}$ . Incorporating Nozzle A with the porous silicon chip resulted in approximately 4x increase in

the average peak thrust, and over a 4x increase in the average impulse. Although there were variations in the reproducibility of measured force and impulse, the author was able to see trends indicating enhanced thrust performance as a result of integrating a nozzle with the porous silicon. Additional work could be done to implement a thrust stand measurement system to more precisely measure thrust as a function of angular displacement.

Fabrication of the nozzle using 3D printing dramatically reduced the time needed to prototype the nozzles from approximately 1 week to 3 hours. The silicon nozzle required two separate lithography steps to pattern the chamber and orifice, a third lithography step to pattern the bond ring, and a metal deposition and deep reactive ion etch before completion. Changing nozzle parameters using the 3D printing process eliminated the need for mask re-design, because parameters could be easily modified in SolidWorks and exported to the Form 2 for re-print. Based on the minimum feature size for the nozzle throat diameter (0.75 mm) needed for the parametric study, the Form 2 appeared to be capable of meeting the design tolerance.

## Chapter 6

### Conclusions

This work provides key insights that have advanced the understanding of energetic porous silicon as a solid propellant micro-thruster based on an extensive experimental study of the material's thrust performance. Thrust performance was measured as a function of porous silicon morphology, where morphology was characterized according to the porosity of the material. Porosity was varied by altering parameters of the etch process, including electrolyte concentrate, wafer resistivity, and etch time, which correlates to the depth of porous silicon. Thrust was measured quantitatively using a 9215 Kistler piezoelectric force sensor. The accuracy of the sensor was verified using weights of known mass to provide a static measurement, and was also verified by measuring the angular displacement of a pendulum set in motion by an energetic porous silicon device.

The dependency of thrust and impulse generated by porous silicon as a function of the porous silicon area for a single thrust event was experimentally studied and presented in this work. The author provided key insights on the effects of simultaneous ignition and scaling the area of energetic porous silicon. The study also identified critical spacing between adjacent devices to mitigate potential sympathetic ignition and determined the trade-offs between thrust and impulse and the density of micro-thrusters that could be integrated on a 1 cm<sup>2</sup> chip.

Overall, the experimental data provided an understanding of scaling propulsion and trade-offs and limitations associated with propulsion event density.

Finally, the author demonstrated fabrication of 3D printed nozzles, using additive manufacturing techniques, and presented key findings on the effects of confining the byproducts of the exothermic reaction of porous silicon. Seven different nozzle configurations were printed as part of a parametric study. Critical design components, such a nozzle throat diameter and the divergent angle were varied to understand the effects of confinement. The primary contributions of this work are summarized as follows:

- Characterized thrust as a function of porosity, and how different porous silicon etch parameters affect porosity.
- Characterized the effects of scaling the size of porous silicon to deliver multiple propulsion events on a single 1 cm<sup>2</sup> chip.
- Characterized the effects of sympathetic and simultaneous ignition with arrays of porous silicon devices to determine trade-offs associated with achieving multiple propulsion events on a single 1 cm<sup>2</sup> chip.
- Integrated 3D printed nozzles at millimeter size scales and characterized the effects of confining the energetic porous silicon reaction.

## 6.1 Future Work

To further understand energetic porous silicon as a propellant enhancing thrust performance, future work would include the following:

- Develop a pore model, including boundary methods, to model the interaction of the pores at the molecular level along with mass and energy diffusion to understand transport and reaction rates through the porous silicon network when activated with a liquid oxidizer. This is generally a challenge within the field of nano-energetics to understand the complex decomposition stages associated with the reaction [54]
- Perform an in-depth study of the porous silicon reaction propagation to determine the mechanism of ignition and to understand the mechanism associated with the sympathetic ignition of adjacent porous silicon devices. This involves designing and implementing a Schlieren imaging setup to study shock wave interactions at the surface of the porous silicon.
- Study sub-surface porous silicon shock wave interactions through silicon using a series of piezo-pins to track propagation through the backside of the silicon chip. This would aid in better understanding the mechanisms associated with sympathetic ignition.
- Perform high speed thermal imaging to determine if sympathetic ignition of porous silicon is due to thermal conduction of hot particulates ejected from the reaction.

- Implement a thrust stand measurement system to more accurately measure thrust, especially thrust levels close to 1 N, which generally excited multiple resonant frequencies in the current piezo-force sensor. This would allow the author to look at the maximum limits of thrust generation.
- Develop an analytical model for the energetic porous silicon and nozzle configurations to verify experimentally collected data and to further optimize the design.
- Build upon the current parametric study to evaluate nozzles with throat diameters less than 0.75 mm and greater than 1.25 mm and nozzle divergent angles less than 10 degrees and greater than 30 degrees to include a wider data set.
- Demonstrate tethered multi-propulsion/jumping using energetic porous silicon micro-thrusters and nozzles attached to a milli-gram size microrobot. Specifically show multi-jump capability to traverse a flight of stairs.
- Develop a work space model for a milli-gram size microrobot to understand the limits of jump height and trajectory based on single and multiple propulsion events.

## Chapter B

### MATLAB

#### B.1 Experimental and Computational Background

## Bibliography

- [1] G. P. Sutton and M. Burrows, "Biomechanics of jumping in the flea," *Journal of Experimental Biology*, vol. 214, no. 5, pp. 836–847, 2011.
- [2] M. Noh, S.-W. Kim, S. An, J.-S. Koh, and K.-J. Cho, "Flea-inspired catapult mechanism for miniature jumping robots," *Robotics, IEEE Transactions on*, vol. 28, no. 5, pp. 1007–1018, Oct 2012.
- [3] B. Lambrecht, A. D. Horchler, and R. Quinn, "A small, insect-inspired robot that runs and jumps," in *Robotics and Automation, 2005. ICRA 2005. Proceedings of the 2005 IEEE International Conference on*, April 2005, pp. 1240–1245.
- [4] P. Fiorini, S. Hayati, M. Heverly, and J. Gensler, "A hopping robot for planetary exploration," in *Aerospace Conference, 1999. Proceedings. 1999 IEEE*, vol. 2, 1999, pp. 153–158 vol.2.
- [5] J.-S. Koh, E. Yang, G.-P. Jung, S.-P. Jung, J. H. Son, S.-I. Lee, P. G. Jablonski, R. J. Wood, H.-Y. Kim, and K.-J. Cho, "Jumping on water: Surface tension-dominated jumping of water striders and robotic insects," *Science*, vol. 349, no. 6247, pp. 517–521, 2015.
- [6] A. Gerratt and S. Bergbreiter, "Incorporating compliant elastomers for jumping locomotion in microrobots," *Smart Materials and Structures*, vol. 22, no. 1, p. 014010, 2013.
- [7] S. Bergbreiter and K. Pister, "Design of an autonomous jumping micro-robot," in *Robotics and Automation, 2007 IEEE International Conference on*, April 2007, pp. 447–453.
- [8] K. Zhang, S. Chou, S. Ang, and X. Tang, "A mems-based solid propellant microthruster with au/ti igniter," *Sensors and Actuators A: Physical*, vol. 122, no. 1, pp. 113–123, 2004.
- [9] V. Nguyen, K. Pita, and C. H. Kam, "Giant and tunable mechanical impulse of energetic nanocrystalline porous silicon," *Journal of Propulsion and Power*, vol. 31, no. 2, pp. 694–698, March-April 2015.
- [10] C. R. Becker, S. Apperson, C. J. Morris, S. Gangopadhyay, L. J. Currano, W. A. Churaman, and C. R. Stoldt, "Galvanic porous silicon composites for high-velocity nanoenergetics," *Nano Letters*, vol. 11, no. 2, pp. 803–807, 2011.
- [11] C. Rossi, D. Briand, M. Dumonteuil, T. Camps, P. Q. Pham, and N. F. de Rooij, "Matrix of 10 by 10 addressed solid propellant microthrusters: Review of the technologies," *Sensors and Actuators A: Physical*, vol. 126, no. 1, pp. 241 – 252, 2006.

- [12] X. Wu, P. Dong, Z. Li, S. Li, Q. Liu, and H. Wan, "Design, fabrication and characterization of a solid propellant micro-thruster," in *2009 4th IEEE International Conference on Nano/Micro Engineered and Molecular Systems*, Jan 2009, pp. 476–479.
- [13] L. Igor and et. al., "Space micropropulsion systems for cubesats and small satellites: From proximate targets to furthestmost frontiers," *Applied Physics Reviews*, vol. 5, no. 1, p. 011104, 2018.
- [14] V. Zaitsev, O. Gvirsman, U. B. Hanan, A. Weiss, A. Ayali, and G. Kosa, "A locust-inspired miniature jumping robot," *Bioinspiration and Biomimetics*, vol. 10, no. 6, p. 066012, 2015.
- [15] H. Tsukagoshi, M. Sasaki, A. Kitagawa, and T. Tanaka, "Design of a higher jumping rescue robot with the optimized pneumatic drive," in *Robotics and Automation, 2005. ICRA 2005. Proceedings of the 2005 IEEE International Conference on*, April 2005, pp. 1276–1283.
- [16] W. A. Churaman, "Novel integrated system architecture for an autonomous jumping micro-robot," Master's thesis, University of Maryland, at College Park, 2123 Lee Building, College Park, MD 20742, August 2010.
- [17] W. A. Churaman, C. R. Becker, C. J. Morris, L. J. Currano, C.-C. Wu, and M. J. Sailor, "Packaging nanoporous energetic silicon for on-chip mems applications," in *Proceedings of the Wafer-Level Packaging*, 2011, pp. 1–6.
- [18] D. Teasdale, V. Milanovic, P. Chang, and K. Pister, "Microrockets for smart dust," *Smart Mater. Struct.*, vol. 10, pp. 1145–1155, 2001.
- [19] M. Li, W. Cheng, K. Liu, Y. He, X. Li, and X. Liao, "Sweep coverage with mobile sensors," *IEEE Transactions on Mobile Computing*, vol. 10, no. 11, pp. 1534–1545, Nov 2011.
- [20] A. Hoover, E. Steltz, and R. Fearing, "Roach: An autonomous 2.4g crawling hexapod robot," in *Intelligent Robots and Systems, 2008. IROS 2008. IEEE/RSJ International Conference on*, Sept 2008, pp. 26–33.
- [21] U. Scarfogliero, C. Stefanini, and P. Dario, "A bioinspired concept for high efficiency locomotion in micro robots: the jumping robot grillo," in *Proceedings 2006 IEEE International Conference on Robotics and Automation, 2006. ICRA 2006.*, May 2006, pp. 4037–4042.
- [22] K. Lemmer, "Propulsion for cubesats," *Acta Astronautica*, vol. 134, pp. 231–243, 2017.
- [23] S. Stoeter, P. Rybski, M. Gini, and N. Papanikolopoulos, "Autonomous stair-hopping with scout robots," in *Intelligent Robots and Systems, 2002. IEEE/RSJ International Conference on*, vol. 1, 2002, pp. 721–726 vol.1.

- [24] R. Armour, K. Paskins, A. Bowyer, J. Vincent, and W. Megill, "Jumping robots: a biomimetic solution to locomotion across rough terrain," *Bioinspiration & Biomimetics*, vol. 2, no. 3, pp. S65–S82, 2007.
- [25] T. Bandyopadhyay, K. Von-Richter, M. Pallaud, and A. Elfes, "Differential jumping: A novel mode for micro-robot navigation," in *2016 IEEE International Conference on Robotics and Automation (ICRA)*, May 2016, pp. 3813–3818.
- [26] S. Apperson, A. Bezmelnitsyn, R. Thiruvengadathan, K. Gangopadhyay, S. Gangopadhyay, W. Balas, P. Anderson, and S. Nicolich, "Characterization of nanothermite material for solid-fuel microthruster applications," *Journal of Propulsion and Power*, vol. 25, pp. 1086–1091, 2009.
- [27] W. Lindsay, D. Teasdale, V. Milanovic, K. Pister, and C. Fernandez-Pello, "Thrust and electrical power from solid propellant microrockets. 2. actuators," in *Micro Electro Mechanical Systems, 2001. MEMS 2001. The 14th IEEE International Conference on*, Jan 2001, pp. 606–610.
- [28] E. Mukerjee, A. Wallace, K. Yan, D. Howard, R. Smith, and S. Collins, "Vaporizing liquid microthruster," *Sensors and Actuators A: Physical*, vol. 83, no. 13, pp. 231 – 236, 2000. [Online]. Available: ,
- [29] J. Xiong, Z. Zhou, D. Sun, and X. Ye, "Development of a {MEMS} based colloid thruster with sandwich structure," *Sensors and Actuators A: Physical*, vol. 117, no. 1, pp. 168–172, 2005.
- [30] J. Kohler, J. Bejhed, H. Kratz, F. Bruhn, U. Lindberg, K. Hjort, and L. Stenmark, "A hybrid cold gas microthruster system for spacecraft," *Sensors and Actuators A: Physical*, vol. 9798, pp. 587 – 598, 2002.
- [31] F. Pranajaya and M. Cappelli, "Development of a colloid micro-thruster for flight demonstration on the emerald nanosatellite." Reston, VA: American Institute of Aeronautics and Astronautics, 2001 2001.
- [32] M. Gamero-Castao and V. Hruby, "Electrospray as a Source of Nanoparticles for Efficient Colloid Thrusters," *Journal of Propulsion and Power*, vol. 17, pp. 977–987, 2001.
- [33] A. Chaalane, C. Rossi, and D. Estve, "The formulation and testing of new solid propellant mixture for a new mems-based microthruster," *Sensors and Actuators A: Physical*, vol. 138, no. 1, pp. 161 – 166, 2007.
- [34] D. Lewis, S. Janson, R. Cohen, and E. Antonsson, "Digital micropropulsion," *Sensors and Actuators A: Physical*, vol. 80, no. 2, pp. 143 – 154, 2000.
- [35] M. Kova, M. Bendana, R. Krishnan, J. Burton, M. Smith, and R. J Wood, "Multi-stage micro rockets for robotic insects," *Robotics*, p. 185, 2013.

- [36] D. Maurya, S. Das, and S. Lahiri, "Silicon mems vaporizing liquid microthruster with internal microheater," *Journal of Micromechanics and Microengineering*, vol. 15, no. 5, p. 966, 2005.
- [37] K. Karthikeyan, S. Chou, L. Khoong, Y. Tan, C. Lu, and W. Yang, "Low temperature co-fired ceramic vaporizing liquid microthruster for microspacecraft applications," *Applied Energy*, vol. 97, pp. 577 – 583, 2012.
- [38] S. Janson, H. Helvajian, W. Hansen, and L. L. J., "Microthrusters for nanosatellites," in *Integrated Micro Nanotechnology for Space Applications (MEMS), 1999 Second International Conference on*, Apr 1999.
- [39] W. Storck, O. Billett, M. Jambusaria, A. Sadhwani, P. Jammes, and J. Cutler, "A survey of micropropulsion for small satellites," in *In Proceedings of the 20th Annual Small Satellites Conference*, 2006.
- [40] A. Kakami, H. Koizumi, K. Komurasaki, and Y. Arakawa, "Design and experiments of a pulsed plasma thruster (ppt) using liquid propellants," *Journal of the Japan Society of Aeronautical and Space Sciences*, vol. 51, no. 589, pp. 85 – 88, 2003.
- [41] R. Cassady, W. Hoskins, M. Campbell, and C. Rayburn, "A micro pulsed plasma thruster (ppt) for the 'dawgstar' spacecraft," in *Aerospace Conference Proceedings, 2000 IEEE*, vol. 4, 2000, pp. 7–14 vol.4.
- [42] M.-H. Wu and R. A. Yetter, "A novel electrolytic ignition monopropellant microthruster based on low temperature co-fired ceramic tape technology," *Lab Chip*, vol. 9, pp. 910–916, 2009.
- [43] E. A. London, A.P. and J. Kerrebrock, "High pressure bipropellant micro-rocket engine," *Journal of Propulsion and Power*, vol. 17, no. 4, pp. 780–787, 2001.
- [44] M. Kovac, M. Fuchs, A. Guignard, J.-C. Zufferey, and D. Floreano, "A miniature 7g jumping robot," in *Robotics and Automation, 2008. ICRA 2008. IEEE International Conference on*. IEEE, 2008, pp. 373–378.
- [45] M. Archer, M. Christophersen, and P. Fauchet, "Electrical porous silicon chemical sensor for detection of organic solvents," *Sensors and Actuators B: Chemical*, vol. 106, no. 1, pp. 347–357, 2005.
- [46] H. Arrand, T. Benson, P. Sewell, A. Loni, R. Bozeat, R. Arens-Fischer, M. Kruger, M. Thonissen, and H. Luth, "The application of porous silicon to optical waveguiding technology," *Selected Topics in Quantum Electronics, IEEE Journal of*, vol. 4, no. 6, pp. 975–982, Nov 1998.
- [47] N. Piekielek, C. Morris, W. Churaman, M. Cunningham, D. Lunking, and L. Currano, "Combustion and material characterization of highly tunable

on-chip energetic porous silicon," *Propellants, Explosive, and Pyrotechnics*, vol. 40, pp. 16–26, 2015.

- [48] A. Uhlir and I. W. Uhlir, "Historical perspective on the discovery of porous silicon," *physica status solidi (c)*, vol. 2, no. 9, pp. 3185–3187, 2005.
- [49] M. du Plessis, "A decade of porous silicon as nano-explosive material," *Propellants, Explosive, and Pyrotechnics*, vol. 39, pp. 348–364, 2013.
- [50] M. du Plessis and C. Conradie, "Nano-explosions in porous silicon," in *Device and Process Technologies for Microelectronics, MEMS, and Photonics IV*, *Proc. of SPIE*, 2005.
- [51] W. A. Churaman, L. J. Currano, A. Singh, U. Rai, M. Dubey, P. Amirtharaj, and P. Ray, "Understanding the high energetic behavior of nano-energetic porous silicon," *Chemical Physics Letters*, vol. 464, no. 46, pp. 198 – 201, 2008.
- [52] X. Zhou, M. Torabi, J. Lu, R. Shen, and K. Zhang, "Nanostructured energetic composites: Synthesis, ignition/combustion modeling and applications," *Applied Materials and Interfaces*, vol. 6, no. 5, pp. 3058–3074, 2014.
- [53] F. Elwinger, P. Pourmand, and I. Furo, "Diffusive transport in pores. tortuosity and molecular interaction with the pore wall," *Journal of Physical Chemistry*, vol. 121, pp. 13 757–13 764, 2017.
- [54] A. Plummer, V. Kuznetsov, J. Gascooke, J. Shapter, and N. Voelcker, "Combined thermal and ftir analysis of porous silicon based nano-energetic films," *Royal Society of Chemistry Advances*, vol. 7, pp. 7338–7345, 2017.
- [55] A. Plummer, V. Kuznetsov, T. Joyner, J. Shapter, and N. H. Voelcker, "The burning rate of energetic films of nanostructured porous silicon," *Small*, vol. 7, no. 23, pp. 3392–3398, 2011.
- [56] W. A. Churaman, L. J. Currano, C. J. Morris, J. E. Rajkowski, and S. Bergbreiter, "The first launch of an autonomous thrust-driven microrobot using nanoporous energetic silicon," *Microelectromechanical Systems, Journal of*, vol. 21, no. 1, pp. 198–205, Feb 2012.
- [57] N. W. Piekial, C. J. Morris, W. A. Churaman, M. E. Cunningham, D. M. Lunking, and L. J. Currano, "Combustion and material characterization of highly tunable on-chip energetic porous silicon," *Propellants, Explosives, Pyrotechnics*, pp. 16–26, 2015.
- [58] L. J. Currano and W. A. Churaman, "Energetic nanoporous silicon devices," *Microelectromechanical Systems, Journal of*, vol. 18, no. 4, pp. 799–807, Aug 2009.

- [59] L. Gelb and K. Gubbins, "Characterization of porous glasses: simulation models, adsorption isotherms, and the Brunauer Emmett Teller analysis method," *Langmuir*, vol. 14, no. 8, pp. 2097–2111, 1998.
- [60] Kistler Instrument Corp., "Sensors for small forces, type 9215a datasheet," 2019.
- [61] W. A. Churaman, C. J. Morris, L. J. Currano, and S. Bergbreiter, "On-chip porous silicon microthruster for robotic platforms," in *Solid-State Sensors, Actuators and Microsystems (Transducers Eurosensors XXVII), 2013 Transducers Eurosensors XXVII: The 17th International Conference on*, June 2013, pp. 1599–1602.
- [62] W. A. Churaman, C. J. Morris, R. Ramachandran, and S. Bergbreiter, "The effect of porosity on energetic porous silicon solid propellant micro-propulsion," *Journal of Micromechanics and Microengineering*, vol. 25, no. 11, p. 115022, 2015.
- [63] V. S. Parimi, S. A. Tadigadapa, and R. A. Yetter, "Reactive wave propagation mechanisms in energetic porous silicon composites," *Combustion Science and Technology*, vol. 187, no. 1-2, pp. 249–268, 2015.
- [64] M. Du Plessis, "Integrated porous silicon nano-explosive devices," in *Electron Devices and Materials, 2006. Proceedings. 7th Annual 2006 International Workshop and Tutorials on*, July 2006, pp. 6–13.
- [65] R. Ramachandran, W. A. Churaman, D. Lunking, and C. J. Morris, "Characterization of energetic porous silicon for a microelectromechanical system (mems)-based solid propellant microthruster," U.S. Army Research Laboratory, Tech. Rep. A14-141, September 2014.
- [66] L. Currano, W. Churaman, and C. Becker, "Nanoporous silicon as a bulk energetic material," in *Solid-State Sensors, Actuators and Microsystems Conference, 2009. TRANSDUCERS 2009. International*, June 2009, pp. 2172–2175.
- [67] K. S. Martirosyan and S. E. Lyshevski, "Mems technology microthrusters and nanoenergetic materials for micropropulsion systems," in *2012 2nd International Conference "Methods and Systems of Navigation and Motion Control" (MSNMC)*, Oct 2012, pp. 133–136.
- [68] A. Szelecka, J. Kurzyna, D. Danilko, and S. Barral, "Liquid micro pulsed plasma thruster," *Journal of Nukleonika*, vol. 60, no. 2, pp. 257 – 261, 2015.
- [69] Z. Miao, J. Mo, G. Li, Y. Ning, and B. Li, "Wheeled hopping robot with combustion-powered actuator," *International Journal of Advanced Robotic Systems*, vol. 15, no. 1, p. 1729881417745608, 2018.

- [70] K. Sathiyathan, R. Lee, H. Chesser, C. Dubois, R. Stowe, R. Farinaccio, and S. Ringuette, "Solid propellant microthruster design for nanosatellite applications," *Journal of Propulsion and Power*, vol. 27, no. 6, pp. 1288–1294, 2011.
- [71] M. Noh, S.-W. Kim, S. An, J.-S. Koh, and K.-J. Cho, "Flea-inspired catapult mechanism for miniature jumping robots," *IEEE Transactions on Robotics*, vol. 28, no. 5, pp. 1007–1018, 2012.
- [72] W. Hu, G. Z. Lum, M. Mastrangeli, and M. Sitti, "Small-scale soft-bodied robot with multimodal locomotion," *Nature*, vol. 554, no. 81, 2018.
- [73] J. Bustillo, J. Fortineau, and M. Lethiecq, "Thickness evaluation of mesoporous silicon layer using ultrasonic method," in *11th European Conference on Non-Destructive Testing, Prague, Czech Republic*, Oct 2010.
- [74] M. C. Louwerse, H. V. Jansen, M. N. W. Groenendijk, and M. C. Elwenspoek, "Nozzle fabrication for micropropulsion of a microsatellite," *Journal of Micromechanics and Microengineering*, vol. 19, no. 4, p. 045008, Mar 2009.